

Fabrication of Hysteresis-Free Perovskite Solar Cells by SAM Modified Electrode

Doctor of Philosophy
in
Materials Science and Engineering

by

Eyyup Yalçın

ORCID 0000-0002-7468-2169

May, 2022

This is to certify that we have read the thesis **Fabrication of Hysteresis-Free Perovskite Solar Cells by SAM Modified Electrode** submitted by **Eyyup Yalçın**, and it has been judged to be successful, in scope and in quality, at the defense exam and accepted by our jury as a DOCTORAL THESIS.

APPROVED BY:

Advisor: **Prof. Dr. Şerafettin Demić**

İzmir Kâtip Çelebi University

Committee Members:

Prof. Dr. Sermet Koyuncu

Çanakkale Onsekiz Mart University

Prof. Dr. Cem Tozlu

İzmir Kâtip Çelebi University

Prof. Dr. Mustafa Can

İzmir Kâtip Çelebi University

Assist. Prof. Dr. Burak Gültekin

Ege University

Date of Defense: May 30, 2022

Declaration of Authorship

I, **Eyyup Yalçın**, declare that this thesis titled **Fabrication of Hysteresis-Free Perovskite Solar Cells by SAM Modified Electrode** and the work presented in it are my own. I confirm that:

- This work was done wholly or mainly while in candidature for the Doctoral degree at this university.
- Where any part of this thesis has previously been submitted for a degree or any other qualification at this university or any other institution, this has been clearly stated.
- Where I have consulted the published work of others, this is always clearly attributed.
- Where I have quoted from the work of others, the source is always given. This thesis is entirely my own work, with the exception of such quotations.
- I have acknowledged all major sources of assistance.
- Where the thesis is based on work done by myself jointly with others, I have made clear exactly what was done by others and what I have contributed myself.

Signature:

Date: 30.05.2022

Fabrication of Hysteresis-Free Perovskite Solar Cells by SAM Modified Electrode

Abstract

Energy has become one of the main problems of humanity after the industrial revolution and the rapid rise in world population. Most energy resources depend on fossil fuels, which causes environmental problems. Solar energy is a clean and sustainable alternative to the increasing world energy demand. In this context, perovskite solar cells (PSCs) are particularly attractive due to ability to achieve very high efficiencies. The power conversion efficiency (PCE) of PSCs has rapidly grown from 3.8% in 2009 to over 25.5% in 2022, which making it fastest advancing solar cell technology to date.

The work present in this thesis is focused on the novel self-assembled monolayers (SAMs) that act as hole transport layer (HTL) in p-i-n type perovskite solar cells to obtain high power conversion efficiency. With SAMs, interfacial power losses between the perovskite and charge selective layers mitigated. In addition, SAMs decrease the carrier recombination between interfaces, improve the perovskite film quality with a bigger grain size, and increase device stability and PCE.

The aim of this thesis is replacement of conventional HTLs, PEDOT:PSS and PTAA, by SAM molecules. The works done in this thesis consist of two parts.

In the first part, we studied the use of two novel SAM molecules (nominated MC-43 and TPA) made of semiconductor hole transport organic molecules to replace the most common p-type contact, PEDOT:PSS, in p-i-n methylammonium lead iodide (MAPI) PSCs. The PSCs fabricated with SAMs show remarkable PCEs, with the best cell based on TPA scoring 15.9% and the best performing MC-43 cell scoring

17.3%. Devices fabricated with both SAMs show a negligible hysteresis and improved stability. Also, it is important to notice that the efficiency obtained with MC-43 devices is among the highest values reported in the literature until that time (23.06.2018).

In the second part, we reported three novel SAM molecules used as HTLs for p-i-n type triple cation (CsMAFA) PSCs while PTAA used as baseline HTL for performance comparison. Two of SAM molecules have bidentate anchoring group (nominated MC-54 and MC-55) while one of them has monodentate anchoring group (nominated MC-45). Besides the PTAA comparison, we also have made a comparison between those two types of molecules (monodentate and bidentate groups). Photovoltaic performance of SAM molecule with bidentate anchoring groups (MC-54 and MC-55) has higher PCE than MC-45, which has monodentate anchoring group, and current standard polymeric PTAA. The best cell performance of MC-54, MC-55, MC-45 and PTAA are 19.52%, 18.99%, 16.69% and 18.62% PCE, respectively. Devices with SAM molecules have negligible hysteresis and improved stability.

Keywords: Perovskite solar cells, self-assembled monolayers, interface engineering, solar energy

SAM Modifiyeli ITO Elektrot ile Histeresis Göstermeyen Perovskit Güneş Hücresi Üretimi

ÖZ

Sanayi devrimi ve dünya nüfusunun hızla artmasından sonra enerji, insanlığın temel sorunlarından biri haline gelmiştir. Çoğu enerji kaynağı, çevre sorunlarına neden olan fosil yakıtlara bağlıdır. Güneş enerjisi, artan dünya enerji talebine temiz ve sürdürülebilir bir alternatiftir. Bu bağlamda, perovskit güneş pilleri (PSC'ler), çok yüksek verimler elde etme kabiliyetleri nedeniyle çok dikkat çekicidirler. PSC'lerin güç dönüşüm verimliliği (PCE), 2009'da %3,8 iken 2022'de %25,5'in üzerine hızla çıkmıştır ve bu da onu bugüne kadarki en hızlı ilerleyen güneş pili teknolojisi haline getirmiştir.

Bu tezde bulunan mevcut çalışma, yüksek güç dönüşüm verimliliği elde etmek için p-i-n tipi perovskit güneş pillerinde boşluk taşıma katmanı (HTL) olarak görev alan özgül kendiliğinden organize tek katman moleküllerine (SAMs) yoğunlaşmıştır. SAM'ler ile perovskite ve yük seçici katmanlar arasındaki ara yüz güç kayıpları azaltıldı. Ek olarak, SAM'ler ara yüzler arasındaki yük rekombinasyonunu azalttı, daha büyük tane boyutu ile perovskit film kalitesini iyileştirdi, cihaz kararlılığını ve PCE'yi de artırdı.

Bu tezin amacı, geleneksel HTL'ler olan PEDOT:PSS ve PTAA'nın yerine SAM moleküllerinin kullanılmasıdır. Bu tez kapsamında yapılan çalışmalar iki bölümden oluşmaktadır.

İlk bölümde, p-i-n metilamonyum kurşun iyodür (MAPI) PSC'ler de en yaygın p-tipi kontak olan PEDOT:PSS'nin yerini almak için yarı iletken boşluk taşıma organik moleküllerinden yapılmış iki yeni SAM molekülünün (MC-43 ve TPA olarak

adlandırılmıştır) kullanımını inceledik. SAM'lerle üretilen PSC'ler dikkate değer PCE'ler gösterdi. TPA ile üretilen cihazların en iyi hücre verimi %15.9 ve en iyi performans gösteren MC-43 hücresinin verimi ise %17.3'tür. Her iki SAM ile üretilen cihazlar, ihmal edilebilir bir histeresis ve daha iyi bir kararlılık gösterdi. Ayrıca MC-43 cihazları ile elde edilen verimin literatürde o zamana kadar bildirilen en yüksek değerler arasında yer aldığını da belirtmek fayda var (23.06.2018).

İkinci bölümde, p-i-n tipi üçlü katyon (CsMAFA) PSC'ler için HTL'ler olarak kullanılan üç yeni SAM molekülünü ve performans karşılaştırılması için referans HTL olarak PTAA'nın kullanıldığını raporladık. SAM moleküllerinden ikisi, iki bacaklı yapıya (MC-54 ve MC-55 olarak adlandırılan) sahipken, bunlardan biri tek bacaklı yapıya (MC-45 olarak adlandırılan) sahiptir. PTAA karşılaştırılmasının yanı sıra, bu iki tip molekül (tek bacaklı ve iki bacaklı gruplar) arasında da bir karşılaştırma yaptık. İki bacaklı yapıya sahip (MC-54 ve MC-55) SAM moleküllerinin fotovoltaik performansı, tek bacaklı yapıya sahip MC-45 ile mevcut standart polimerik PTAA'ya göre daha yüksek PCE'ye gösterdiler. MC-54, MC-55, MC-45 ve PTAA'nın en iyi hücre performansı sırasıyla %19.52, %18.99, %16.69 ve %18.62'dir. SAM molekülleri ile üretilen cihazlar ihmal edilebilir histeresis ve daha iyi kararlılık gösterdi.

Anahtar Kelimeler: Perovskit güneş pilleri, kendiliğinden organize tek katman tabakaları, ara yüzey mühendisliği, güneş enerjisi

To my family,

Acknowledgment

First and foremost, I would like to grant special appreciation to my supervisor Prof. Dr. Şerafettin Demić for his tremendous support with sharing his knowledge and experience. I learned a lot from him both from humanity and on the scientific point of view. I am also grateful to Prof. Dr. Emilio Palomares for opening his laboratory to me and for his support during my stay at ICIQ. I feel lucky to work with him.

I also would like to express my gratitude to Prof. Dr. Mustafa Can and Prof. Dr. Cem Tozlu. They were available all the time for discussion and my questions. Our discussions were beneficial for the progress and improvement of the thesis work.

I would like to thank all my colleagues, Dr. Emre Arkan, Dr. Abdullah Bayram, Dr. M. Zeliha Arkan, Merve Karaman, Kenan Ensariođlu, Dr. Koray Kara, Gülsüm Ersu, İpek Yoldaş and Yenal Gökpek, at the IKÇÜ. It has been a pleasure to share with you all this time.

I had a great time during my stay at ICIQ and Tarragona. Thanks to all the people I have worked at the ICIQ, I learned a lot from you. Thanks to Werther Cambarau, Dr. Ece Aktaş, Dr. Maria Mendez, Dr. Jose G. Sanchez, Dr. Ilario Gelmetti, Dr. Eugenia Martinez, Dr. Lijun Su, Dora A. Gonzalez, Beatriu Domingo, Sarika Kumari, Dr. Carlos E. Puetro, Sarah Hudson and of course Santi Gene!. Also, thanks to Sorania Jimenez for her kind help. Thank you all.

I am thankful for the financial support of ‘the scientific and technological research council of Turkey (TUBITAK)’ during one year of my research in ICIQ, Tarragona/Spain.

I am also grateful to my family for their supports. They have always been with me all my life and I became who I am today.

To all of you, Thank you.

Table of Contents

Declaration of Authorship	ii
Abstract	iii
Öz	v
Acknowledgment	viii
Table of Contents.....	ix
List of Figures.....	xii
List of Tables.....	xvi
List of Abbreviations	xvii
List of Symbols.....	xx
1 Introduction.....	1
1.1 Perovskite Solar Cells	2
1.2 Device Architectures of Perovskite Solar Cells.....	3
1.3 Working Principles of Perovskite Solar Cells	4
1.4 J-V Hysteresis in Perovskite Solar Cells.....	6
1.5 Self Assembled Monolayers as Hole Transport Materials.....	8
2 Experimental Methods and Characterizations Techniques.....	11
2.1 Small Molecules.....	11
2.1.1 4, 4"-bis(diphenylamino)-1,1':3',1"-terphenyl-5'-carboxylic [TPA] .	11
2.1.2 4'-[bis(2',4'-dimethoxybiphenyl-4-yl)amino]-biphenyl-4-carboxylic acid [MC-43].	12
2.1.3 4'-(bis(4-methoxyphenyl)amino)-[1,1'-biphenyl]-4-carboxylic acid [MC-45].....	13
2.1.4 4',4'''-([1,1'-biphenyl]-4,4'-diylbis(m-tolylazanediy))bis((1,1'-biphenyl)-4-carboxylic acid)) [MC-54]	14

2.1.5	4,4'''-([1,1'-biphenyl]-4,4'-diylbis (naphthalene-1-ylazanediy))bis((1,1'-biphenyl)-4-carboxylic acid)) [MC-55].....	15
2.2	Device Fabrication of Perovskite Solar Cells	16
2.2.1	Device Fabrication of MAPI Perovskite Solar Cell	16
2.2.2	Device Fabrication of CsMAFA Perovskite Solar Cells	18
2.3	Characterization Techniques.....	19
2.3.1	Cyclic Voltammetry.....	19
2.3.2	UV-vis Absorbance Spectroscopy.....	20
2.3.3	Thermal Analysis.....	20
2.3.4	X-Ray Photoelectron Spectroscopy.....	21
2.3.5	Atomic Force Microscopy.....	21
2.3.6	Contact Angle.....	21
2.3.7	Scanning Electron Microscopy.....	21
2.3.8	X-Ray Diffraction.....	22
2.3.9	Photoluminescence Measurements.....	22
2.3.10	Characterization of Perovskite Solar Cells.....	22
2.3.11	Effect of Light Intensity on Current Density and Open-Circuit Voltage	24
2.3.12	Stability Measurements of Perovskite Devices	26
3	Self-Assembled Monolayers as Hole Transport Materials in MAPI Perovskite Solar Cells.....	27
3.1	Abstract.....	28
3.2	Introduction.....	28
3.3	Results and Discussion.....	30
3.3.1	SAM modification of the ITO surface	30
3.3.2	Photovoltaic Performance	37
3.3.3	Conclusions	43
4	A Comparison of Monodentate and Bidentate Anchoring Group of Small Molecules as Hole Transport Layer for Perovskite Solar Cells.....	44

4.1	Introduction.....	44
4.2	Result and Discussion	46
4.2.1	Thermogravimetric (TGA) and Differential Scanning Calorimetry (DSC) Measurement of SAM molecules	48
4.2.2	Optical and Electrochemical Characterization of Molecules	49
4.2.3	Effects of SAM Molecules on ITO surface and Perovskite properties.	51
4.2.4	Photovoltaic Performance	63
4.3	Conclusion	72
5	General Conclusion	73
	References	75
	Appendices	92
	Appendice A	93
	Appendice B.....	97
	Curriculum Vitae.....	98

List of Figures

Figure 1.1	Crystal structure of perovskite [11].....	3
Figure 1.2	Device configuration of the most common used PSCs in literature	4
Figure 1.3	Schematic illustration of electrons and holes injection process in a p-i-n architecture perovskite solar cell.....	5
Figure 1.4	An example of forward/reverse scan J - V curves for hysteresis.....	6
Figure 1.5	Schematic illustration of 3 main parts of SAM molecules	9
Figure 1.6	Illustration of a carboxylic acid molecule attaching on a metal oxide surface	10
Figure 2.1	Schematic illustration of MAPI (a), and CsMAFA (b) perovskite solar cells device structures.....	16
Figure 2.2	Illustration of device preparation steps. The ITO substrates are treated with UV-ozone before SAM deposition.	17
Figure 2.3	Illustration of device preparation steps. The ITO coated substrates were treated with UV/ozone before SAM deposition.....	19
Figure 2.4	A typical J - V curve (red line) of perovskite solar cells with V_{OC} , J_{SC} , FF and MPP parameters. J_{MP} and V_{MP} are current and voltage at the MMP, respectively. The ratio between blue and light grey rectangles areas is the FF	23
Figure 2.5	J - V curves of a perovskite solar cell with MC-45 SAM molecule under different light intensities (from 1 sun to dark) on reverse condition.....	24
Figure 2.6	a) Current density dependence with the light intensity and b) open-circuit voltage dependence with the light intensity. Both figures obtained from reverse J - V curves of Figure 2.5.....	26
Figure 3.1	The molecular structure of (a) TPA and (b) MC-43. (c) Energy levels of the PSC materials employed in this study. (d) Layered structure of the SAM based device	31
Figure 3.2	Cyclic voltammograms of ITO/TPA (a) and ITO/MC-43 (b)	32

Figure 3.3	Top: Contact angle measurements on the (a) bare ITO surface, (b) ITO/TPA surface and (c) ITO/MC-43 surface. Bottom: Surface topographical AFM images of (d) bare ITO, (e) ITO/TPA and (f) ITO/MC-43.....	33
Figure 3.4	XPS Survey Spectrum of C1s, O1s and N1s for ITO/MC-43 (a) and ITO/TPA (b).....	33
Figure 3.5	The XPS high resolution survey spectra of C 1s (a) and O 1s (b) for ITO/MC-43. The XPS high resolution survey of C 1s (c) and O 1s (d) for ITO/TPA...35	35
Figure 3.6	High resolution surface spectra of N1s for ITO/MC-43 (a), ITO/TPA (b) and bare ITO (c).....	36
Figure 3.7	Morphology of the perovskite films on top of the modified and nonmodified ITO surface: (a) bare ITO; (b) ITO/PEDOT:PSS; (c) ITO/TPA; and (d) ITO/MC-43	37
Figure 3.8	Top: <i>J-V</i> characteristics of the best devices, measured at 1 sun in the reverse voltage scan direction at a speed of 40 mV s ⁻¹ , and EQE spectra of the same cells. Bottom: PCE tracking of the best devices under continuous illumination, obtained by registering the current density at the applied voltage corresponding to the maximum power point (MPP)	38
Figure 3.9	Statistics of photovoltaic parameters for PSCs based on MC-43 (red), TPA (green) and PEDOT:PSS (blue) recorded at 1 sun for both forward and reverse voltage scan	39
Figure 3.10	<i>J-V</i> characteristics of best PSC based on MC-43 (red), TPA (green), PEDOT:PSS (blue) and bare ITO (yellow) at 1 sun. Both forward and reverse scans have been performed at a scan rate of 40 mV/s.....	40
Figure 3.11	Evolution of the <i>J-V</i> characteristic, measured at 1 sun, for a MC-43 based PSC over 20 days. The device was encapsulated and stored in dark under low humidity conditions.....	42
Figure 3.12	Long-term evolution of photovoltaic parameters of the best MC-43 based PSC measured at 1 sun.....	42
Figure 4.1	(a) Chemical structure polymeric PTAA and SAM molecules, (b) device structure of p-i-n (inverted) perovskite solar cell, (c) cross section FESEM images of a complete device, (d) work function of bare ITO, SAM modified ITOs, PTAA and CsMAFA perovskite.....	47

Figure 4.2	TGA analyses of MC-45, MC-54 and MC-55 at scan rate of 10°C/min under N ₂ atmosphere	48
Figure 4.3	DSC analyses of MC-45, MC-54 and MC-55 at scan rate of 10 °C/min under N ₂ atmosphere	49
Figure 4.4	CV voltammogram of SAM molecules in solution (a) and ITO/SAM coating (b). UV (dashed lines) and PL Intensity (solid lines) of MC-45, MC-54 and MC-55 (c).....	50
Figure 4.5	XPS high-resolution surface spectra of C1s and O1s for ITO/MC-45 (a), ITO/MC-54 (b), ITO/MC-55 (c) and bare ITO (d).....	52
Figure 4.6	High resolution surface spectra of N1s for ITO/MC-45, ITO/MC-54 and ITO/MC-55.....	54
Figure 4.7	Surface topography of bare ITO, ITO/PTAA, ITO/MC-45, ITO/MC-54 and ITO/MC-55 from different scan scales	55
Figure 4.8	RMS values of bare ITO and modified ITO from different scan scales	55
Figure 4.9	Surface topography and surface potential mapping of ITO/SAM from KPFM	56
Figure 4.10	Contact angle of (a) bare ITO, (b) ITO/MC-45, (c) ITO/MC-54 and (d) ITO/MC-55	57
Figure 4.11	FESEM images (up and middle) and grain size distribution (down) of perovskite films before and after modification of ITO. Perovskite was deposited on a) bare ITO, b) ITO/PTAA, c) ITO/MC-45, d) ITO/MC-54 and e) ITO/MC-55.....	58
Figure 4.12	SEM cross-section of full devices: (a) ITO/PTAA, (b) ITO/MC-45, (c) ITO/MC-54, and (d) ITO/MC-55.....	59
Figure 4.13	XRD patterns of bare ITO, ITO/PTAA, ITO, MC-45, ITO/MC-54 and ITO/MC-55	60
Figure 4.14	(a) Steady-state PL and (b) TrPL spectra of CsMAFA perovskite film on bare ITO, PTAA, MC-45, MC-54 and MC-55	62
Figure 4.15	(a) J-V curves of best solar cells in forward (JSC to VOC, solid line) and reverse scan (VOC to JSC, dashed line). (b) External quantum efficiency (EQE) spectra which show integrated current density of best solar cells. (c) Statistic values of photovoltaic parameters with PTAA, MC-45, MC-54 and MC-55 HTL for both forward (fwd) and reverse (rev) scan direction.....	64

Figure 4.16	Built-in potential is estimated from dark J-V curves of PTAA (a), MC-45 (b), MC-54 (c) and MC-55 (d).....	66
Figure 4.17	J-V curves of PTAA, MC-45, MC-54 and MC-55 based devices at different light intensity	67
Figure 4.18	(a) JSC and (b) VOC dependence of light intensity for different HTM68	
Figure 4.19	Stability of the completed PSCs based on SAMs and PTAA (a), and stability of SAM molecules on ITO for MC-45 (b), MC-54 (c) and MC-55 (d) measured by CV for 30th cycles.....	69
Figure 4.20	Differential capacitance at different light bias with and without C _{geo} for PSCs with different HTMs. Dashed lines correspond to linear fitting of C _{geo} . Solid lines (at the bottom) correspond to carrier density after subtraction of geometrical capacitance.....	70
Figure 4.21	(a) Charge (n) carrier measured from DC vs carrier lifetime obtained via TPV for different HTMs and (b) after subtraction of geometrical capacitance.....	71
Figure A.1	XPS high-resolution surface spectra of C1s (a) and O1s (b) for bare ITO.	93
Figure A.2	XPS survey spectrum of bare ITO.....	93
Figure A.3	J-V characteristic of best PSC based on MC-43 (a) and TPA (b) SAM molecules at 1 sun and dark conditions	94
Figure A.4	XPS surface spectrum of ITO/MC-45	95
Figure A.5	XPS surface spectrum of ITO/MC-54	95
Figure A.6	XPS surface spectrum of ITO/MC-55	96

List of Tables

Table 3.1	The corresponding binding energy of functional groups for ITO/MC-43 and ITO/TPA.....	35
Table 3.2	Averages values (mean \pm std. dev.) for the photovoltaic parameters of solar cells over 15 individual devices	39
Table 3.3	Photovoltaic parameters of the best performing devices based on different ITO electrodes with a scan speed of 40 mV s^{-1}	40
Table 4.1	Thermal properties of SAM molecules.....	49
Table 4.2	HOMO, LUMO and bandgap values of SAM molecules.....	51
Table 4.3	The corresponding bonding energy of functional groups of ITO/MC-45, ITO/MC-54, ITO/MC-55 and bare ITO.....	53
Table 4.4	Grain size distribution results of perovskite films surface.....	59
Table 4.5	Carrier lifetime at the interface of ITO/CsMAFA, ITO/PTAA/CsMAFA, ITO/MC-45/CsMAFA, ITO/MC-54/CsMAFA and ITO/MC-55/CsMAFA that obtained from TrPL.....	63
Table 4.6	Photovoltaic parameters of best performing devices.....	65

List of Abbreviations

AFM	Atomic Force Microscopy
Ag	Silver
Al	Aluminum
AM	Air Mass
BCP	Bathocuproine
Br ⁻	Bromide
CaTiO ₃	Calcium Titanium Oxide
C _{geo}	Geometric Capacitance
Cl ⁻	Chloride
Cs ⁺	Cesium
CV	Cyclic Voltammetry
DC	Differential Capacitance
DCM	Dichloromethane
DSC	Differential Scanning Calorimetry
DSSCs	Dye-Sensitized Solar Sells
ETL	Electron Transport Layer
EQE	External Quantum Efficiency
FA ⁺	Formammidinium
FESEM	Field Emission Scanning Electron Microscopy
FET	Field-Effect Transistor
FTO	Fluorine Tin Oxide
HI	Hysteresis Index
H ₂ O	Water Molecule
MPP	Maximum Power Point
HTL	Hole Transport Layer

HTM	Hole Transport Material
HOMO	Highest Occupied Molecular Orbital
I ⁻	Iodide
ITO	Indium Tin Oxide
J _{SC}	Short-Circuit Current
J-V	Current density–Voltage
k _B	Boltzmann Constant
KPFM	Kelvin Probe Force Microscopy
LUMO	Lowest Unoccupied Molecular Orbital
MA ⁺	Methylammonium
n _{id}	Ideality Factor
OLEDs	Organic Light-Emitting Diodes
OSC	Organic Solar Cells
Pb ²⁺	Lead
PCBM	Phenyl-C61-butyric acid methyl ester
PCE	Power Conversion Efficiency
PEDOT:PSS	poly(3,4-ethylenedioxythiophene) polystyrene sulfonate
PMAA	poly(methyl methacrylate)
PL	Steady-State Photoluminescence
PTAA	Poly(triarylamine)
PV	Photovoltaic
PSCs	Perovskite Solar Cells
RMS	Root-Mean-Square
SEM	Scanning Electron Microscopy
Si	Silicon
SRH	Shockley-Read-Hall Recombination
Sn ⁺	Tin
SAM	Self-assembly monolayer
Spiro-OMETAD	2,2',7,7'-Tetrakis[N,N-di(4-methoxyphenyl)amino]-9,9'-spirobifluorene
THF	Tetrahydrofuan

T_g	Transition Temperature
T_{des}	Decomposition Temperatures
TGA	Thermogravimetric Analysis
TrPL	Time-Resolved Photoluminescence
TPC	Transient Photocurrent
TPV	Transient Photovoltage
UV-vis	Ultraviolet-visible
V_{bi}	Built-in Potential
V_{oc}	Open-Circuit Voltage
WF	Work Function
XRD	X-Ray Diffraction
XPS	X-Ray Photoelectron Spectroscopy

List of Symbols

Φ	Light Intensity
Q	Elementary Charge
τ_1	Carrier Lifetimes
N	Charge
δ	Recombination Order
λ	Slope of Power-Law
α	Ideality factor
η	Power Conversion Efficiency

Chapter 1

Introduction

Energy consumption has become one of the main problems of humanity after the industrial revolution and the rise in world population. Fossil fuels-based energy resources are not sustainable, resulting environmental and health problems [1-3]. Its consumption leads to increasing greenhouse gases, especially CO₂ emission, which is expected to severe results in weather changes, global warming, sea-level rise, and changes in the ecosystem [4]. In addition to these problems, fossil fuels are not uniformly distributed and can only be found in particular regions of the Earth. This makes dependency of some nations on others and it is caused serious energy and political crisis during the last few decades [5, 6].

In order to solve these problems, intense research is carried out on renewable energy sources including hydroelectric power, geothermal energy, wind energy, and especially solar energy. Among these energy sources, solar energy is the best alternative because it is the only unlimited energy source and it is possible directly convert sunlight to electricity by using photovoltaic cells. However, converting efficient, cost-effective, and sustainable solar energy is a foremost challenge for this era. During the past decades, researchers have been working on many types of solar cells for efficient photovoltaic energy conversion from the sun.

Polycrystalline silicon (Si) based solar cells have been dominated the photovoltaic (PV) market since the first Si p-n junction discovered in 1954 at Bell Laboratories because of their high power conversion efficiency [7]. Nevertheless, this technology has a high cost and cannot be able to be produced on flexible substrates. Because of these reasons, next-generation solar cell technologies including organic solar cells

(OSCs), dye-sensitized solar cells (DSSCs), and perovskite solar cells (PSCs) etc. have been developed.

In a short time, the power conversion efficiency (PCE) of PSCs has increased from 3.8% to over 25.5% [8, 9]. This rapid improvement in PSC efficiency gets it close to Si technology and makes it the hottest PV technology topic.

1.1 Perovskite Solar Cells

Perovskite material had been known more than a century before it was used in solar cells as an absorber material. The first natural perovskite was found in the Ural Mountains in 1839 by Gustav Rose and it was named with the name of Russian mineralogist Lev Perovski [10]. The name perovskite refers to a group of materials with the same crystal structure as mineral perovskite, calcium titanium oxide (CaTiO_3), which has a chemical formula as ABX_3 . The lattice structure of perovskite mineral is shown in Figure 1.1, where A is organic or metal cation, B is metal cation and X is halide anions [11]. In the case of organic-inorganic halide perovskite, A is organic methylammonium (CH_3NH_3^+ , MA^+), formamidinium ($\text{NH}_2=\text{CH}_3\text{NH}_2^+$, FA^+), or metal cesium (Cs^+) [12, 13]; B is lead (Pb^{2+}) or tin (Sn^{2+}); and X is iodide (I^-), bromide (Br^-), and chloride (Cl^-) [14, 15].

The stability of the crystal structure of perovskite is usually determined by the Goldschmidt tolerance factor (t), which is expressed as in equation 1.1

$$t = \frac{R_A + R_X}{\sqrt{2} (R_B + R_X)} \quad (1.1)$$

Where R_A , R_B and R_X indicate the ionic radius of the corresponding ions on A, B and X sites, respectively. When $t = 1$, a perfect packing structure occurs. When t is $0.8 \leq t < 1$, a cubic structure like in Fig. 1.1 occurs [16, 17]. When it is very small, perovskite crystal structure will become a tetragonal or orthorhombic structure, it is also possible to become a cubic structure if it is treated with high temperature [18]. Crystal planes of low-dimensional perovskite are varying three types (100), (110),

and (111). Among those low-dimensional perovskites, the (100) orientation crystal plane is the most common one and is also most widely used in PV applications [19].

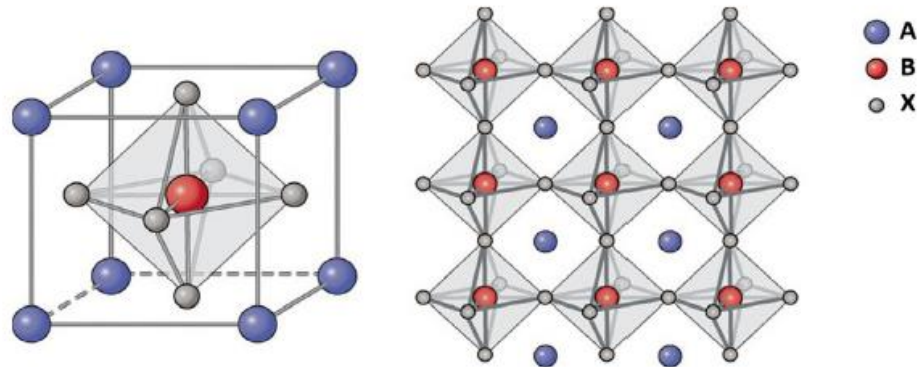


Figure 1.1: Crystal structure of perovskite [11]

The organic–inorganic metal halide perovskites have successfully been applied in photovoltaic applications due to their well-constructed lattice structure, which is providing extraordinary electrical and optical advantages, including high absorption coefficient, long carrier diffusion lengths, high charge carrier, high defect tolerant, and ease of preparation etc. [16, 20, 21]. The first perovskite solar cell was fabricated by Miyasaka and co-workers in 2009 [8]. It was used in dye-sensitized solar cell (DSSC) as an absorbing material instead of organic dye and got 3.8% PCE. However, owing to low PCE, devices were extremely instable because of liquid electrolyte which dissolved perovskite material. A step in the right direction occurred in 2012 when perovskite was used in solid-state DSSC and using spiro-OMETAD instead of liquid electrolyte [22]. With this architecture, 9.7% PCE was obtained. From then on, PSCs have become widespread [23].

1.2 Device Architectures of Perovskite Solar Cells

The configuration of PSCs can be divided into two main sandwich structures regular (n-i-p) and inverted (p-i-n) [24]. For both structures, perovskite absorber are sandwiched between a hole transport layer (HTL) and an electron transport layer

(ETL). Where, these three layers are placed between a metal electrode such as silver (Ag), gold (Au), and aluminum (Al) and a transparent electrode such as indium tin oxide (ITO) or fluorinated oxide (FTO).

In inverted PSCs, the perovskite absorber is deposited on top of the HTL, in other saying holes are collected at the transparent electrode (most often, ITO is used for inverted structure). On the contrary, perovskite layer is deposited on top ETL, in a regular structure, and electrons are collected at the transparent electrode (most often, FTO is used for regular structure).

Figure 1.2 shows the main device architectures of PSCs explained in this section. However, the regular structure can be classified into two different kinds, depending on use of a planer ETL or a mesoporous ETL [25].

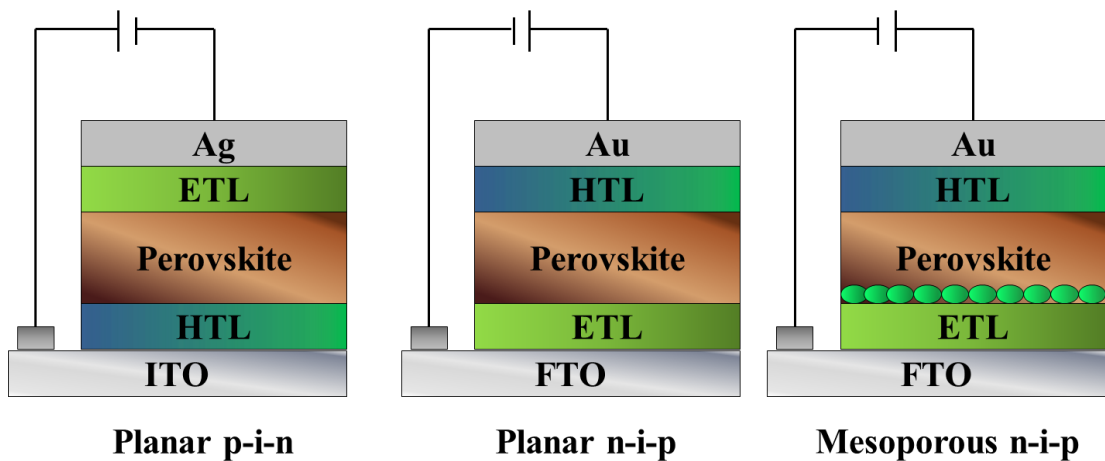


Figure 1.2: Device configuration of the most common used PSCs in literature

In this thesis, inverted perovskite solar cells are studied (Chapter 3 and Chapter 4). Therefore, the working principle of this structure is going to be explained only in the following section.

1.3 Working Principles of Perovskite Solar Cells

Figure 1.3 shows the working principle and a simplified charge transfer process of a PSC. At first, the perovskite layer is absorbed incident light (photons) to generate

charge carriers (electron-hole pairs or exciton). If the energy of photons is larger than the band gap of perovskite, electrons and holes are separated (1) and injected into corresponding transport layers (2). Electrons are injected into the conduction band (CB) of ETL and holes are injected into the highest occupied molecular orbital (HOMO) of HTL. Then electrons and holes are transferred to electrodes (3) and, finally, photocurrent is generated in the output of the circuit (Fig. 1.3) [24].

The injection of electrons and holes is directly related to the energy band structure of materials. Therefore, selecting ETL and HTL with proper energy band structures suitable for perovskite is essential. Another critical role of transport layers is charge selectivity or charge blocking. It is vital to prevent inappropriate charges are injected to electrodes, while allowing the right ones to pass. In the case of HTL, it is responsible for efficient hole injection from the perovskite/HTL interface and the blocking of the electrons. Meanwhile, an ETL is responsible for electron injection from the perovskite/ETL interface and prevents hole charge carriers. If, for instance, an electron reaches the metal contact, it will recombine non-radiatively with holes present at the contact [26, 27]. However, device performance will suffer due to these undesired photovoltage losses caused by recombination.

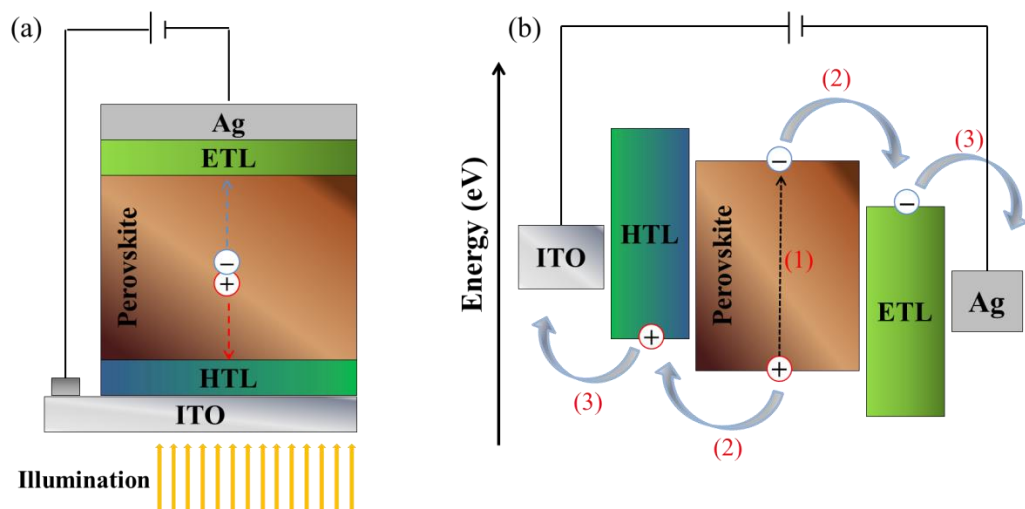


Figure 1.3: Schematic illustration of electrons and holes injection process in a p-i-n architecture perovskite solar cell

1.4 J-V Hysteresis in Perovskite Solar Cells

Current density–voltage (J – V) measurements of a PSC can be done with two different scan directions, which are described as forward scan (scan from J_{SC} to V_{OC}) and reverse scan (scan from V_{OC} to J_{SC}). It is critical to perform J – V measurements in these two ways in PSCs because measurement results vary based on J – V scan directions [28]. However, a gap occurs between forward and reverse scan of J – V curves and the curves cannot overlap (Fig. 1.4). This phenomenon is called hysteresis. The J – V hysteresis characteristic creates confusion in determining the actual performance of perovskite solar cells [29]. The dimensional hysteresis index (HI) is calculated using the equations below to quantify hysteresis [30, 31].

$$HI = \frac{J_{RS}(0.8 V_{OC}) - J_{FS}(0.8 V_{OC})}{J_{RS}(0.8 V_{OC})} \quad (1.2)$$

$$HI = \frac{PCE_{RS} - PCE_{FS}}{PCE_{RS}} \quad (1.3)$$

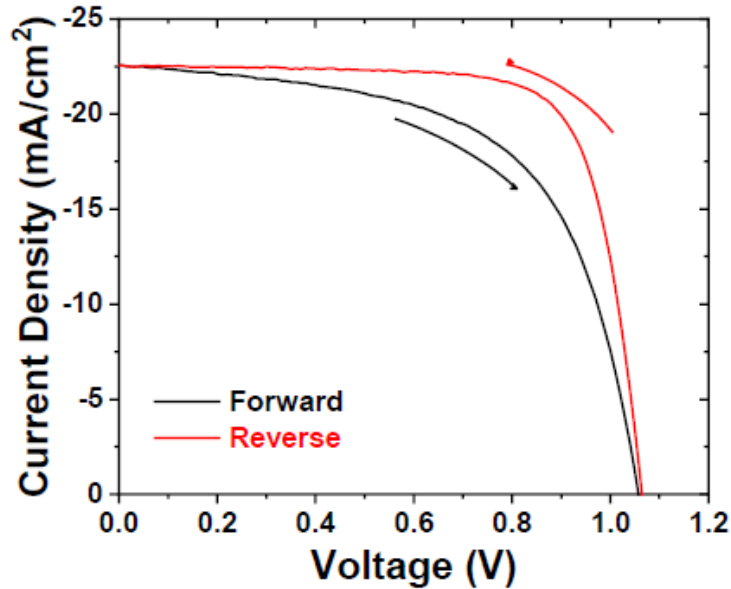


Figure 1.4: An example of forward/reverse scan J - V curves for hysteresis

The hysteresis phenomenon in PSCs was first reported by Snaith et al. in 2014 [28]. This study hypothesized that 2 possible reasons could be responsible for hysteresis: charge trapping and ion migration. After discovering $J-V$ hysteresis, many studies have been made to determine the origin of $J-V$ hysteresis and minimize it. However, it is still a subject under debate [32].

The $J-V$ hysteresis behavior has been reported to depend on many parameters; these parameters can be classified as internal and external parameters. The internal parameters for hysteresis are generally considered ion migration [33] and charge accumulation at the interfaces [34]. The external parameters are scan rate [35], device architecture, preconditions, interfaces, HTL, and ETL [36]. However, the majority believe that, ion migration and charge recombination at the perovskite/transport interface layers is responsible for $J-V$ hysteresis [37, 38]. According to theoretical calculations and experimental observations, migration of Γ^- , MA^+ , and Pb^{2+} ions and their vacancies accumulate at the interface of HTL and ETL under an external electrical field [39]. This accumulation at the interfaces results in an inner electric field at the perovskite film, which is at the opposite direction to external electric field. For instance, it is hypothesized that, the external electric field drives the migration of Γ^- to the HTL, while MA^+ is being drifted in the reverse direction [37, 39]. Due to the opposite direction of the external and internal electric field, ions have a slow redistribution process and this is suggested for $J-V$ hysteresis in PSCs [36].

The device architecture of PSCs also has a remarkable effect on hysteresis. Notably, an inverted (p-i-n) structure perovskite device generally has a negligible hysteresis when compared to a regular (n-i-p) structure [29, 36, 40, 41]. The reason is expected from the trapping/detrapping of defects within the TiO_2 , ZnO or the oxide/perovskite interface [42]. For inverted PSCs, PCBM or C_{60} are typically used as ETL material and PEDOT:PSS or PTAA as HTL material. Therefore, inverted PSCs shows more negligible hysteresis compared to TiO_2 based regular PSCs [29, 43].

1.5 Self Assembled Monolayers as Hole Transport Materials

Self-assembly monolayers (SAMs) are molecular single layers that spontaneously make chemical bonds on the surface of various substrates [44, 45]. SAM molecules form a very thin (1-3 nm) and highly ordered monolayer on the respective surfaces. The first report on SAM molecules was published by Bigelow et al. in 1946. They investigated the preparation of SAMs by adsorption on a clean metal surface [46, 47]. Typically, the structures of SAMs are divided into 3 main parts: the anchoring group (or head group), the spacer group (or tail) and the terminal group (or functional end group) (Figure 1.5).

- ❖ Anchoring group: the anchoring group is responsible for the interface between substrate and molecule. Various kind of anchoring groups allow users to select proper molecules for proper substrates. The most widely used class of SAM molecules is carboxylic acid (bonding on metal oxides), phosphonic acid (bonding on metal oxides), silanes (bonding on Si) and thiols (bonding on gold) [48]. The anchoring groups change surface work function (WF), contact resistance, and interface dipole [49].
- ❖ Spacer group: the spacer group is known as the molecule's backbone and it function as a bridge between the anchoring and terminal groups, besides molecular ordering responsibility. The length of the backbone plays a critical role in electronic conductivity from one contact to another and local optical properties [49].
- ❖ Terminal group: the terminal group has a vital role in the property of SAM molecules. It is responsible for the chemistry between molecule interface and overlayer because it becomes a new surface of the substrate [50-52]. Terminal groups change the surface energy, surface wettability, and topography of the top layer [53, 54]. For electronic application, the selection of terminal group is significant for the electronic coupling with overlayer.

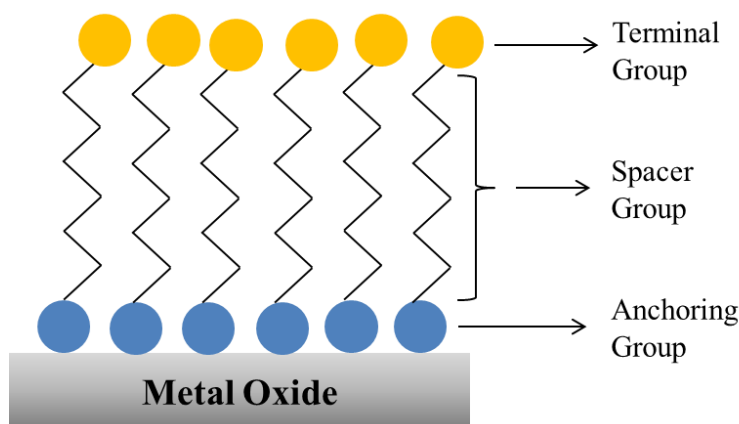


Figure 1.5: Schematic illustration of 3 main parts of SAM molecules

For the preparation of the SAM layer, immersion of the substrate into a solution containing the molecules is a widely used method of the adsorption of the SAM molecules on a surface. The film-forming process can be affected by external factors such as solvent concentration, time, and temperature [55]. It is suggested that a longer immersion time is required for a low concentration SAM solution. Similarly, a short immersion time is required for a high concentration SAM solution. Additionally, applying temperature accelerates the formation of the SAMs.

SAM molecules have varied adsorption processes depending on the anchoring group. In this thesis, SAMs with carboxylic acid anchoring group is used. Therefore, here, the adhesion mechanisms of the carboxylic acid anchoring group will be briefly explained. However, the carboxylic acid has two oxygen atoms, consequently mono- or bidentate binding mechanism is allowed when integrated with metal atoms [56]. The monodentate binding is formed by activated surface hydroxyl groups ($-OH$) and releasing a water molecule (H_2O). For bidentate, the hydrogen is transferred to the surface $-OH$ group and the second H_2O is released. Unlike the metal atom case, the only monodentate binding mechanism is possible while binding to a $-OH$ group surface [56].

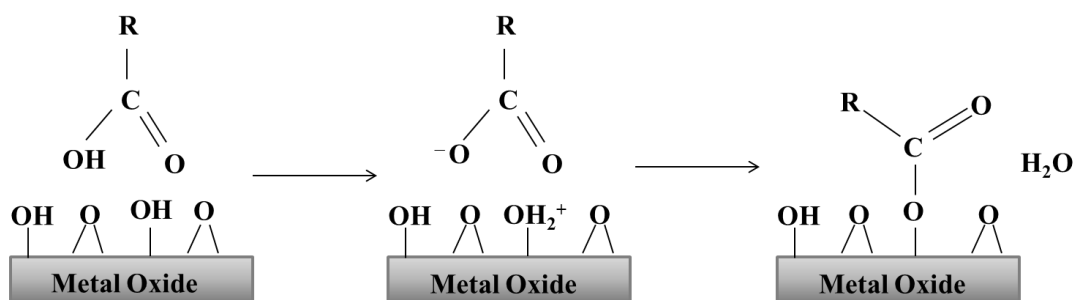


Figure 1.6: Illustration of a carboxylic acid molecule attaching on a metal oxide surface

SAM molecules offer an easy and effective way for interface modification of optoelectronic devices. It has extensive application fields because of providing a cost-effective and practical surface coating. It has been widely used in perovskite solar cells as an interface modifier in the last few years. SAMs have been used in organic light-emitting diodes (OLEDs), field-effect transistors (FETs), and dye-sensitized solar cells (DSSCs) before being used in PSCs [57, 58]. After these many studies undertaken on SAMs, it has been discovered that it could go to improve PSC performance due to energy level alignment, morphological adjustment, and trap passivation [59-61]. However, in 2018, two novel SAM molecules were first used as a hole transport material (HTM) instead of PEDOT:PSS in p-i-n configuration PSCs by our group. This study showed remarkable power conversion efficiency due to having good hole extraction properties. This work is given in **Chapter 3**.

Chapter 2

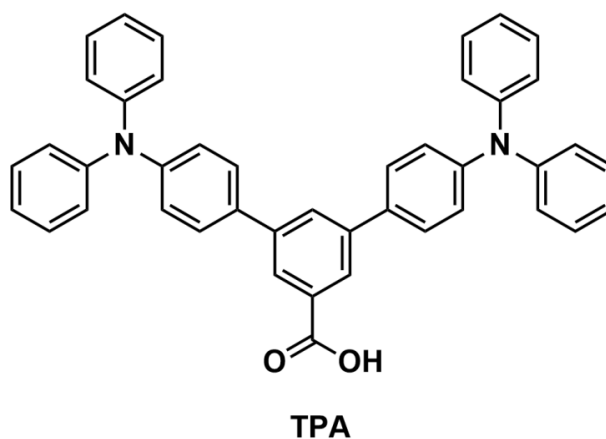
Experimental Methods and Characterizations Techniques

2.1 Small Molecules

2.1.1 4,4''-Bis(diphenylamino)-1,1':3',1''-terphenyl-5'-carboxylic [TPA]

TPA molecule was designed and synthesized by our group members Dr. Şerafettin Demić and Dr. Mustafa Can. It was used as hole transport layer in p-i-n type MAPI perovskite solar cell and published in [62]. Synthetic route and procedure of molecule was detailed in the paper.

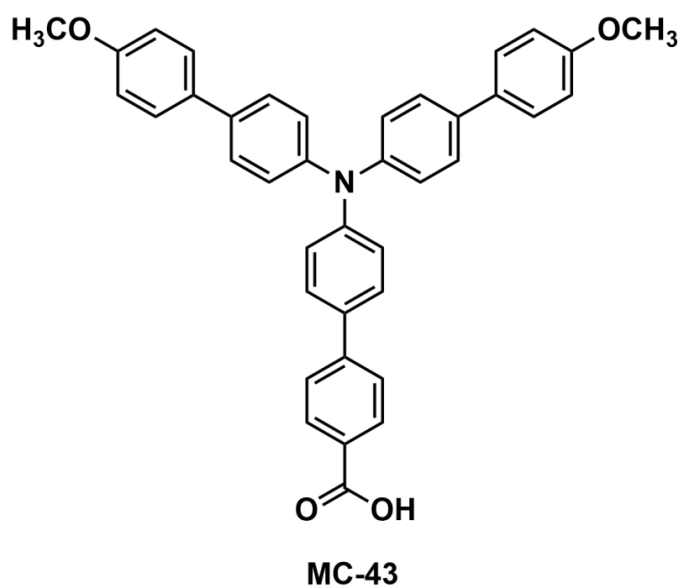
Chemical structure of TPA molecule is given as in below.



2.1.2 4'-[Bis(2',4'-dimethoxybiphenyl-4-yl)amino]-biphenyl-4-carboxylic acid [MC-43].

MC-43 molecule was designed and synthesized by our group members Dr. Şerafettin Demić and Dr. Mustafa Can. It was used as hole transport layer in p-i-n type MAPI perovskite solar cell and published in [62]. Synthetic route and procedure of molecule was detailed in the paper.

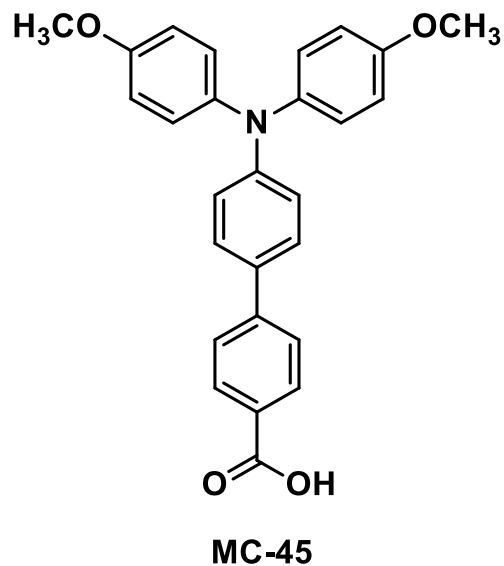
Chemical structure of MC-43 molecule is given as in below.



2.1.3 4'-(Bis(4-methoxyphenyl)amino)-[1,1'-biphenyl]-4-carboxylic acid [MC-45]

MC-45 molecule was designed and synthesized by our group members Dr. Şerafettin Demić and Dr. Mustafa Can. It was used as hole transport layer in p-i-n type CsMAFA perovskite solar cell. The manuscript is under preparation, not punished yet.

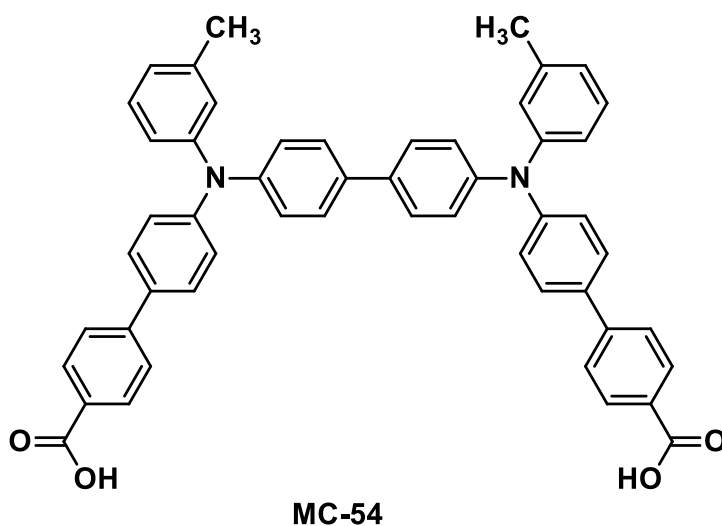
Chemical structure of MC-45 molecule is given as in below.



2.1.4 4',4'''-([1,1'-Biphenyl]-4,4'-diylbis(m-tolylazanediy))bis((1,1'-biphenyl)-4-carboxylic acid)
[MC-54]

MC-54 molecule was designed and synthesized by our group members Dr. Şerafettin Demić and Dr. Mustafa Can. It was used as hole transport layer in p-i-n type CsMAFA perovskite solar cell. The manuscript is under preparation, not published yet.

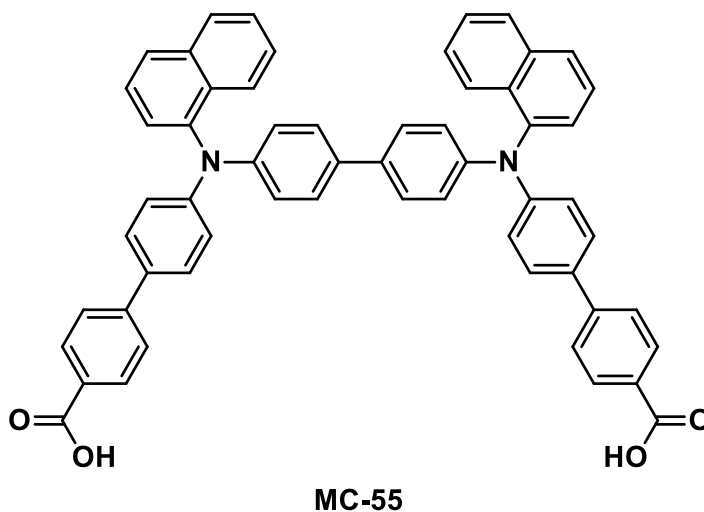
Chemical structure of MC-54 molecule is given as in below.



2.1.5 4',4'''-([1,1'-Biphenyl]-4,4'-diylbis (naphthalene-1-ylazanediy))bis((1,1'-biphenyl)-4-carboxylic acid)
[MC-55]

MC-55 molecule was designed and synthesized by our group members Dr. Şerafettin Demić and Dr. Mustafa Can. It was used as hole transport layer in p-i-n type CsMAFA perovskite solar cell. The manuscript is under preparation, not punished yet.

Chemical structure of MC-55 molecule is given as in below.



2.2 Device Fabrication of Perovskite Solar Cells

This section will describe inverted (p-i-n) MAPI and CsMAFA perovskite solar cell structures. The architectures of devices are shown in Fig. 2.1. In this thesis, different SAM molecules have been used as hole transport layer material for both architectures. In following, the fabrication techniques of both structures are detailed.

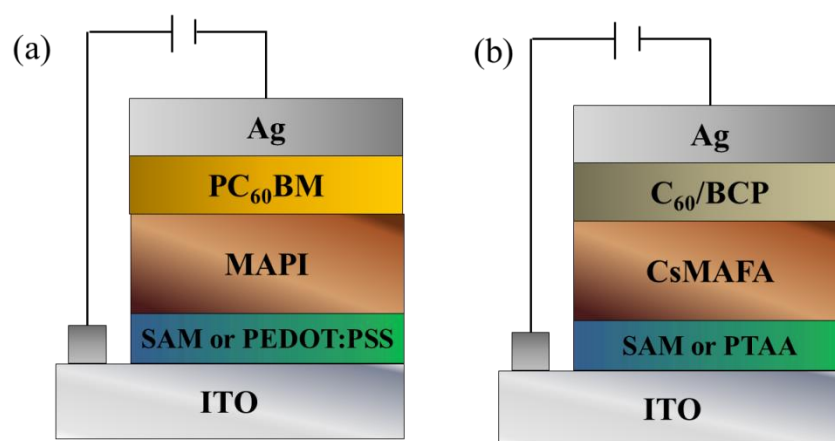


Figure 2.1: Schematic illustration of MAPI (a), and CsMAFA (b) perovskite solar cells device structures

2.2.1 Device Fabrication of MAPI Perovskite Solar Cell

ITO-coated glasses (Xinyan Technology Ltd, 15 Ω per square) were properly cleaned for 15 minutes by ultrasonication in water with HellmanexTM detergent, then in acetone and finally in isopropanol. Then cleaned layers are dried with a strong airflow before UV-O₃ treatment. All materials were purchased from Sigma-Aldrich and used as received unless differently specified.

TPA and MC-43 were dissolved in toluene (4×10^{-4} M) and kept stirring at 60 °C for two hours to increase their solubilities. ITO substrates were treated with UV/ozone for 30 min and subsequently immersed into SAM solutions for 4 hours at 45 °C. After that, substrates were rinsed with toluene to remove residual SAM molecules not covalently bonded onto the ITO surface. Alternatively, PEDOT:PSS (CleviosTM PV P AI4083, Heraeus) was deposited as the HTM at a 4500 rpm spin speed for 30 s,

achieving of 25–30 nm thickness. Finally, the substrates were transferred in a nitrogen-filled glovebox to complete the device fabrication.

For the preparation of perovskite solution, 460 mg of lead (II) iodide (PbI_2 , 99.995%, Alfa Aesar) was dissolved in (920:80) L of an anhydrous DMF:DMSO mixture while 50 mg of methylammonium iodide (MAI, Greatcell Solar Ltd) was dissolved in 1 mL of anhydrous isopropanol. The solutions were kept stirring for 2h. The perovskite was obtained with a two-step deposition method. In the first step, after filtering the solution with a $0.22 \mu\text{m}$ PTFE filter, $70 \mu\text{L}$ of PbI_2 was cast at 4000 rpm. After 60 s, $100 \mu\text{L}$ of MAI was dripped over the spinning substrate. The substrate was kept spinning for a further 30 s. Successively, substrates were moved directly onto a hotplate and annealed for 10 min at $100 \text{ }^\circ\text{C}$. The thickness achieved is around 350 nm.

After perovskite film preparation, the devices were stored in the glovebox overnight in the dark. Afterward, 20 mg of PC_{60}BM (Nano-C Inc.) was dissolved in 1 mL of anhydrous chlorobenzene, stirred for two hours and deposited via spin coating (static dispensing, $70 \mu\text{L}$) at 2000 rpm for 30 s achieving a thickness of around 60 nm. Finally, 120 nm of Ag (Kurt J. Lesker) was deposited by thermal evaporation under high vacuum (around 1×10^{-6} mbar). Figure 2.2 summarizes the device fabrication steps that explained above in detail.

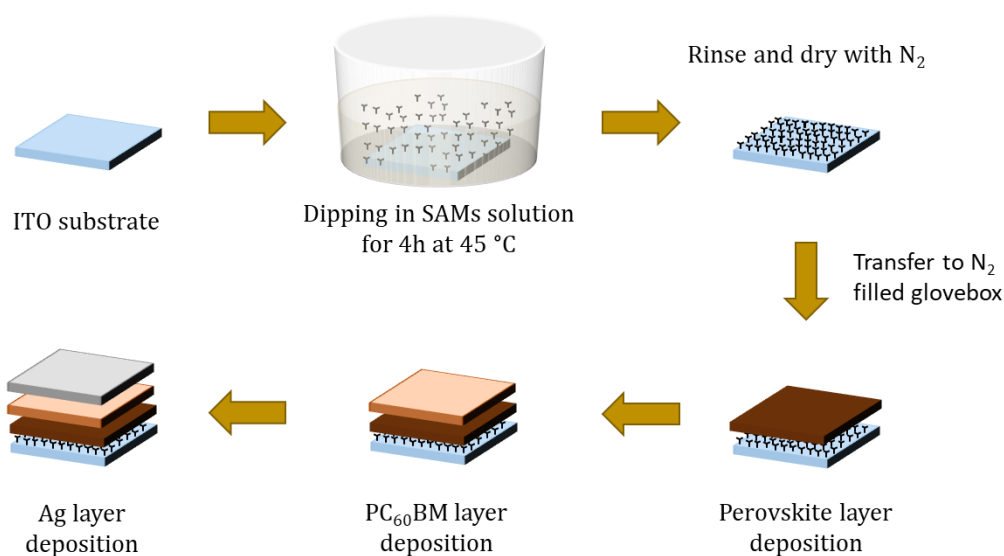


Figure 2.2: Illustration of device preparation steps. The ITO substrates are treated with UV-ozone before SAM deposition.

2.2.2 Device Fabrication of CsMAFA Perovskite Solar Cells

Patterned ITO glass substrates (1.5 cm x 1.5 cm) with sheet resistance $15 \Omega \text{ sq}^{-1}$ were cleaned in a three-step process that consisting of an ultrasonic bath for 15 min in DI water with HellmanexTM detergent, acetone and isopropanol, respectively. After the cleaning and drying process, ITO substrates were treated with UV/ozone cleaner for 30 min to activate the ITO surface and removing organic residues.

SAM molecules (MC-54 and MC-55) were dissolved in THF (0.1 mM) and MC-45 was dissolved in toluene (0.1 mM). Prepared SAM solutions were kept on a hot plate at 60 °C for 2h to increase their solubilities. Then, UV/ozone activated ITO substrates were immersed into SAM solutions and kept 6 h at 50 °C in ambient air. After 6 h, ITO substrates were removed and rinsed with THF (MC-54 and MC-55) and toluene (MC-45) to remove nonbonded SAM molecules onto the ITO surface. Alternatively, PTAA (Sigma Aldrich) was prepared for control devices as a hole transport layer (HTL). It was dissolved in anhydrous toluene (Sigma-Aldrich) at a concentration of 2 mg/mL. The deposition of PTAA was performed at 5000 rpm spin speed for 30 seconds and annealed on a hot plate at 100 °C for 10 minutes in a glove box.

Preparation of detailed triple-cation perovskite (CsMAFA) solution procedure was reported elsewhere [63]. To explain briefly, PbI_2 (1.5 M) and PbBr_2 (1.5 M) were dissolved in a mixture of anhydrous dimethylformamide (DMF) and dimethyl sulfoxide (DMSO, Sigma Aldrich, 4:1 volume ratio) and stirring on a hot plate at 50 °C for overnight. Then, PbI_2 and PbBr_2 stock solutions were added to formamidinium iodide (FAI, Dyenamo, 99.99%, 1.09:1 M ratio) and methylammonium bromide (MABr, Dyenamo, 99.99%) powders, respectively, to obtain FAPbI_3 and MAPbBr_3 solutions with a final concentration of 1.24 M. These two solutions then mixed in a volume ratio of 17:83. Finally, cesium cation was added from a 1.5 M CsI (Sigma Aldrich) solution in DMSO in a 5:95 volume ratio. This final perovskite solution was deposited on the HTLs by a spin coater at 3000 rpm for 40 sec. The last 15 sec of spinning 100 μl of anisole (Sigma Aldrich) was dropped on spinning substrates to promote fast solvent-removal forming a smooth and compact layer. After the spin-coating process, perovskite coated samples were annealed on a hot plate at 100 °C for 60 min. Then, 23 nm of C_{60} and 8 nm of BCP were deposited by thermal evaporation

on top of the perovskite with a rate of 0.2 -0.5 Å/s at a base pressure of 1×10^{-6} mbar. Finally, 100 nm of Ag was evaporated to complete the device structure. Figure 2.3 summarizes the device fabrication steps that explained above in detail.

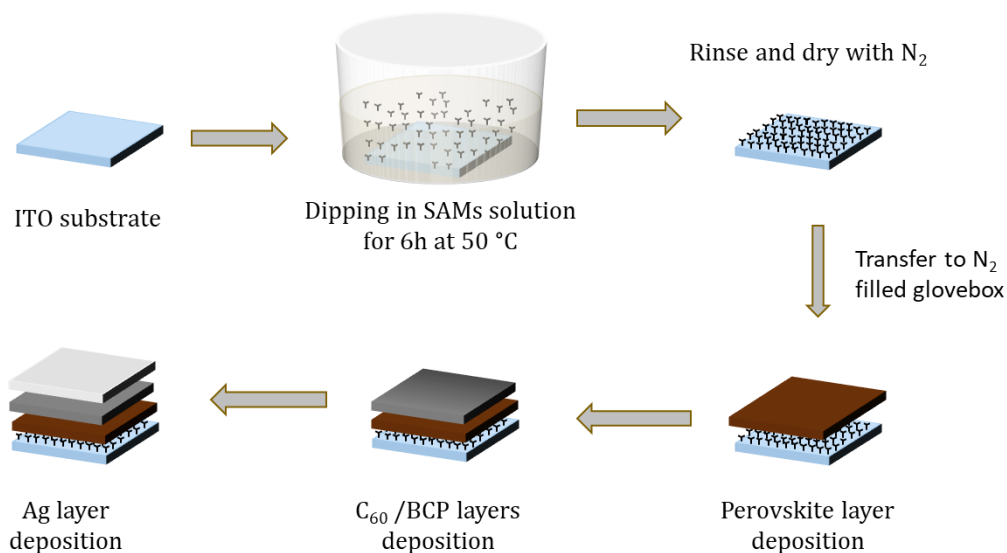


Figure 2.3: Illustration of device preparation steps. The ITO coated substrates were treated with UV/ozone before SAM deposition.

2.3 Characterization Techniques

2.3.1 Cyclic Voltammetry

For cyclic voltammetry (CV) measurements, a three-electrode system was used. All measurements were performed in a one component cell and equipped with a glassy carbon working-electrode, a platinum counter-electrode, and an Ag/Ag^+ reference electrode in acetonitrile solution at a concentration of 0.5 mM. The supporting electrode is a 0.1 M of tetrabutyl ammonium hexafluorophosphate (TBAPF_6) dissolved in dichloromethane (DCM) solvent.

HOMO levels of SAM molecules were obtained from the inflection point of cyclic voltammograms in the solution process and calculated from equation 2.1. Similarly,

SAM modified ITO's work function was determined from inflection point of CV and calculated from equation 2.1.

CV measurements were performed by a CH Instruments CH440b potentiostat.

$$E_{\text{HOMO}} = - (E_{1/2(\text{ox})} + 4.4) \text{ eV} \quad (2.1)$$

2.3.2 UV-vis Absorbance Spectroscopy

Ultraviolet-visible (UV-vis) spectrometer was performed to get absorbance spectra of SAM molecules in the solution phase. Solution absorption measurements were performed in tetrahydrofuran (THF) and toluene with a 1 cm path length quartz cell at room temperature in air.

Shimadzu UV spectrometer 1700 with an optical range between 190-1100 nm was used for this measurement.

2.3.3 Thermal Analysis

Thermogravimetric analysis:

Thermogravimetric analysis (TGA) determines the rate and the weight loss of a material as a function of temperature or time under a controlled atmosphere. In this characterization, TGA/STD A851 Mettler-Toledo equipment was chosen. The working temperature went from 30 to 600 °C at a scan rate of 10 °C/min under a nitrogen atmosphere. In this work, it is an important parameter to determine the decomposition temperature of SAM molecules to consider whether they will resist during the annealing process of perovskite layer.

Differential Scanning Calorimetry

Differential Scanning Calorimetry (DSC) gives information about physical and chemical changes of materials to determine glass transition temperature (T_g). In this work, DSC measurement was carried out in the DSC822e Mettler-Toledo

calorimeter. The working temperatures went from 30 to 450 °C performing three continuous cycles, at a scan rate of 10 °C/min in a nitrogen atmosphere.

2.3.4 X-Ray Photoelectron Spectroscopy

The X-Ray Photoelectron Spectroscopy (XPS) measurement was carried out by a Thermo Scientific K-Alpha equipment in a high vacuum chamber. XPS was used to analyse atomic bonds of SAM molecules on the ITO surface before and after modification.

2.3.5 Atomic Force Microscopy

The surface topography and roughness values of SAM modified ITO and unmodified ITO was characterized by a Nano-surf Easy Scan-2 Controller atomic force microscopy (AFM) with a non-contact mode.

Kelvin Probe Force Microscopy (KPFM) was used to determine surface potential differences of SAM modified and unmodified ITO substrates.

2.3.6 Contact Angle

Contact angle measurements were performed with a KSV Attension Theta Lite optical tensiometer used in sessile water (DI) drop experiment. It was performed by dispersing a water droplet on the substrates in the static state.

It was used to investigate the surface wettability of ITO substrates before and after modification with SAMs

2.3.7 Scanning Electron Microscopy

FEI Company Scios 2 field emission scanning electron microscopy (FESEM) was used to obtain surface images of perovskite films. All perovskite films were protected with poly(methyl methacrylate) (PMMA) to perform the measurements at ambient conditions (20 nm of PMMA was spin coated on perovskite). Focused Ion Beam (FIB) was used to obtain cross-section images of complete device layers.

2.3.8 X-Ray Diffraction

X-Ray Diffraction (XRD) was used to determine the crystal structure of perovskite films by a Bruker D8 Discover diffractometer. All perovskite films were protected with 20 nm PMMA to do measurements at ambient conditions.

2.3.9 Photoluminescence Measurements

To investigate possible paths of carrier recombination at the interface between perovskite and selective contacts, steady-state photoluminescence (PL) was used. Also, time-resolved PL was used to measure carrier lifetime from luminescence decays. These measurements were performed on an Edinburg Instruments LifeSpec-II with a PMT detector and 470 nm picosecond pulsed diode laser source. Before analysing the samples, all perovskite films were protected with ~20 nm PMMA to do measurements in ambient conditions.

2.3.10 Characterization of Perovskite Solar Cells

Figure 2.4 shows a typical J - V characteristic of a solar cell with the main electrical parameters. These parameters are open-circuit voltage (V_{OC}), short-circuit current (J_{SC}), fill factor (FF), and maximum power point (MPP or P_{max}) which are obtained from an illuminated perovskite solar cell. The PCE or solar cell efficiency is calculated from these parameters.

- **Short-circuit current density:** J_{SC} is the current through the external circuit when the voltage across the external circuit is zero. J_{SC} depends on various parameters such as the active area of the solar cell or incident light intensity.
- **Open circuit voltage:** V_{OC} is the maximum voltage available from a solar cell, and it occurs at the zero net current through from the solar cell.
- **Fill factor:** FF is the ratio between the maximum power output ($J_{MM} \times V_{OC}$) generated by a solar cell and the product of V_{OC} and J_{SC} (equation 2.2). The FF can be obtained graphically from J - V curve. It is defined from the ratio between the blue and grey rectangles (see Fig. 2.4).

$$FF = \frac{V_{MP} J_{MP}}{V_{OC} J_{SC}} \quad (2.2)$$

- **Power conversion efficiency:** PCE is the ratio between the maximum output power (P_{out}) that's generated from a solar cell and incident light power (P_{in}) (equation 2.3).

$$PCE = \frac{P_{out}}{P_{in}} = \frac{J_{SC} V_{OC} FF}{P_{in}} \quad (2.3)$$

The J - V measurements were performed by using a solar simulator (ABET 11000) and a source meter (Keithly 2400). The curves were registered under 1-sun irradiance (100 mW/cm^2 , AM 1.5G) calibrated with a silicon photodiode (NREL). The active area of the devices was 0.09 cm^2 .

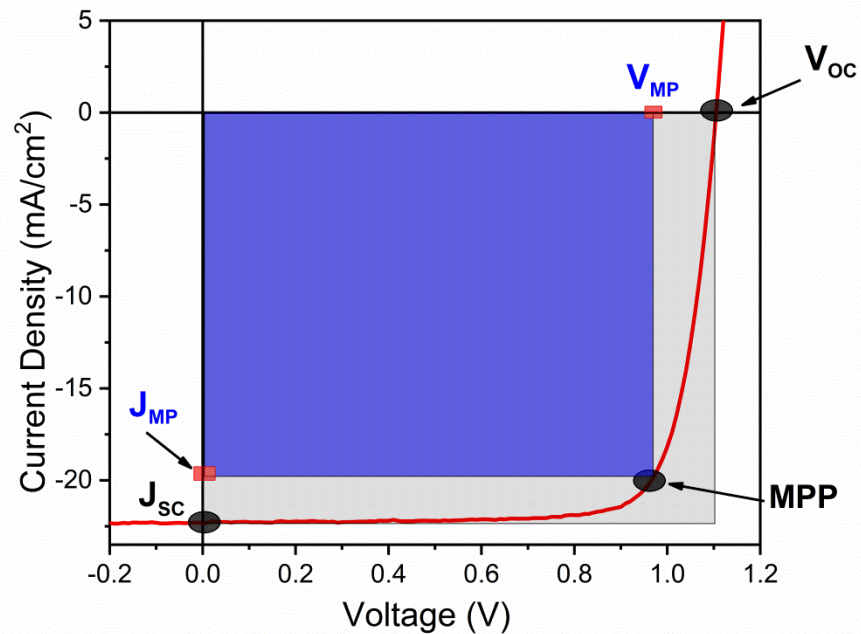


Figure 2.4: A typical J - V curve (red line) of perovskite solar cells with V_{OC} , J_{SC} , FF and MPP parameters. J_{MP} and V_{MP} are current and voltage at the MPP , respectively. The ratio between blue and light grey rectangles areas is the FF

The $J-V$ curve of PSCs can be obtained from two different scan sweeps which are namely forward (scan direction from J_{SC} to V_{OC}) and reverse (scan direction from V_{OC} to J_{SC}). Forward and reverse scans of PSC show different $J-V$ characteristics called hysteresis. $J-V$ hysteresis of PSC was explained in detail in section 1.4.

2.3.11 Effect of Light Intensity on Current Density and Open-Circuit Voltage

The intensity of the light changes solar cell parameters such as J_{SC} , V_{OC} , FF and PCE. For this purpose, different optical filters were used to obtain different light intensities (Φ). These optical filters allow less light to pass to solar cells from solar simulator (from 1 sun to dark). $J-V$ curves that obtain from different optical filters is shown in Figure 2.5.

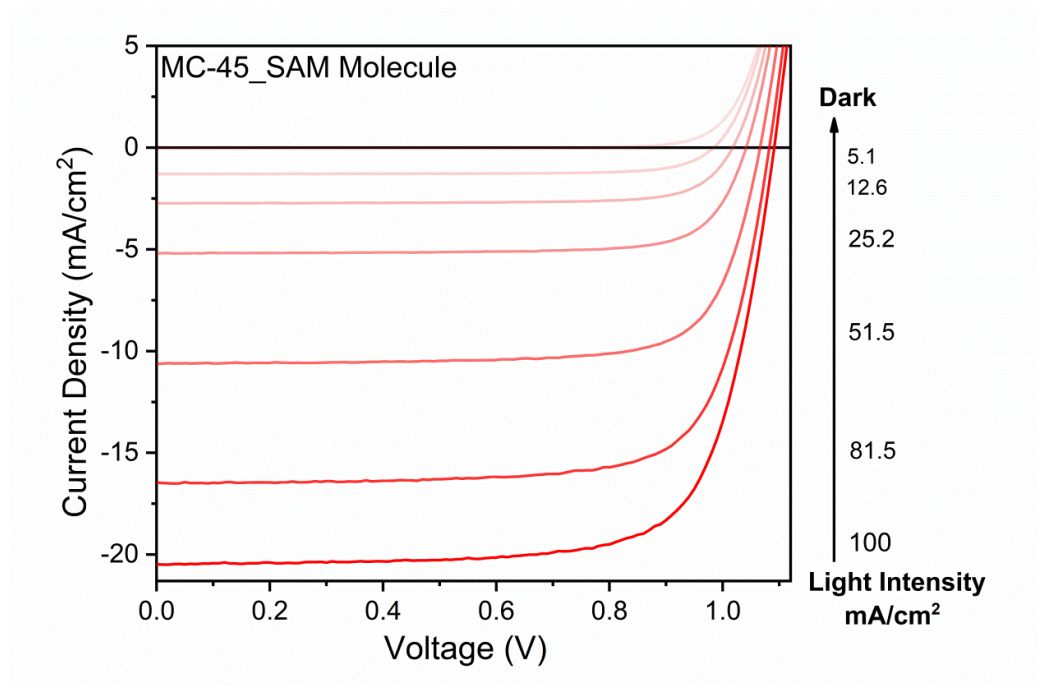


Figure 2.5: $J-V$ curves of a perovskite solar cell with MC-45 SAM molecule under different light intensities (from 1 sun to dark) on reverse condition

V_{OC} and J_{SC} values from each light intensity are extracted from $J-V$ curves of Fig. 2.5 and plotted as current density *versus* irradiance (Fig. 2.6a) and voltage *versus*

irradiance (Fig. 2.6b). In the case of J_{SC} dependence with light intensity, the J_{SC} is fitted to power-law dependence ($J_{SC} \propto \Phi$) and it is possible to estimate if there are any photocurrent losses or not under short circuit conditions. There are no photocurrent losses at the short circuit condition for an ideal device, if $\alpha = 1$ (Fig. 2.6a) [64].

For the case of V_{OC} dependence with light intensity, it is possible to calculate the ideality factor (n_{id}). For p-n junction, the ideality factor shows how much devices differ from ideal diode behavior. Typically, n_{id} value ranges from 1 to 2 [65]. If $n_{id} = 1$, it means band to band recombination (or bimolecular recombination) and if $n_{id} = 2$, it means Shockley-Read-Hall (SRH) recombination predominant (Fig. 2.6b) [66, 67].

Shockley and Read published the first $J-V$ equation for an ideal diode solar cell in 1952. The $J-V$ equation for the ideal solar cell is listed as follows:

$$J = J_{SC} - J_0 \left(e^{\frac{qV}{n_{id} k_B T}} - 1 \right) \quad (2.4)$$

Where J is net current, J_0 is constant, K_B is the Boltzmann constant, q is the elementary charge, V is the applied voltage and T is the operating temperature. The value of J is equal to '0' when the device is at the open-circuit voltage ($V = V_{OC}$ at the one sun test condition) under standard test conditions. So, equation 2.4 converted to equation 2.5.

$$J_{SC} = J_0 \left(e^{\frac{qV_{OC}}{n_{id} k_B T}} - 1 \right) \quad (2.5)$$

Finally, the diode ideality factor can be delivered from equation 2.6 as follow,

$$n_{id} = \frac{q V_{OC}}{k_B T \left(\ln \frac{J_{SC}}{J_0} + 1 \right)} \quad (2.6)$$

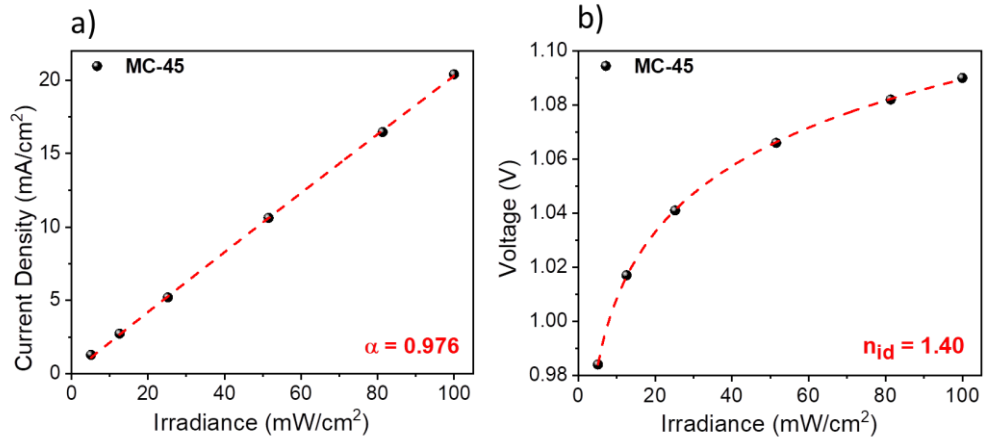


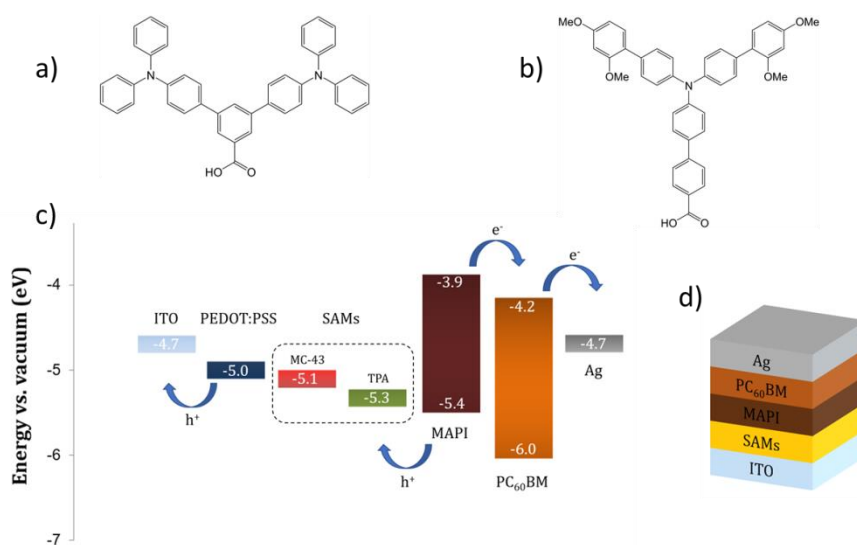
Figure 2.6: a) Current density dependence with the light intensity and b) open-circuit voltage dependence with the light intensity. Both figures obtained from reverse J - V curves of Figure 2.5

2.3.12 Stability Measurements of Perovskite Devices

The stability measurement setup is based on a high-power white LED source made at ICIQ mechanical workshop in which irradiance has been calibrated to 1 sun using a silicon reference. A Keithley 2400 was used for voltage-current measurement of the solar cells. A custom C++ code was developed for the automated data recording and pre-processing. The parameters extracted (time, J_{SC} , V_{OC} , FF and PCE) from the J - V curves for every 1 h and normalized to the start value. During the aging experiment, the cells were kept in the ultrahigh vacuum compatible sample holder and the temperature around the cells was measured as 45 °C.

Chapter 3

Self-Assembled Monolayers as Hole Transport Materials in MAPI Perovskite Solar Cells.



This chapter based on a published work: Yalcin et. al. Semiconductor self-assembled monolayers as selective contacts for efficient p-i-n perovskite solar cells; *Energy & Environmental Science*, 2019, 12, 230-237

Authors: Eyup Yalcin, Mustafa Can, Cristina Rodriguez-Seco, Ece Aktas, Rajesh Pudi, Werther Cambarau, Serafettin Demic, and Emilio Palomares

3.1 Abstract

Herein, we studied the use of two different Self Assembled Monolayer (SAM) molecules made of semiconductor hole transport organic molecules to replace the most common p-type contact, PEDOT:PSS, in p-i-n methylammonium lead iodide (MAPbI₃ or MAPI) perovskite solar cells (PSCs). The SAM molecule (MC-43) leads to a solar to energy conversion efficiency of 17.3%, which is among the highest efficiencies reported to date (23.06.2018) for PiN perovskite solar cells. The present finding highlights the potential of semiconductor based SAMs to fabricate stable and high performing planar PSCs.

3.2 Introduction

The research activity in hybrid lead based perovskite solar cells has increased enormously since the pioneering work of Miyasaka and co-workers [8]. For instance, the record in power conversion efficiency (PCE) has grown exponentially up to the current 22.7% [68]. Moreover, the fine-tuning of material composition had led to considerable improvements in device stability, [69, 70] encouraging its pre-industrialization. In this context, several research groups are committed to the development of new methods to grow and form homogeneous perovskite films [21, 71-76] with bigger grain size and limited defects in order to achieve highly reproducible devices with the maximum PCE. The use of different halides and organic-inorganic cations, mixed in such a way that it promotes the final perovskite structure, had led to a variety of materials with different valence and conduction band energy levels, and improved ionic and electronic transport capabilities [77]. Yet, the use of appropriate selective contacts [78], either organic molecules or metal oxides, also plays a crucial role in reducing charge recombination losses and maximizing the open-circuit voltage (V_{OC}) and thus the PCE.

The configurations of perovskite solar cells (PSCs) are frequently known as ‘regular’ (or n-i-p), where the perovskite absorber is deposited on top of the electron transport material (ETM), or ‘inverted’ (p-i-n) structures, where, on the contrary, the perovskite layer is on top of the hole transport material (HTM). The latter has been essentially developed to offer an alternative to the conventional structure [79] which

presents some drawbacks related to the charge transport materials, like the high processing temperature of TiO₂ (the most employed ETM) or the complex doping system of the HTM (usually spiro-OMeTAD or PTAA) as much as its cost. Nonetheless, the regular structure remains the most employed architecture and still holds the record efficiency in PSCs.

The inverted structure offers the advantage of low-temperature processing that allows the fabrication of perovskite modules on flexible substrates compatible with the roll-to-roll technology [80]. The typical inverted configuration, which has been already reported with efficiencies as high as 18% [21, 81], consists of poly(3,4-ethylenedioxythiophene):poly(styrenesulfonate) (PEDOT:PSS) as the HTM and [6,6]-phenyl-C(61)-butyric acid methyl ester (PC₆₀BM) or its corresponding C₇₀ derivative, PC₇₀BM, as the ETL. However, besides its excellent optoelectronic properties, PEDOT:PSS suffers from acidic and hygroscopic characteristics that can severely compromise the stability of the devices. Numerous inorganic alternatives to PEDOT:PSS, like nickel-based or copper based semiconductors [82], have been considered and successfully employed as the HTM in PSCs.

In this framework, self-assembled monolayers (SAMs) of organic molecules on electrodes surfaces have been considered as a valid alternative to conventional single-carrier transport layers [60, 61, 70, 83-85].

SAMs are small molecules that can be chemically attached to a surface (typically a metal or a metal oxide) and form extremely thin and stable layers. Besides their facile synthesis and deposition, the main advantage of SAMs is the ability to tune the electrical properties of the surface on which they are attached. This ability allows modulating the work function (WF) of a metal oxide, working as an electrode in a solar cell, in order to align it with the energy level of the photo-excited quasi-Fermi levels of the active layer.

This fact is a key point to ensure an ohmic contact at the interface and to maximize the V_{OC} . In the literature, the number of successful uses of SAMs in PSCs is scarce. Zuo *et al.* [60] demonstrate that an extremely thin layer of propanoic acid-based SAMs attached on top of a ZnO ETM can significantly increase the device PCE due to a better energy alignment with the perovskite LUMO and improved film

crystallinity. Yang and co-workers [86] successfully employed (3-aminopropyl) triethoxysilane (APTES) as a SAM material to modify the SnO₂ ETM, achieving 18% efficiency in a planar NiP PSC. Likewise, in our previous work we proved that the use of simple boronic acid-based SAMs, for coating the compact TiO₂ surface, is able to improve the photovoltaic properties of MAPbI₃ or MAPI PSCs [60]. In this work, we moved one step further and together with the property of being capable to form organized molecular layers we introduced the semiconductor feature for efficient transport of electronic holes. Our synthesised molecules, namely TPA and MC-43, are depicted in Fig. 3.1a and 3.1b, and are directly assembled at the indium doped tin oxide (ITO) electrode as surface modifiers to enhance hole extraction in inverted PSCs.

We studied the influence of the SAMs on the surface wettability, the perovskite formation and the photovoltaic performance of the solar cells. Our results show that it is possible to obtain high efficiencies in p-i-n perovskite based solar cells without the need of any inorganic metal oxide or semiconductor polymer as the HTM.

3.3 Results and Discussion

3.3.1 SAM modification of the ITO surface

Figure 3.1d shows a schematic device structure of a p-i-n type planar MAPI PSC composed of a transparent conductive ITO layer followed by a SAM modification layer, MAPbI₃, PC₆₀BM and finally a silver electrode. The SAM coating onto ITO is obtained with a straightforward procedure, consisting of submerging the substrate into a solution containing the molecule for an appropriate time, enough for the monolayers to attach to the ITO surface and form a compact and ordered film (device fabrication is described in detail at the corresponding chapter).

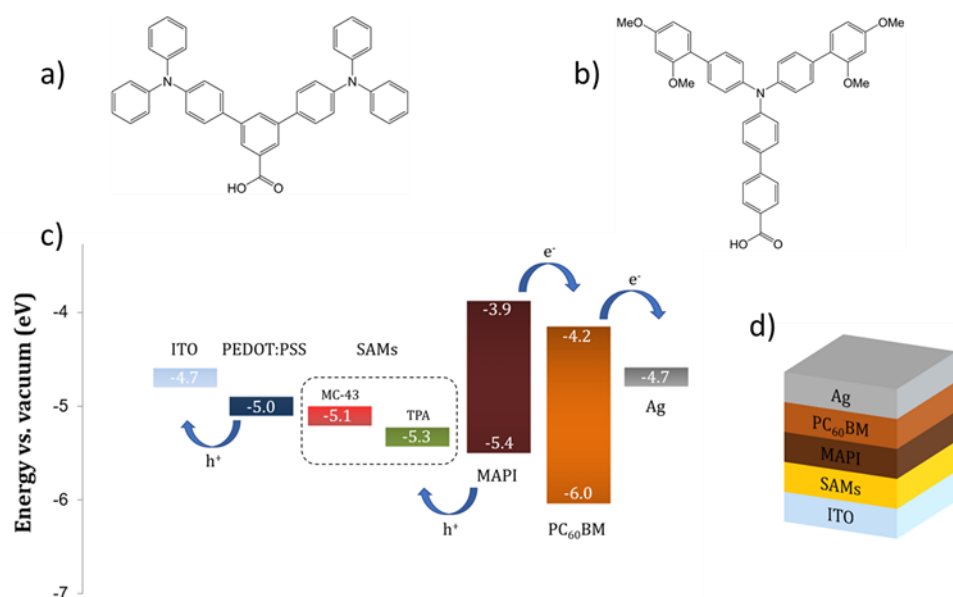


Figure 3.1: The molecular structure of (a) TPA and (b) MC-43. (c) Energy levels of the PSC materials employed in this study. (d) Layered structure of the SAM based device

Cyclic voltammetry was used to determine the electrochemical behaviour of TPA and MC-43 coated ITO surfaces. The new energy level (HOMO) of TPA and MC-43 modified ITO was determined as 5.33 eV and 5.11 eV, respectively, from the inflection point of the cyclic voltammograms (see Fig. 3.2) and calculated from equation 3.1. In accordance with energy level alignment of electronic states (see Fig. 3.1c) SAMs modification leads to alignment of work function of ITO at lower energy level. It is worth noting that the presence of electron-donating groups coupled to the triphenylamine backbone reduces its oxidation potential. This is a possible explanation for the 0.2 eV difference in the HOMO level between ITO/MC-43 and ITO/TPA surfaces.

$$E_{\text{HOMO}} = -(E_{1/2(\text{ox})} + 4.4) \text{ eV} \quad (3.1)$$

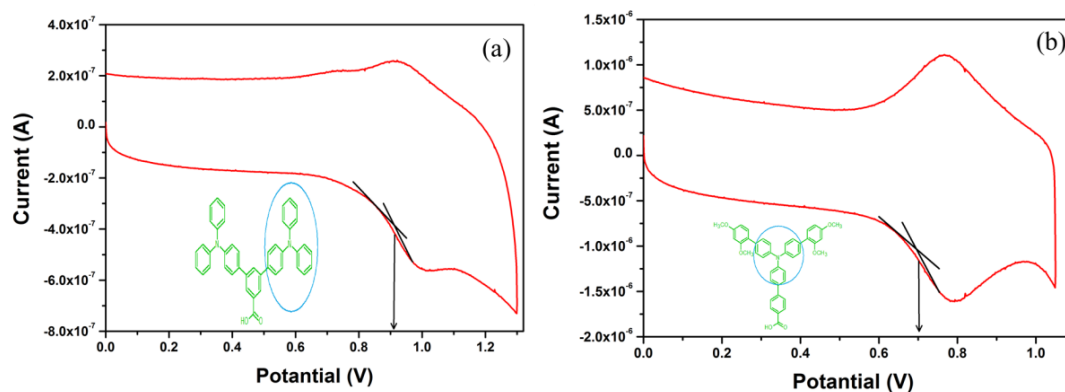


Figure 3.2: Cyclic voltammograms of ITO/TPA (a) and ITO/MC-43 (b)

The surface wettability of the ITO coated substrate before and after modification with the SAMs was investigated by measuring the contact angle in a sessile water drop experiment. It is well known that the ITO surface has a hydrophilic character because of hydroxyl groups consist on its surface. The contact angle on a bare ITO surface (i.e. without SAM coating) was estimated as 53.61° as shown in Fig. 3.3. The same picture shows, as a comparison, that TPA and MC-43 modified ITO surfaces became more hydrophobic (around 85° and 90°) with the molecules forming a barrier interface surface between ITO and the fluid.

Topographical atomic force microscopy (AFM) images of SAM modified samples were taken to confirm that the SAMs were effectively attached to the ITO surface (see Fig. 3.3d-f). Root-mean-square (RMS) values of bare ITO, ITO/TPA and ITO/MC-43 are 2.0 nm, 4.5 nm and 3.5 nm, respectively. Surface roughness values obtained for SAM modified ITO surfaces differ from bare ITO suggesting once again that ITO surfaces are covered by SAM molecules.

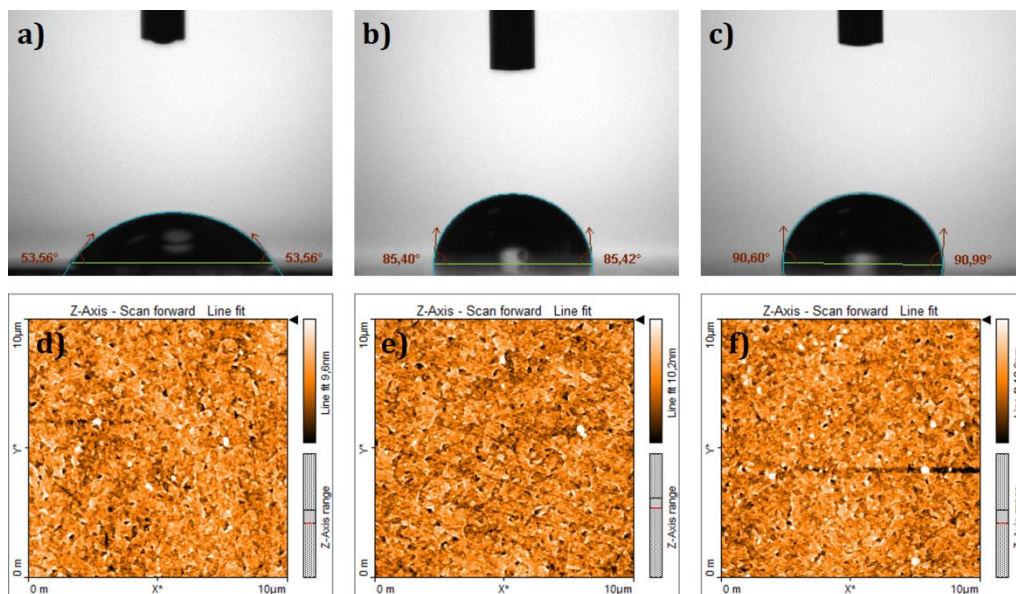


Figure 3.3: Top: Contact angle measurements on the (a) bare ITO surface, (b) ITO/TPA surface and (c) ITO/MC-43 surface. Bottom: Surface topographical AFM images of (d) bare ITO, (e) ITO/TPA and (f) ITO/MC-43

The X-ray photoelectron spectroscopy (XPS) was used to determine chemical compositions of modified ITO surfaces coated with MC-43 and TPA molecules. Fig. 3.4 shows the survey spectrum of C1s, O1s and N1s for ITO/MC-43 and ITO/TPA coatings, respectively. The peaks observed in the survey spectra for MC-43 are for C1s, O1s and N1s with binding energies of 284.08 eV, 529.32 eV and 398.94 eV, respectively [84, 87]. Approximately the same results are obtained for TPA.

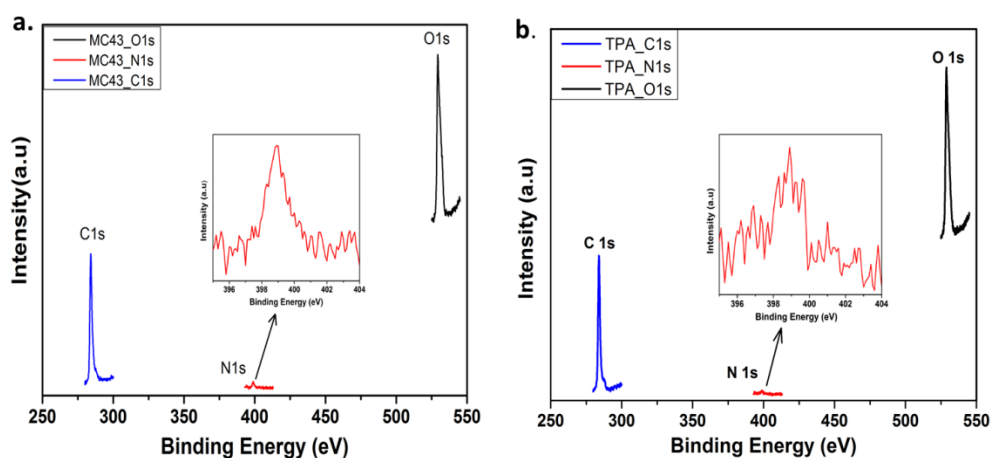


Figure 3.4: XPS Survey Spectrum of C1s, O1s and N1s for ITO/MC-43 (a) and ITO/TPA (b)

To analyse the atomic bonds formed by carbon and oxygen atoms on the ITO surface after the formation of SAMs, high resolution spectra of C1s and O1s were fitted and presented in Fig. 3.5. The peaks of C1s for MC-43 on ITO at 284.08, 285.43, and 287.41 eV and for TPA on ITO at 283.95, 284.60 and 287.58 eV are attributed to C—C or C—H, C—O—C and O—C=O, respectively [87]. The peaks assigned to ester bonding (O—C=O) at 287.41 and 287.58 eV indicate the formation of strong covalent bonds between the carboxylic acid (—COOH) head group of MC-43 and TPA SAM molecules and hydroxyl groups (—OH) present on the surface of ITO (Fig. 3.5a and c).

More detailed and fitted high resolution XPS spectra of O1s for MC-43 and TPA are given in Fig. 3.5b and d. The peaks observed at 529.32 and 530.96 eV are assigned to the ITO/MC-43 surface and these signals correspond to lattice oxide O_2^- and C=O groups, respectively. Almost the same peaks are obtained from the ITO/TPA surface with the values of 528.77 and 530.12 eV [84]. The corresponding binding energies of functional groups for ITO/MC-43 and ITO/TPA are listed as in Table 3.1.

Moreover, high-resolution survey spectra of bare ITO are given in Fig. A.1. High-resolution survey spectra of C1s and O1s were fitted (Fig. A.1a and A.1b) to analyse the atomic bonds of carbon and oxygen atoms on the ITO surface. The peaks of C1s at 284.97, 285.70 and 288.50 eV are attributed to C—C or C—H, C—O—C and O—C=O, respectively. The peaks of O1s at 530.01 and 531.50 eV are corresponding to lattice oxide O_2 (present on ITO surface) and C=O group, respectively. However, Figure A.2 shows the survey spectra of bare ITO. The measured bands correspond to C1s, In3d, Sn3d and O1s with binding energies of 285.2, 445.01, 487.07 and 531.03 eV, respectively. As expected, without SAM's there is not a band for N1s.

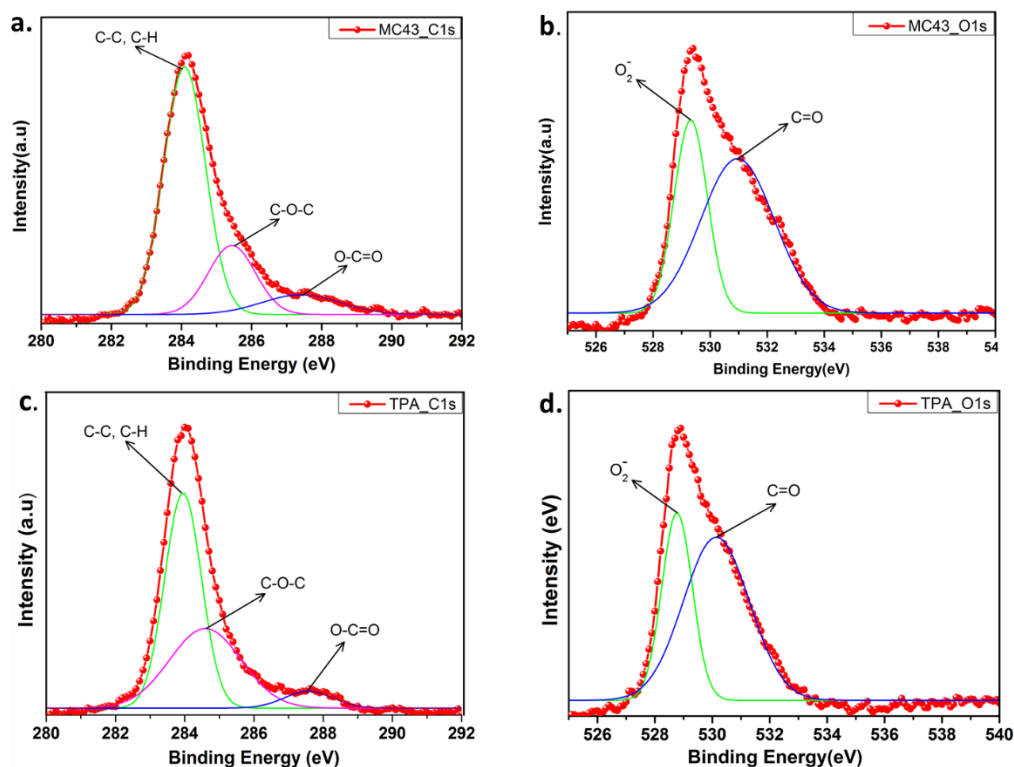


Figure 3.5: The XPS high resolution survey spectra of C 1s (a) and O 1s (b) for ITO/MC-43. The XPS high resolution survey of C 1s (c) and O 1s (d) for ITO/TPA

Table 3.1: The corresponding binding energy of functional groups for ITO/MC-43 and ITO/TPA

Samples	O1s (eV)		C1s (eV)			N1s (eV)
	O_2^-	$C=O$	$C-C/C-H$	$C-O-C$	$O-C=O$	
ITO/MC-43	529.32	530.96	284.08	285.43	287.41	398.94
ITO/TPA	528.77	530.12	283.95	284.60	287.58	398.89

Figure 3.6 shows the high resolution surface spectra of N1s for ITO/MC-43, ITO/TPA and bare ITO. The binding energy peak of N1s for ITO/MC-43 and ITO/TPA are around 400 eV. Bare ITO does not contain 'N' element therefore it does not have any peak around 400 eV. The absence of 'N' peak on bare ITO whereas its presence on SAM modified ITO surfaces confirms that ITO substrates were successfully covered by SAM molecules.

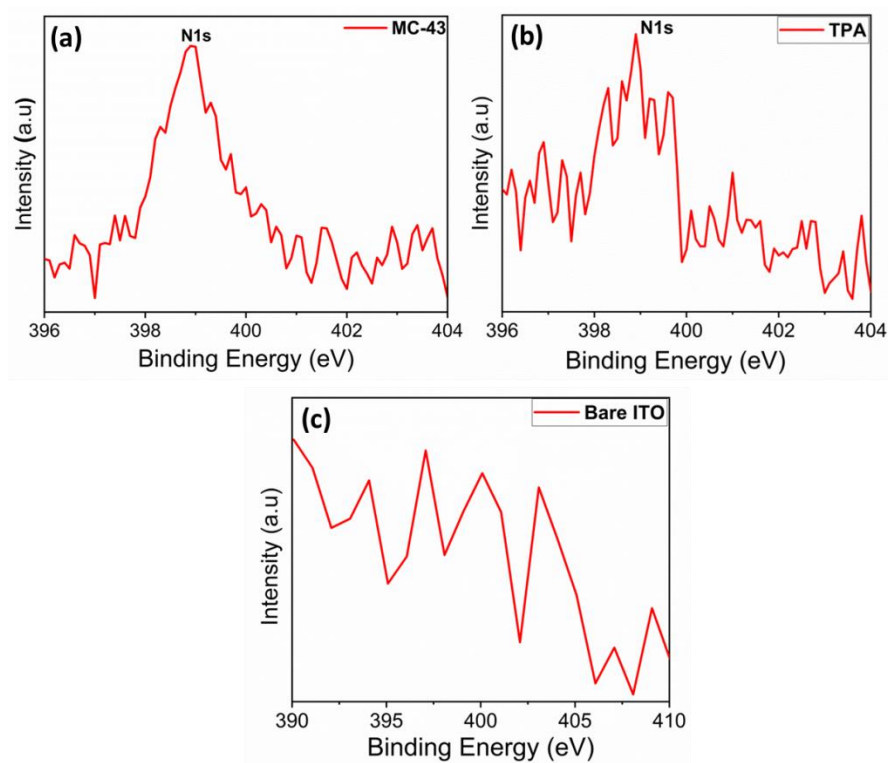


Figure 3.6: High resolution surface spectra of N1s for ITO/MC-43 (a), ITO/TPA (b) and bare ITO (c)

Moreover, we recorded perovskite film images (Fig. 3.7) using scanning electron microscopy (SEM). As can be seen, the use of PEDOT:PSS (Fig. 3.7b) reveals a more smooth ITO surface where the ITO grains cannot be distinguished. Yet, when the organic molecules are deposited (Fig. 3.7c and d) the ITO surface is still rough and the nanocrystals can be seen. Nonetheless, much of the nano space between ITO grains is covered. It is feasible that a rougher surface improves the contact between the electrode and the perovskite layer. Furthermore, the molecules at the SAM will provide a favourable dipole moment for efficient charge collection at the ITO electrode.

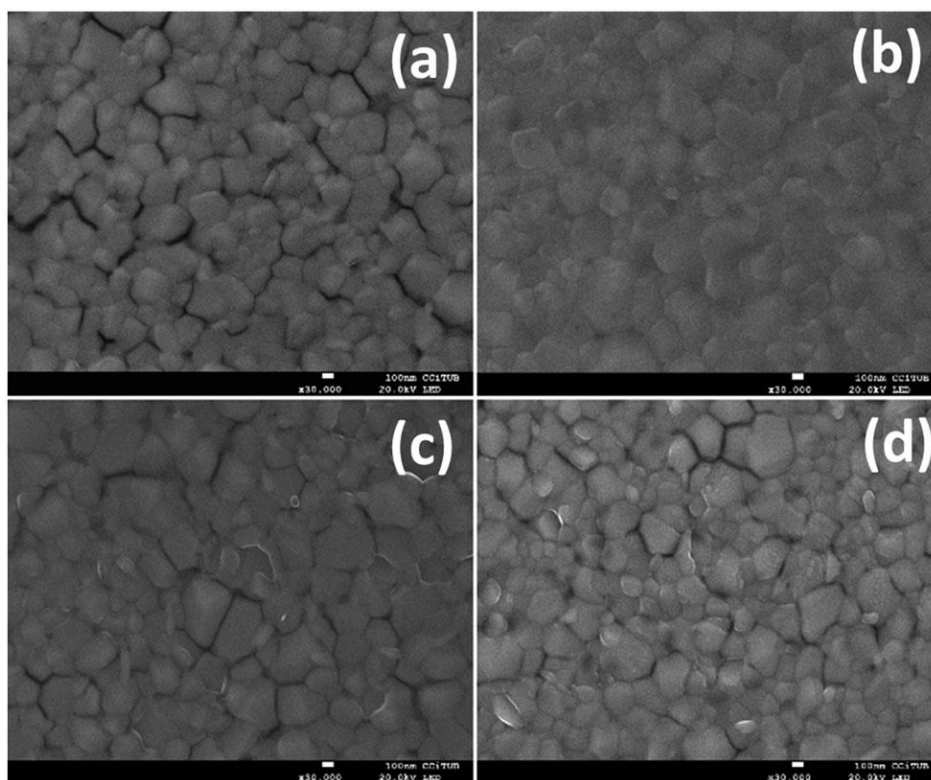


Figure 3.7: Morphology of the perovskite films on top of the modified and nonmodified ITO surface: (a) bare ITO; (b) ITO/PEDOT:PSS; (c) ITO/TPA; and (d) ITO/MC-43

3.3.2 Photovoltaic Performance

Figure 2.2 illustrates the complete device fabrication steps, explained in detail in the Experimental section (Chapter 2), in which the perovskite and the fullerene are deposited via spin coating and the final Ag electrode by means of thermal evaporation under high vacuum. As a comparison, we fabricated similar solar cells with exactly the same perovskite composition and thickness with PEDOT:PSS coated ITO instead of SAMs and, alternatively, without any coating (bare ITO sample). The current density-voltage ($J-V$) characteristics of the best devices are shown in Fig. 3.8.

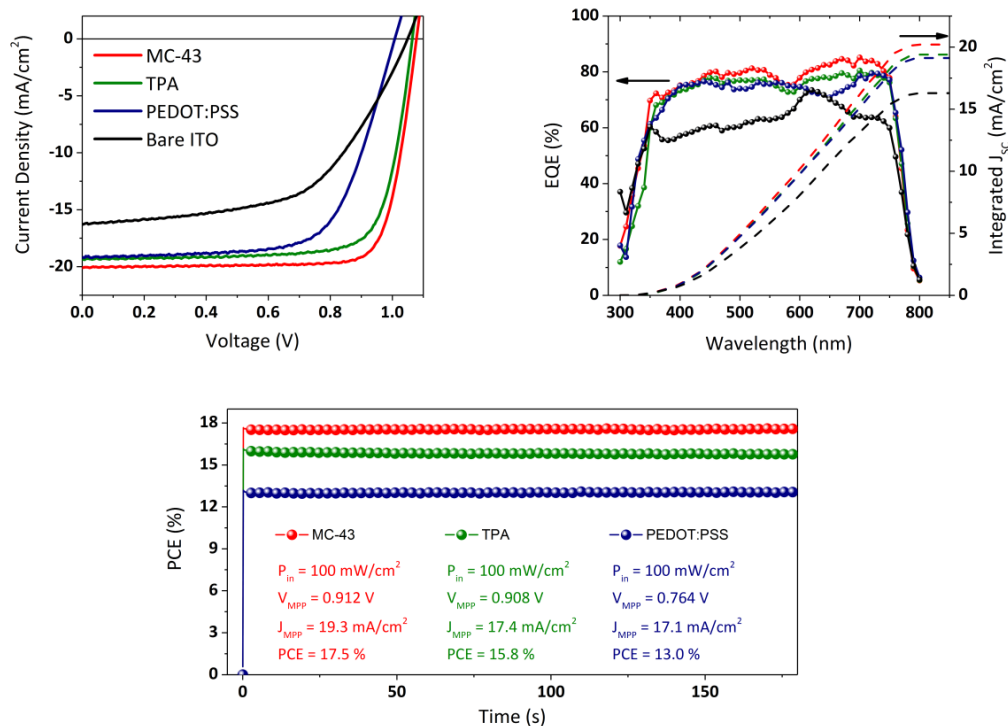


Figure 3.8: Top: J - V characteristics of the best devices, measured at 1 sun in the reverse voltage scan direction at a speed of 40 mV s^{-1} , and EQE spectra of the same cells. Bottom: PCE tracking of the best devices under continuous illumination, obtained by registering the current density at the applied voltage corresponding to the maximum power point (MPP)

These measurements were carried out under 1 sun illumination conditions (AM 1.5G, 100 mW cm^{-2}) and performing the voltage scan in the direction V_{OC} to J_{SC} (reverse sweep) at a scan rate of 40 mV s^{-1} . Compared to bare ITO devices, the SAM based cells perform much better especially in terms of FF and J_{SC} , leading to significantly higher PCEs. While the J_{SC} for the PEDOT:PSS device is comparable with the one obtained with SAMs, the FF is below 70% leading to a maximum PCE of 13.0% with an average value of 12.3%. Average values of photovoltaic parameters are summarized in Table 3.2. And a statistic distribution of photovoltaic performances of J_{SC} , V_{OC} , fill factor (FF) and PCE is shown in Fig. 3.9.

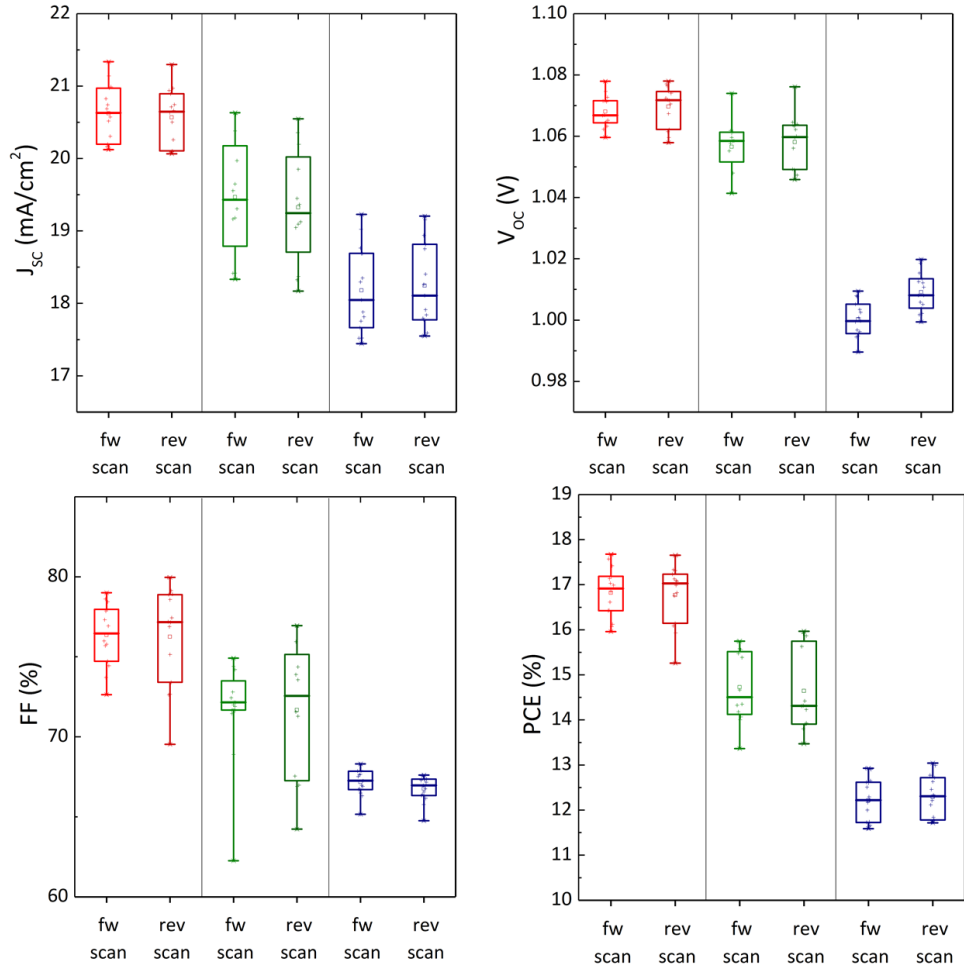


Figure 3.9: Statistics of photovoltaic parameters for PSCs based on MC-43 (red), TPA (green) and PEDOT:PSS (blue) recorded at 1 sun for both forward and reverse voltage scan

Table 3.2: Averages values (mean \pm std. dev.) for the photovoltaic parameters of solar cells over 15 individual devices

Sample	Scan Direction	J_{sc} (mA/cm ²)	V_{oc} (V)	FF (%)	PCE (%)
PEDOT:PSS	Forward	18.18 \pm 0.59	1.000 \pm 0.006	67.17 \pm 0.83	12.21 \pm 0.47
	Reverse	18.24 \pm 0.59	1.009 \pm 0.006	66.75 \pm 0.78	12.29 \pm 0.47
TPA	Forward	19.47 \pm 0.82	1.057 \pm 0.009	71.63 \pm 3.34	14.72 \pm 0.79
	Reverse	19.32 \pm 0.80	1.058 \pm 0.009	71.68 \pm 4.33	14.64 \pm 0.93
MC-43	Forward	20.62 \pm 0.40	1.068 \pm 0.005	76.36 \pm 1.97	16.82 \pm 0.56
	Reverse	20.57 \pm 0.39	1.070 \pm 0.007	76.25 \pm 1.97	16.77 \pm 0.67

MC-43 scores a record efficiency of 17.3% with an average of 16.8% while TPA reaches 15.8% as the maximum with an average of 14.6%. The extremely high FF

might be related to an optimal formation of the perovskite layer on top of the SAM modified ITO. All the photovoltaic parameters related to the champion devices are summarized in Table 3.3. Apart from the bare ITO samples, all cells present negligible or no hysteresis in the J - V curves (see Fig. 3.10) leading to an excellent consistency of photovoltaic parameters regardless of the scan direction.

In addition, J - V characteristic of the best solar cells based on MC-43 and TPA at 1 sun and dark conditions was given as in Fig. A.3.

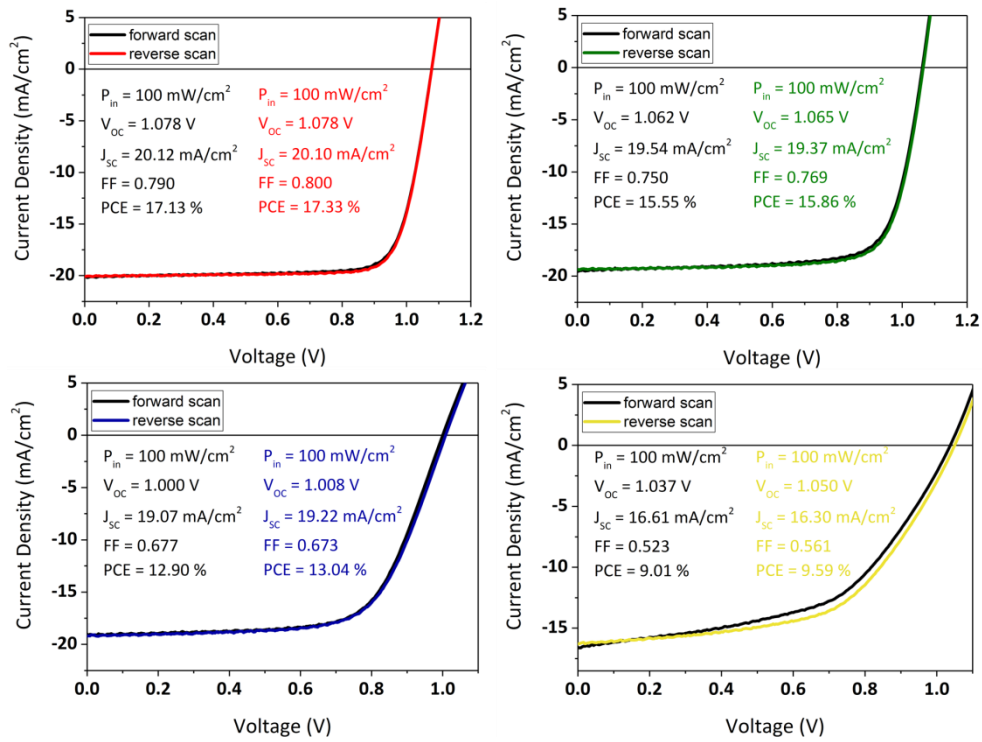


Figure 3.10: J - V characteristics of best PSC based on MC-43 (red), TPA (green), PEDOT:PSS (blue) and bare ITO (yellow) at 1 sun. Both forward and reverse scans have been performed at a scan rate of 40 mV/s

Table 3.3: Photovoltaic parameters of the best performing devices based on different ITO electrodes with a scan speed of 40 mV s⁻¹

Sample	J_{sc} (mA cm ⁻²)	V_{oc} (V)	FF (%)	η (%)
Bare ITO	16.3±0.2	1.05±0.04	56.1±0.3	9.59±0.3
PEDOT:PSS	19.2±0.2	1.01±0.04	67.3±0.3	13.0±0.3
TPA	19.4±0.2	1.06±0.4	76.9±0.3	15.9±0.3
MC-43	20.1±0.2	1.08±0.4	80.0±0.3	17.3±0.3

As observed by several research groups, and confirmed in this work, the p-i-n structure based on the MAPI perovskite does not suffer from severe hysteresis issues [88]. The EQE spectra are also shown in Fig. 3.8. The integrated current density values, plotted on the same graph, match the J_{SC} obtained from the $J-V$ measurements, which for the devices based on TPA and MC-43 is 19.4 and 20.2 mA cm⁻² respectively, in excellent agreement with the value obtained from $J-V$. As it can be seen, the maximum EQE peaks of the top-performing devices can reach over 80% EQE, a notable photon-to-electron conversion for MAPI perovskite solar cells.

The highest FFs reported in the literature are usually due to the utilization of metal cathodes like aluminium or lithium fluoride/aluminium that present better energy alignment for electron extraction. However, despite the difference in energy levels between the LUMO of PC₆₀BM and the work function of Ag, we achieve for all devices very high FF values suggesting efficient charge transfer and extraction. The use of Ag as a top electrode is also preferable for its better stability in order to limit the device degradation and ensure a longer lifetime for the devices. In this context, the performance of the devices has been monitored in a short period, under continuous light illumination, and during several days by performing $J-V$ measurements to evaluate the durability of the devices. In Fig. 3.8 (bottom), we show the PCE stability under continuous 1 sun equivalent illumination measured by applying the voltage corresponding to the maximum power point, as obtained from the $J-V$ measurement, and registering the given current density. The devices show excellent stability with practically no degradation during the evaluation time.

The MC-43 based champion device has been also evaluated in the long-term period. The device was encapsulated and stored in dark under low humidity conditions. Fig. 3.11 is shown the $J-V$ curves for different time measurements. The photovoltaic parameters such as J_{SC} , V_{OC} , FF and PCE that obtain from Fig. 3.11 are also shown in Fig. 3.12. After encapsulation, the device still maintains 90% of its efficiency after 20 days.

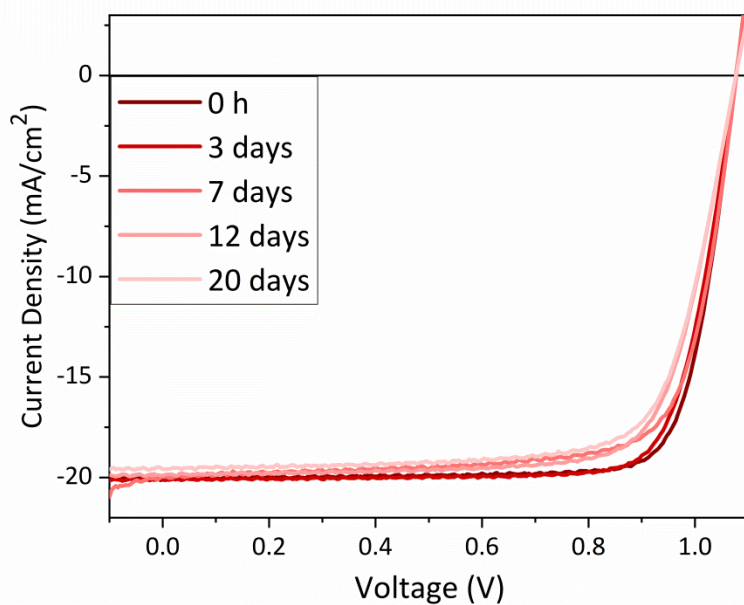


Figure 3.11: Evolution of the J - V characteristic, measured at 1 sun, for a MC-43 based PSC over 20 days. The device was encapsulated and stored in dark under low humidity conditions

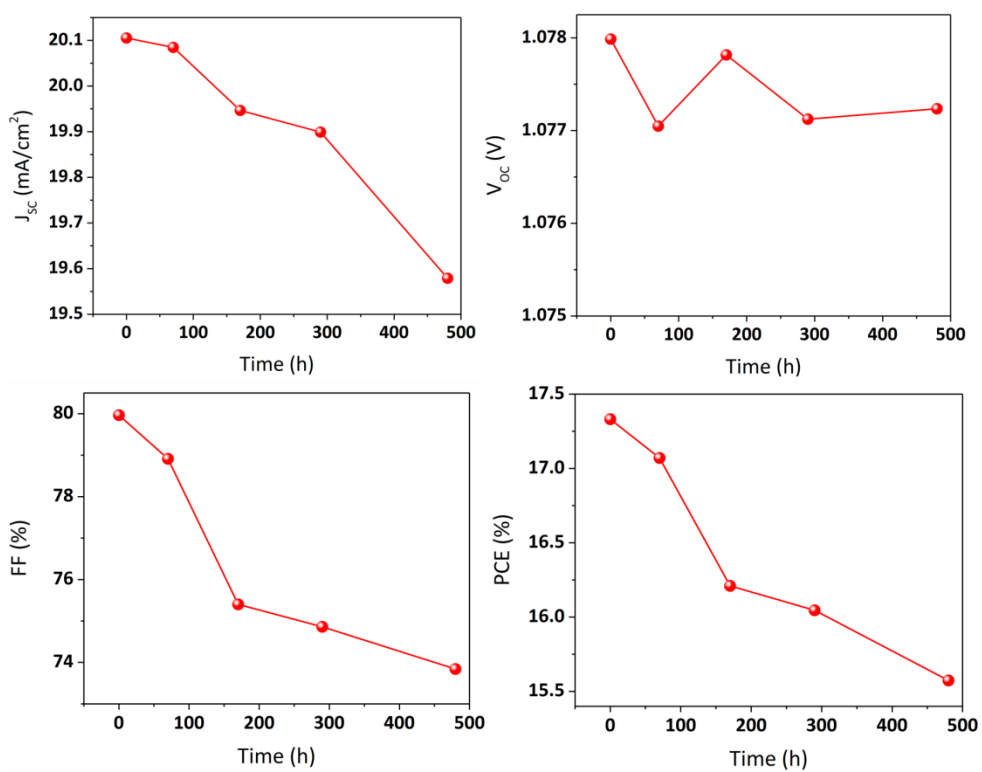


Figure 3.12: Long-term evolution of photovoltaic parameters of the best MC-43 based PSC measured at 1 sun

3.3.3 Conclusions

In summary, we have proposed two SAM organic molecules, TPA and MC-43, to be employed as WF modifiers and efficient substitutes for PEDOT:PSS on ITO electrodes. The solar cells fabricated with the planar p-i-n structure based on our SAMs show remarkable PCE, with the best cell based on TPA scoring 15.9% with a FF of 77%, V_{OC} of 1.06 V and J_{SC} of 19.4 mA cm^{-2} and the best performing MC-43 cell scoring 17.3% with a FF of 80%, V_{OC} of 1.07 V and J_{SC} of 20.3 mA cm^{-2} .

The use of SAMs ensures a homogeneous formation of the MAPI perovskite layer and gives rise to very high FF and V_{OC} . Although ITO/TPA has a 0.2 eV deeper HOMO than ITO/MC-43, the latter shows a slightly higher V_{OC} according to the statistics collected on several devices. An explanation for the best performance of MC-43 based devices is due to its better charge transfer capability (better energy alignment due to its redox properties as it is easier to oxidize) when compared to the TPA.

Also it is important to notice that the PCEs obtained with the surface modified MC-43 devices are among the highest values reported in the literature to date (23.06.2018). The extremely facile deposition method and the ability of these molecules to form strong covalent bonds with metal oxides and tune their WF, represent a clear benefit to reduce charge losses and ensure contact selectivity. As revealed by our work, these molecules can offer a valid alternative to conventional polymers with the aim of increasing the stability and durability of planar p-i-n PSCs.

Chapter 4

A Comparison of Monodentate and Bidentate Anchoring Group of Small Molecules as Hole Transport Layer for Perovskite Solar Cells

4.1 Introduction

Energy has become one of the main problems of humanity after the industrial revolution and the rise in world population. Most of the energy resources depend on fossil fuels which causes environmental problems. In order to solve these problems, intense research is carried out on renewable energy sources. The sun is the primary renewable energy source for the Earth. Converting efficient, cost-effective, and sustainable solar energy is a foremost challenge for this era. In recent years, researchers have been working on many types of solar cells for efficient photovoltaic energy conversion from the sun.

In a short time, the power conversion efficiency (PCE) of an organic-inorganic perovskite solar cells (PSCs) has increased from 3.8% to over 25% [8, 9]. The key to surpassing the efficiency of silicon-based solar cells in a short time is to understand perovskite material, which has high carrier mobilities, tunable bandgap, high absorption coefficient, long exciton charge diffusion length and long charge carrier lifetime [49, 89]. The configuration of PSCs can be divided into two main sandwich structures as regular (n-i-p) and inverted (p-i-n). For instance, in regular PSCs

configuration, n-type mesoscopic metal oxides, such as TiO₂, Al₂O₃ or ZrO₂ are utilized under the perovskite absorber layer due to their highly electron selective properties [90]. However, high processing temperatures (~450 °C) are required to calcinate these mesoscopic metal oxides, which significantly increases the production cost of these devices. Moreover, while this requirement makes it impossible to manufacture solar cells on flexible substrates, it is also a non-negligible obstacle for a large-scaled commercial device production method likewise a roll-to-roll process [91, 92]. Even though inverted PSCs have lower device performance than regular PSCs, they have a lower processing temperature (~100 °C) that allows them to be used on flexible and large-scaled substrates. Besides, inverted PSCs exhibit low hysteresis [81], and high long-term stability [93] since p-type charge selective contact does not need dopants that cause degradation [94].

Additionally, the interface between the perovskite layer and charge selective layers plays a critical role in achieving high PCE by reducing charge recombination losses and maximizing open circuit voltage (V_{OC}). Poly[bis(4-phenyl)(2,4,6-trimethylphenyl)amine] (PTAA) is one of the most widely used hole transport material in high efficiency inverted PSCs, despite its high-cost production and unstable polymer structure [95, 96]. To get rid of these obstacles to the commercialization of inverted PSCs, researchers have started to search for new materials likewise self-assembled molecules (SAMs). SAM molecules have previously used to modify transparent conductive oxide (TCO) in organic based optoelectronic devices. In 2018, SAMs had been first used as hole transport layer (HTL) in inverted PSCs [62, 97], and one of this first study is done by our group. Lastly, SAMs have been used intensively in perovskite solar cells after being commercially available on the market and led to over 22% in PCE [98-100]. As a larger variety of SAMs are needed due to these developments, we synthesized novel SAMs based bidentate anchoring groups that have not been used in PSCs until now.

In principle, SAMs are formed by 3 main moieties: a terminal moiety that controls the interfacial properties of thin films (1-3 nm), a spacer moiety that determines the packing geometry, and an anchoring moiety that forms chemical bond between small molecule and metal oxide. Each of the moieties plays a crucial role in obtaining a homogenous and stable thin film, and the selection of anchor groups takes

precedence in improving them. In 2013, Brennan et. al. performed systematically comparison between different anchor moieties to explore their effect on the device performance. Silatrane, phosphonic acid and carboxylic acid are preferred to functionalize a tetra-arylphorphyrin for attaching them onto metal oxide surface in dye-synthesized solar cells. They demonstrated that using carboxylic acid instead of phosphonic acid or silatrane as anchoring moiety almost doubled the short-circuit current, having better coverage metal oxide. As a consequence, improved light absorption boosted the PCE of the device [101].

The other main purpose of SAMs is tuning the work function of metal oxide surfaces to control the interface energy level alignment between different materials. On the contrary of PTAA, to produce SAMs are cheaper and reproducible owing to being small molecule. Additionally, their deposition technique onto metal oxide covered substrates can be alterable due to having low material consumption.

Herein, three novel SAM molecules with carboxylic acid anchoring groups are used as HTLs for inverted perovskite solar cells while PTAA used as baseline HTL for performance comparison. Two of SAM molecules have bidentate anchoring group (nominated MC-54 and MC-55) while one of them has monodentate anchoring group (nominated MC-45). Besides the PTAA comparison, we also have made a comparison between those two types of molecules (monodentate and bidentate group). In this paper, we studied surface engineering of the influence of SAM molecules on indium tin oxide (ITO) electrode, formation of perovskite and photovoltaic performance of PSCs. According to the results, high efficiency is obtained with SAM based two anchor groups without the need for any of inorganic or organic hole transport layers.

4.2 Result and Discussion

The chemical structures of the novel SAM and employed reference molecules are illustrated in Fig. 4.1a where 4'-(bis(4-methoxyphenyl)amino)-[1,1'-biphenyl]-4-carboxylic acid (**MC-45**), 4',4'''-([1,1'-biphenyl]-4,4'-diylbis(m-tolylazanediyl))bis((1,1'-biphenyl)-4-carboxylic acid) (**MC-54**) and 4',4'''-([1,1'-biphenyl]-4,4'-diylbis(naphthalen-1-ylazanediyl))bis((1,1'-biphenyl)-4-carboxylic acid) (**MC-55**). Fig. 4.1b-c shows the state-of-the-art device architecture employed

with SAMs or PTAA in inverted device configuration and cross-section field-emission scanning electron microscopy (FESEM) image of a completed device, respectively. The energy level alignment between the ITO/perovskite interfaces is a critical parameter for efficient charge injection from perovskite to the ITO electrode. So, work function (WF) of SAM modified ITO was found and shown in Figure 4.1d.

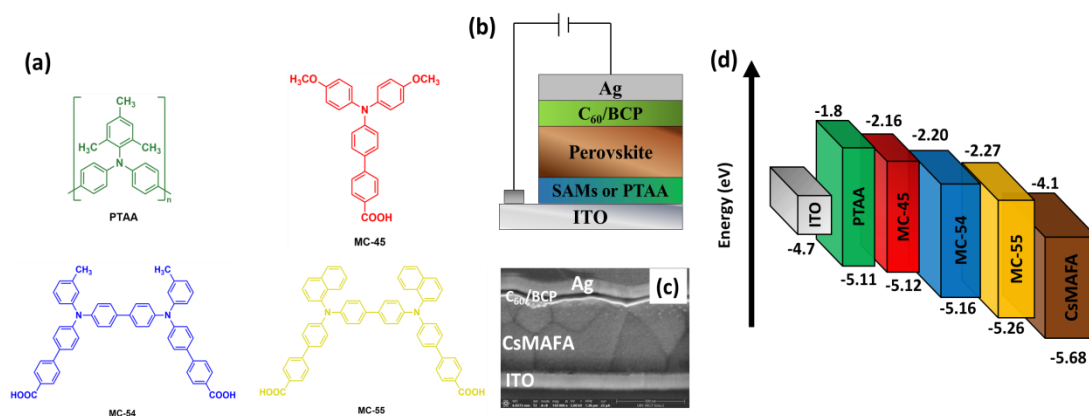


Figure 4.1: (a) Chemical structure polymeric PTAA and SAM molecules, (b) device structure of p-i-n (inverted) perovskite solar cell, (c) cross section FESEM images of a complete device, (d) work function of bare ITO, SAM modified ITOs, PTAA and CsMAFA perovskite

Before starting to fabrication of devices, thermal (TGA, DSC) and electrochemical (CV, UV-vis) behaviors of SAM molecules were recorded. After that, ITO surface modified by SAM molecules was characterized by XPS, AFM and contact angle measurements. Additionally, the surface morphology of perovskite film and perovskite crystallinity was measured by FESEM and XRD, respectively. Finally, photovoltaic measurement of devices was conducted. Each part of characterization was detailed as in the following sections.

4.2.1 Thermogravimetric (TGA) and Differential Scanning Calorimetry (DSC) Measurement of SAM molecules

The thermal behavior of MC-45, MC-54 and MC-55 was measured by TGA (Figure 4.2) and DSC (Figure 4.3). The result of TGA investigation, confirmed high thermal stability with decomposition temperatures (T_{des}), determined 5% weight loss for MC-45, MC-54, and MC-55 of 313, 242, and 295 °C, respectively.

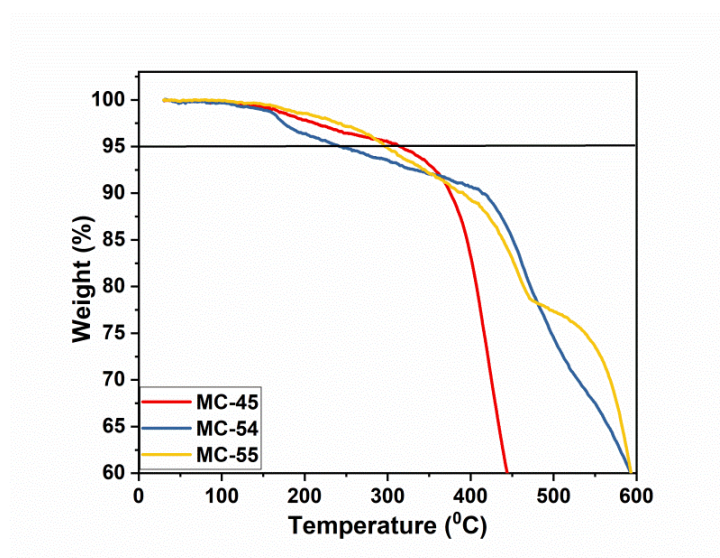


Figure 4.2: TGA analyses of MC-45, MC-54 and MC-55 at scan rate of 10°C/min under N₂ atmosphere

In addition, DSC measurement was carried out to determine glass transition temperatures (T_g) of SAM molecules. Their T_g temperatures were determined from second heating cycle as 180, 184, and 182 °C, respectively. Thermal behavior results confirm that these SAM molecules can resist the annealing process temperature of perovskite (100 °C).

T_{des} and T_g values of SAM from TGA and DSC are listed in table 4.1.

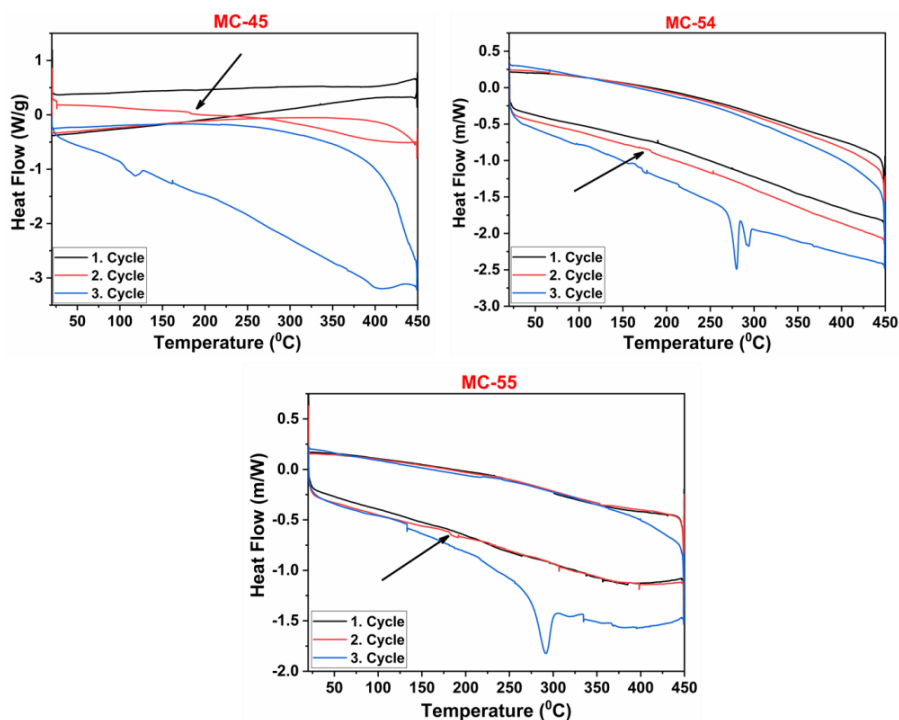


Figure 4.3: DSC analyses of MC-45, MC-54 and MC-55 at scan rate of 10 °C/min under N₂ atmosphere

Table 4.1: Thermal properties of SAM molecules

	MC-45	MC-54	MC-55
T _{des} (°C)	313	242	295
T _g (°C)	180	184	182

4.2.2 Optical and Electrochemical Characterization of Molecules

To determine the effect of SAM molecules on the WF of ITO, cyclic voltammetry investigation was performed by using a three-electrode system in solution and on modified ITO surface. The results are illustrated schematically in Figure 4.4. The highest occupied molecular orbital (HOMO) levels of molecules are determined from the inflection point of CV with the solution process (Fig. 4.4a) and calculated from equation 4.1. The HOMO level of MC-45, MC-54 and MC-55 are calculated as -5.17, -5.22 and -5.30 eV, respectively. Similarly, the new work function of ITO, after modification with SAM molecules (ITO/MC-45, ITO/MC-54, and ITO/MC-55)

was found as -5.12 , -5.16 and -5.26 eV from the inflection point of CV (Fig. 4.4b) and calculated with equation 4.1. Additionally, the lowest unoccupied molecular orbital (LUMO) levels and optical bandgap of SAMs are calculated from the absorption edge wavelength of UV-Vis spectra (Fig. 4.4c).

The optical and electrochemical values of SAM molecules are listed in table 4.2.

$$E_{\text{HOMO}} = -(E_{1/2(\text{ox})} + 4.4) \text{ eV} \quad (4.1)$$

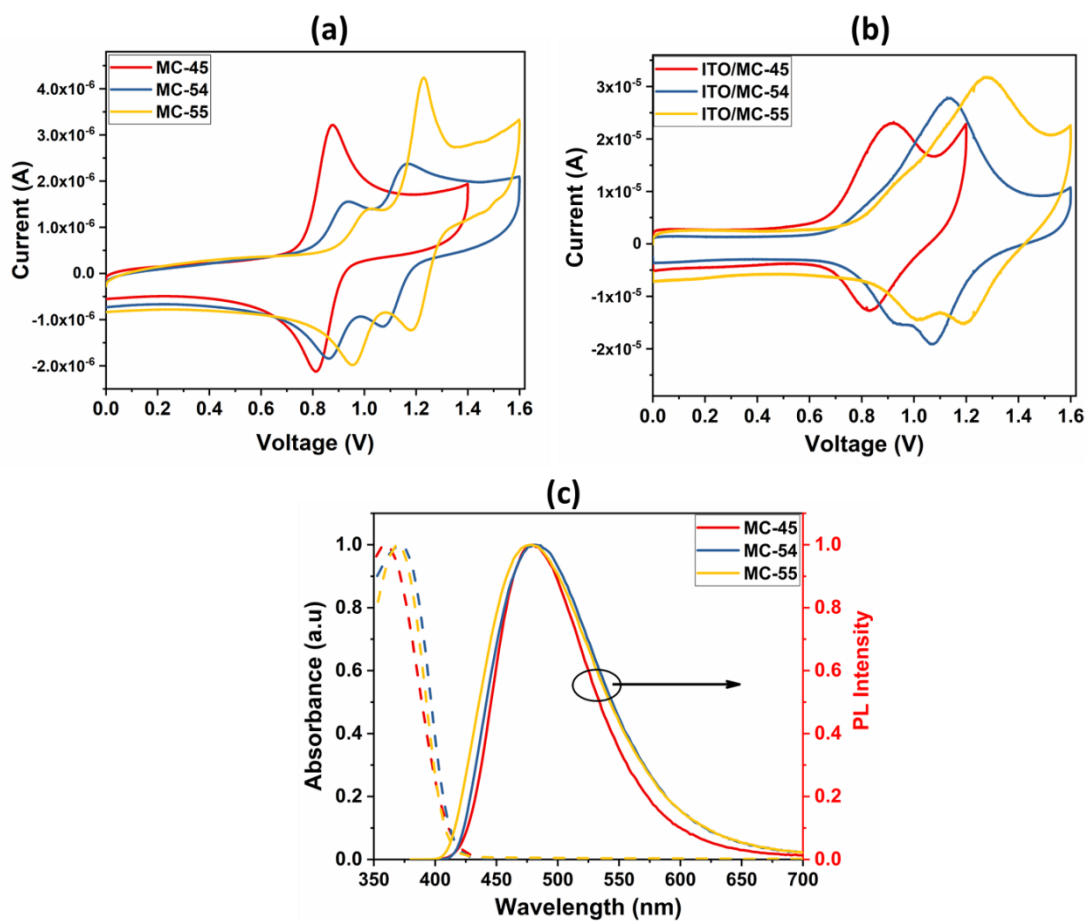


Figure 4.4: CV voltammogram of SAM molecules in solution (a) and ITO/SAM coating (b). UV (dashed lines) and PL Intensity (solid lines) of MC-45, MC-54 and MC-55 (c)

Table 4.2: HOMO, LUMO and bandgap values of SAM molecules

	MC-45	MC-54	MC-55
HOMO (eV)	-5.17	-5.22	-5.30
LUMO (eV)	-2.16	-2.20	-2.27
WF of SAM modified ITO (eV)	5.1	5.16	5.26
E_g^{opt.} (eV)	3.01	3.02	3.03

4.2.3 Effects of SAM Molecules on ITO surface and Perovskite properties.

For further exploration of surface modification of ITO, the atomic bonds of SAMs on the ITO surfaces were examined using X-ray photoelectron spectroscopy (XPS). Figure 4.5 shows the high-resolution survey spectrum of C1s and O1s for ITO/MC-45, ITO/MC-54, ITO/MC-55 and bare ITO. The C1s spectra are fitted by three peaks corresponding to carbon in the different chemical environments. The binding energy peaks of C1s (Fig. 4.5 left) for ITO/MC-45 at 284.3, 285.2 and 287.7 eV, for ITO/MC-54 at 284.0, 284.9 and 288.2 eV and for ITO/MC-55 at 284.4, 285.1 and 288.7 eV are assigned to C–C or C–H, C–O–C and O–C=O, respectively. The peaks at 287.7, 288.2 and 288.7 eV are attributed to O–C=O (ester bonding) and indicate the formation of covalent bonds between –COOH (carboxylic acid) anchoring moieties of MC-45 (Fig.4.5a), MC-54 (Fig.4.5b) and MC-55 (Fig.4.5c) molecules and –OH (hydroxyl moieties) existent on the ITO surface [62, 98].

The O1s high-resolution survey spectra (Fig.4.5 right) show three main components for all SAMs. The O1s of ITO/MC-45 peaks observed at 530.0, 531.2, and 533.6 eV correspond to lattice oxide in $\text{In}_x\text{Sn}_y\text{O}_z$ and carbonyl group (C=O), respectively. Approximately the same peaks are obtained from ITO/MC-54 and ITO/MC-55 coated surfaces.

All corresponding bonding energy of functional groups was given in Table 4.3.

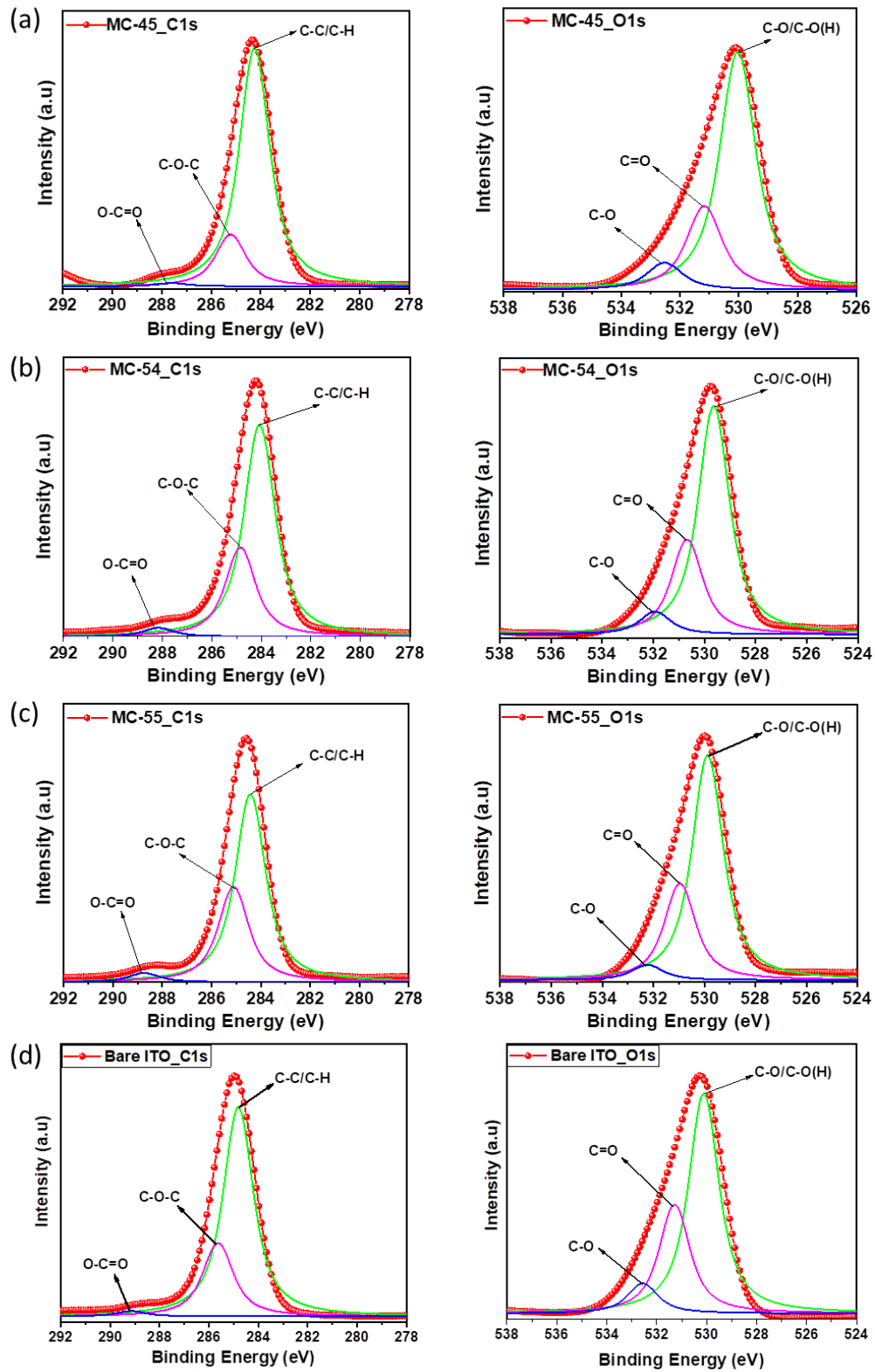


Figure 4.5: XPS high-resolution surface spectra of C1s and O1s for ITO/MC-45 (a), ITO/MC-54 (b), ITO/MC-55 (c) and bare ITO (d)

Table 4.3: The corresponding bonding energy of functional groups of ITO/MC-45, ITO/MC-54, ITO/MC-55 and bare ITO

Samples	C1s (eV)			O1s (eV)			N1s
	<i>C-C/C-H</i>	<i>C-O-C</i>	<i>O-C-O</i>	<i>C-O/C-O(H)</i>	<i>C=O</i>	<i>C-O</i>	
MC-45	284.3	285.2	287.7	530.0	531.2	532.6	400.0
MC-54	284.0	284.9	288.2	529.6	530.6	532	399.4
MC-55	284.4	285.1	288.7	529.9	530.9	532.3	399.6
Bare ITO	284.8	285.6	289.2	530.1	531.3	532.6	—

The high-resolution survey spectrum of C1s and O1s for bare ITO is shown in Figure 4.5d. As in ITO/MC-45, ITO/MC-54, and ITO/MC-55, the same functional groups and almost the same peaks are obtained from C1s and O1s high-resolution survey spectrum of bare ITO.

Figure 4.6 shows high-resolution surface spectra of N1s for ITO/MC-45, ITO/MC-54, ITO/MC-55 and bare ITO. The binding energy peak of N1s for ITO/SAM molecules is around 400 eV. Bare ITO does not have any peak around 400 eV because it does not contain ‘N’ element. The absence of ‘N’ peak on bare ITO whereas its presence on SAM modified ITO surface confirms that SAM molecules successfully covered the ITO substrates.

In addition to the XPS high-resolution surface spectra, surface spectra of the ITO/MC-45, ITO/MC-54, and ITO/MC-55 are given in Fig. A.4, Fig. A.5 and Fig. A.6, respectively.

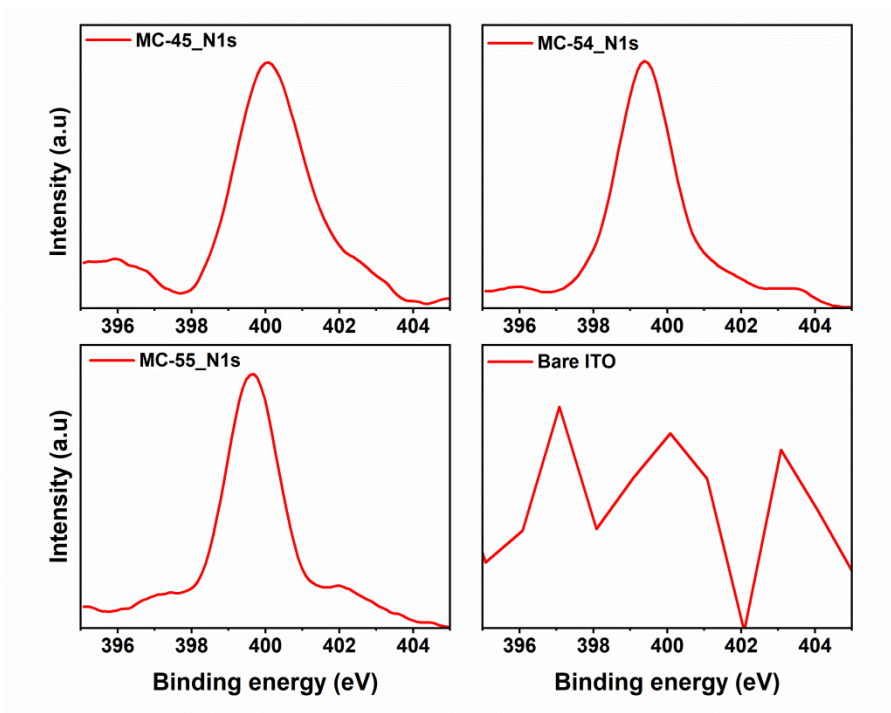


Figure 4.6: High resolution surface spectra of N1s for ITO/MC-45, ITO/MC-54 and ITO/MC-55

Surface topography and root mean square (RMS) of bare ITO, ITO/PTAA and SAM modified ITOs are determined by Atomic Force Microscopy (AFM) from different scan scales. Surface topography images and RMS roughness values are given in Figure 4.7 and Figure 4.8, respectively. According to roughness values, the ITO morphology becomes smoother after modification (Fig. 4.8). This result shows that SAM molecules do not have adverse effects on surface morphology and ITO permeability.

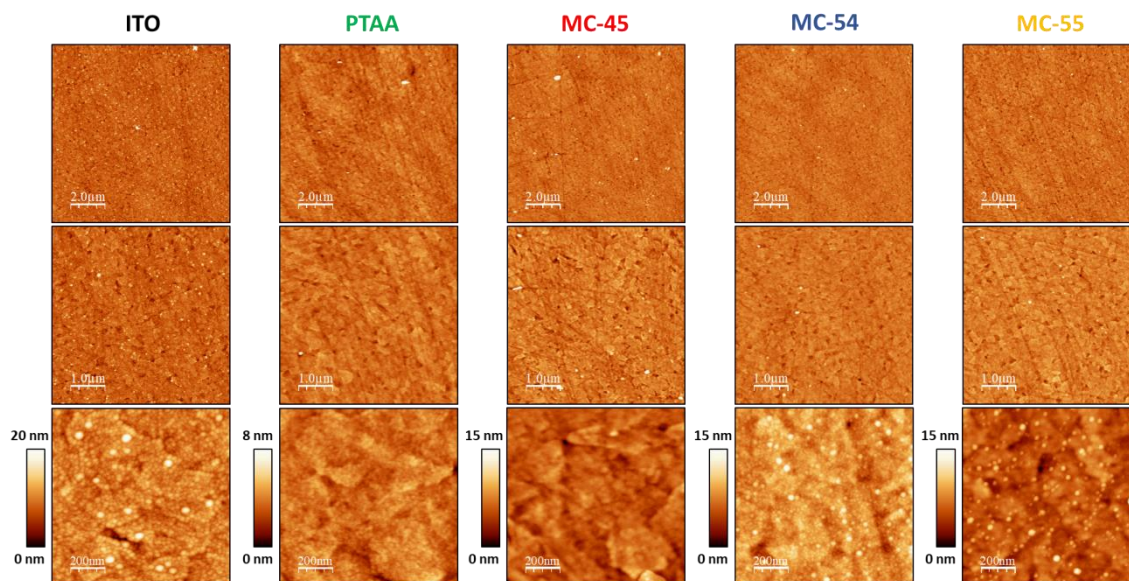


Figure 4.7: Surface topography of bare ITO, ITO/PTAA, ITO/MC-45, ITO/MC-54 and ITO/MC-55 from different scan scales

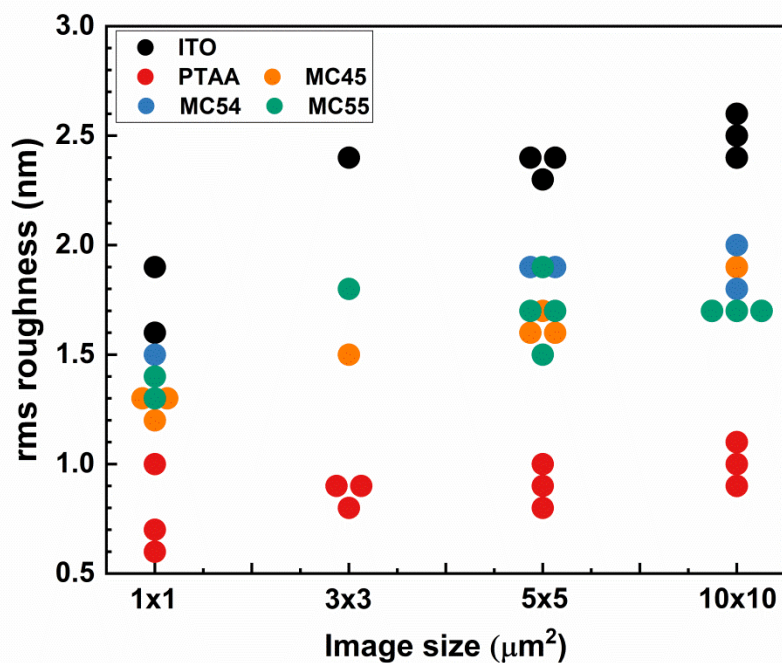


Figure 4.8: RMS values of bare ITO and modified ITO from different scan scales

Area images of surface potential differences are beneficial to understanding whether ITO is covered homogeneously with SAM molecules or not. Figure 4.9 shows the high resolution of surface topography of ITO/SAM molecules and surface potential

mapping of ITO/SAMs measured using KPFM. According to the previous report [102-104], the surface potential of ITO is increased after being treated with SAMs. As can be seen from surface potential images (Fig 4.9), it can be said that SAMs are homogeneously deposited on the ITO surface using the dip-coating method.

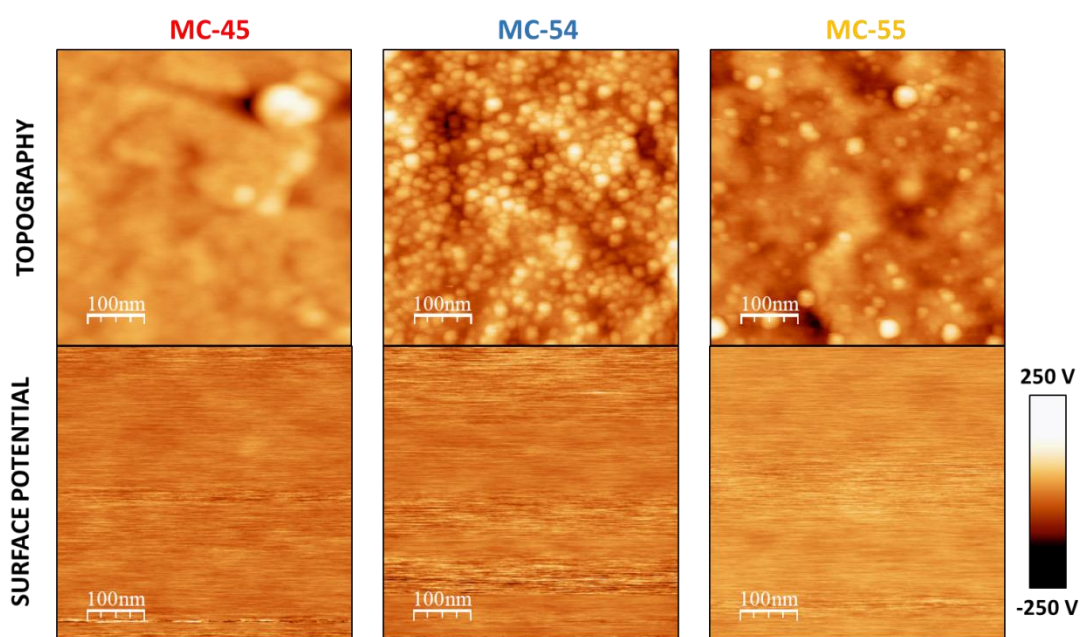


Figure 4.9: Surface topography and surface potential mapping of ITO/SAM from KPFM

The surface wettability of ITO substrates is investigated before and after modification with SAMs by contact angle measurement in a sessile water drop experiment. As it is well known, bare ITO has a hydrophilic character because hydroxyl and carboxyl groups consist on its surface [105-107]. Thus, the unmodified ITO surface shows a high wettability according to water. Although wettability allows us to obtain a homogeneous perovskite film on top of it, it has been reported that water and moisture harm perovskite device performance and stability [108-110]. The interface between perovskite and functional layers is important saving perovskite layer from environmental effects. Figure 4.10 shows water contact angles of bare ITO, ITO/MC-45, ITO/MC-54 and ITO/MC-55 as 54° , 85° , 87° and 88° respectively. The results show that hydrophobic characters of SAM molecules are in favor of blocking moisture into devices [111]. SAM formation provides a non-wetting surface

and reduces the dragging force between the perovskite layer and ITO/SAM surface. It contributes to the formation of large grains [49, 112].

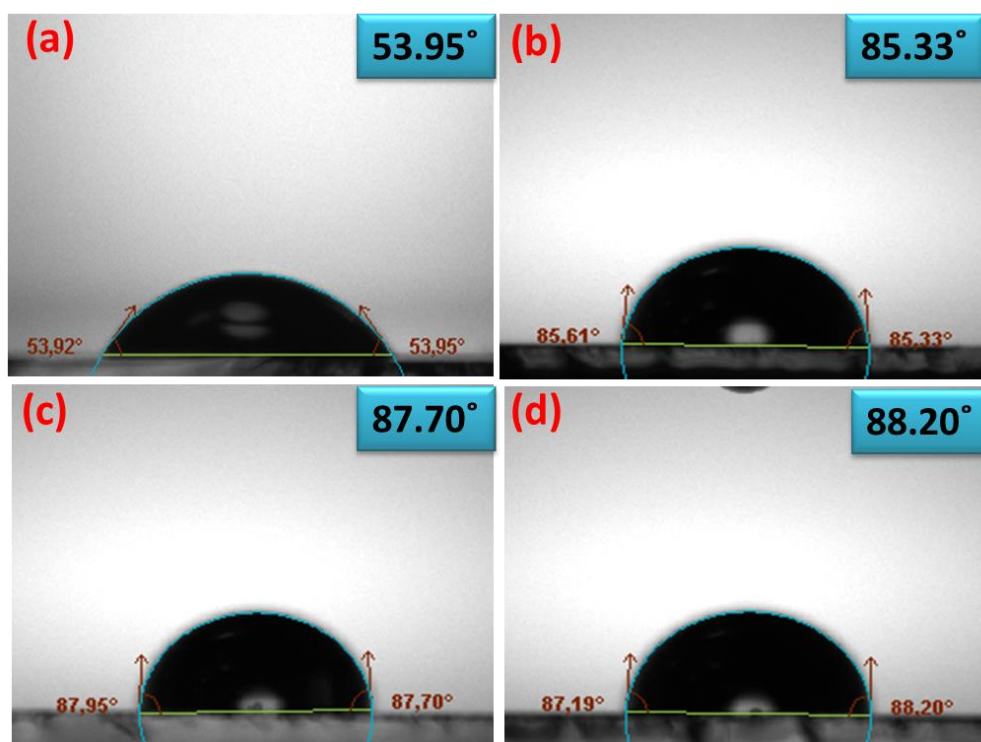


Figure 4.10: Contact angle of (a) bare ITO, (b) ITO/MC-45, (c) ITO/MC-54 and (d) ITO/MC-55

After confirming the existence of SAM molecules on ITO substrates, perovskite is deposited on ITO/SAMs surfaces and PTAA thin film (~10 nm). After that, FESEM and XRD analyses are performed on perovskite films to verify the effect of SAM molecules on perovskite grain size and perovskite crystallinity. Perovskite film quality has a significant effect on the performance of PSCs. The quality of the film is determined by grain size, good crystallinity, pin hole-free with whole surface coverage. Various methods have been used to improve PSCs film quality such as controlling crystal growth, solvent engineering [74, 113], layer by layer vapor deposition [114], fast deposition-crystallization [115], so on [76, 116]. However, according to some studies, grain boundaries are a major recombination center in iodide-based perovskite and that is degrading cell performance [21, 113, 117, 118]. To overcome this problem, the number of grain boundaries should be reduced and

increased grain size is one of the most effective ways to reduce it. Figure 4.11 shows the top view of FESEM images and grain size distributions of perovskite films on bare ITO, PTAA, MC-45, MC-54 and MC-55.

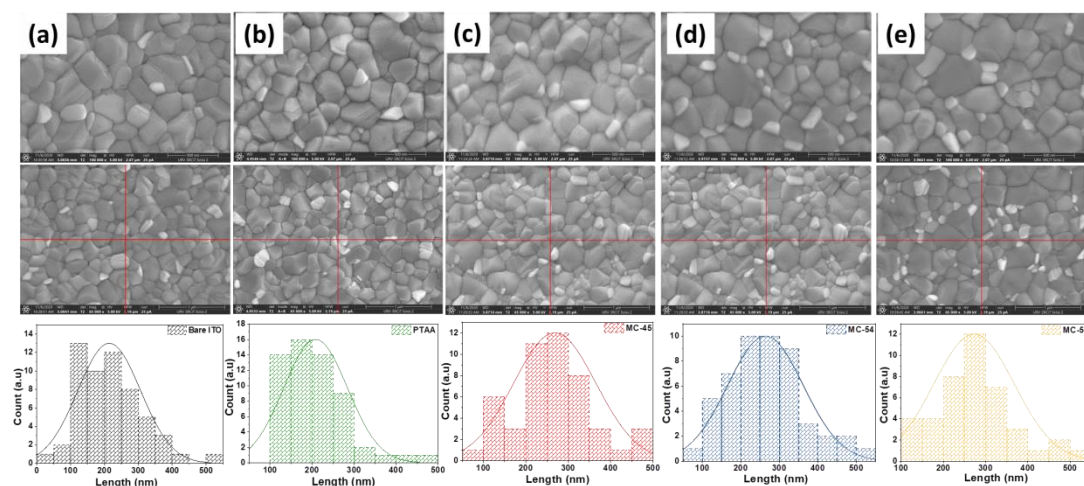


Figure 4.11: FESEM images (up and middle) and grain size distribution (down) of perovskite films before and after modification of ITO. Perovskite was deposited on a) bare ITO, b) ITO/PTAA, c) ITO/MC-45, d) ITO/MC-54 and e) ITO/MC-55

The first line images of SEM show high resolution of perovskite films (mag 100000 X) and second-line images are selected with large scale area (mag 65000 X) to detect more grains for determining grain boundary distributions with better accuracy. A horizontal and vertical red line separated these images in the middle and gain size distributions are found by calculating the size of all grains on these lines. According to the results, mean values of grain size of perovskite films are significantly increased after modifications of SAM molecules (Table 4.4) that reduce the grain boundaries and decrease the density of charge traps and electron-hole recombination [117, 119], increasing the carrier transport and charge collection efficiency [113, 120-122].

Table 4.4: Grain size distribution results of perovskite films surface

Samples	Number of Grains	Mean (nm)	Minimum (nm)	Maximum (nm)
Bare ITO	56	213.92	44.55	523.34
PTAA	58	208.32	102.45	485.45
MC-45	48	268.23	90.42	491.70
MC-54	50	264.02	85.33	515.35
MC-55	42	272.63	113.14	542.06

In addition to the perovskite films images, the whole device's cross-section is imagined by FESEM (Figure 4.12). According to the images, all layers of the devices are successfully coated.

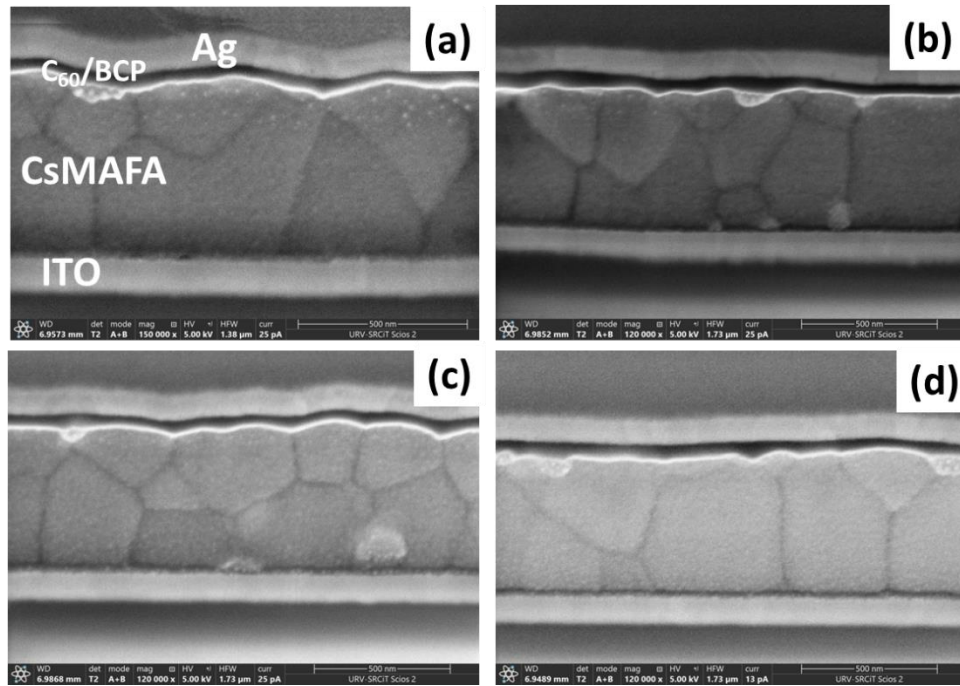


Figure 4.12: SEM cross-section of full devices: (a) ITO/PTAA, (b) ITO/MC-45, (c) ITO/MC-54, and (d) ITO/MC-55

XRD is used to characterize the crystal structure of CsMAFA perovskite (Figure 4.13). The diffraction peaks of XRD at 14.10° , 19.93° , 24.43° , 28.30° , 31.80° , 34.90° , 40.54° and 43.00° correspond to (100), (110), (111), (200), (210), (211), (220) and

(300) planes to a tetragonal phase of CsMAFA perovskite, respectively. The diffraction peak at 12.65° belongs to residual PbI_2 . Moreover, excess PbI_2 can passivate defects, increase V_{OC} [123, 124], and short-circuit current (J_{SC}) [125], improving device stability, and significantly, protecting against water or oxygen-induced degradation [126, 127].

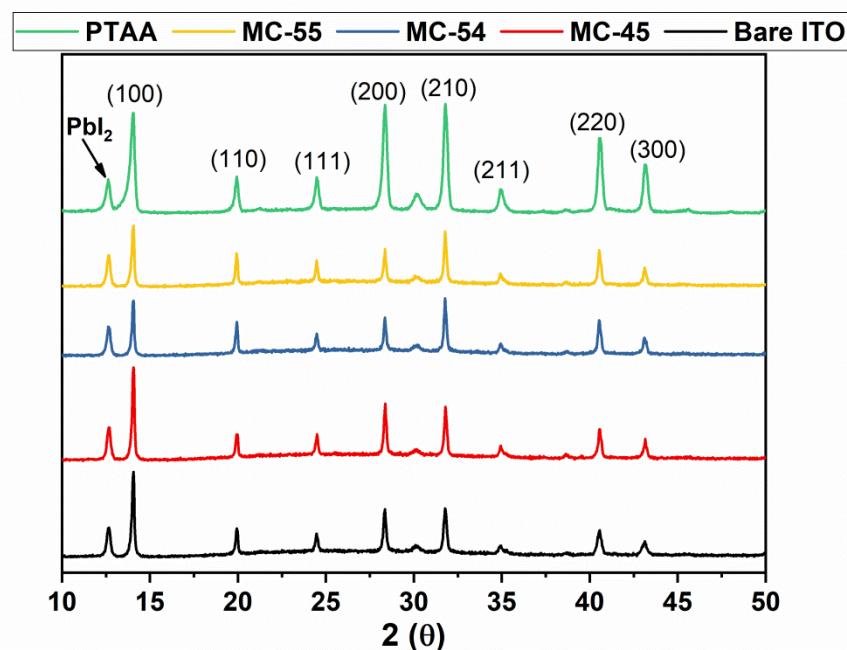


Figure 4.13: XRD patterns of bare ITO, ITO/PTAA, ITO, MC-45, ITO/MC-54 and ITO/MC-55

To investigate the effect of these novel SAMs on hole transport properties and carrier recombination at the interface between perovskite and selective contact, steady-state photoluminescence (PL) spectra and time-resolved PL (TrPL) of ITO/CsMAFA, ITO/PTAA/CsMAFA, and ITO/SAMs/CsMAFA films are performed (Figure 4.14). CsMAFA perovskite film deposited on bare ITO, PTAA, and SAMs modified ITOs to compare PL intensities. Then, poly[methyl methacrylate] films are deposited on perovskite layers to protect them from the environment. As shown in Figure 4.14a, PL intensities of devices containing SAMs and PTAA are significantly lower than the PL intensity of ITO/CsMAFA film. It indicates that SAM molecules facilitate the hole transfer from the perovskite layer to ITO, improving hole extraction and

suppressing carrier recombination [128]. Furthermore, TrPL measurement is performed to analyze carrier lifetime at the interface of perovskite and HTLs. TrPL decay measurement was shown as in Figure 4.14b. As previously reported [98, 129, 130], TrPL was fitted to a bi-exponential decay function. The carrier lifetimes, τ_1 (τ_2), of ITO/CsMAFA, ITO/PTAA/CsMAFA, ITO/MC-45/CsMAFA, ITO/MC-54/CsMAFA and ITO/MC-55/CsMAFA are 29.4 (110.2), 10.6 (48.4), 15.4 (75.6), 15.8 (66.9) and 21.2 (78.3) ns, respectively (Table 4.5). TrPL results further prove that hole extraction from the perovskite layer to the ITO is improved after modification with SAM molecules.

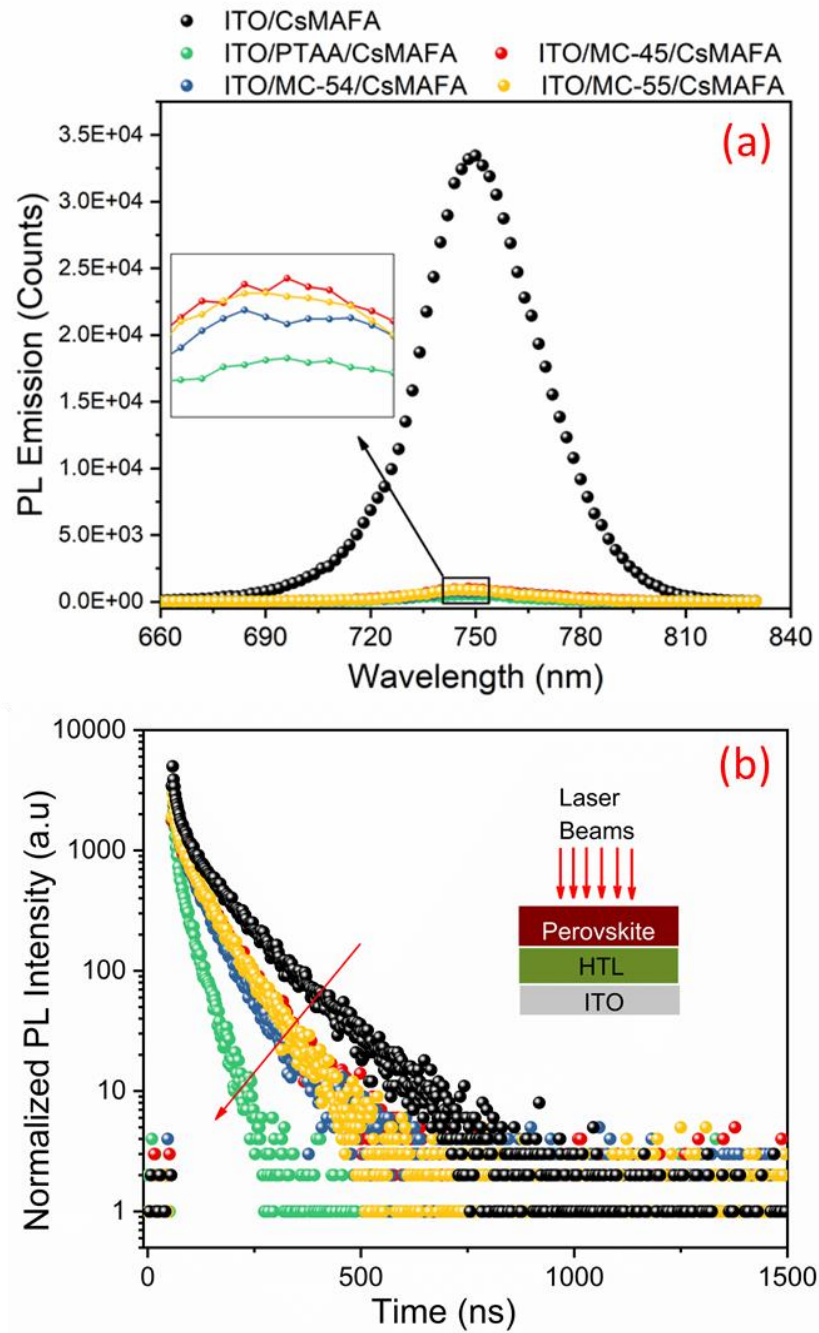


Figure 4.14: (a) Steady-state PL and (b) TrPL spectra of CsMAFA perovskite film on bare ITO, PTAA, MC-45, MC-54 and MC-55

Table 4.5: Carrier lifetime at the interface of ITO/CsMAFA, ITO/PTAA/CsMAFA, ITO/MC-45/CsMAFA, ITO/MC-54/CsMAFA and ITO/MC-55/CsMAFA that obtained from TrPL

Films	τ_1 (ns)	τ_2 (ns)
ITO/CsMAFA/PMAA	29.4	110.2
ITO/PTAA/CsMAFA/PMMA	10.6	48.4
ITO/MC-45/CsMAFA/PMMA	15.4	75.6
ITO/MC-54/CsMAFA/PMAA	15.8	66.9
ITO/MC-55/CsMAFA/PMMA	21.2	78.3

4.2.4 Photovoltaic Performance

Figure 4.1b illustrates the device structure of the inverted PSC (ITO/SAM or PTAA/CsMAFA/C₆₀/BCP/Ag). In this study, triple cation perovskite (CsMAFA) was deposited on HTLs (SAMs and PTAA) by spin coating, then C₆₀ and bathocuproine (BCP) layers were evaporated thermally on the perovskite layer. Lastly, the silver (Ag) electrode is thermally evaporated to complete device structure. All fabrication method is explained in detail in the experimental section of Chapter 2.

PTAA is commonly used in recently published high PCE p-i-n PSCs as a polymeric HTL due to performing high efficiency. In this study, as mentioned before, three novel SAM molecules (MC-45, MC-54 and MC-55) are used as HTLs while PTAA is used as baseline HTL for performance comparison of cells with SAMs.

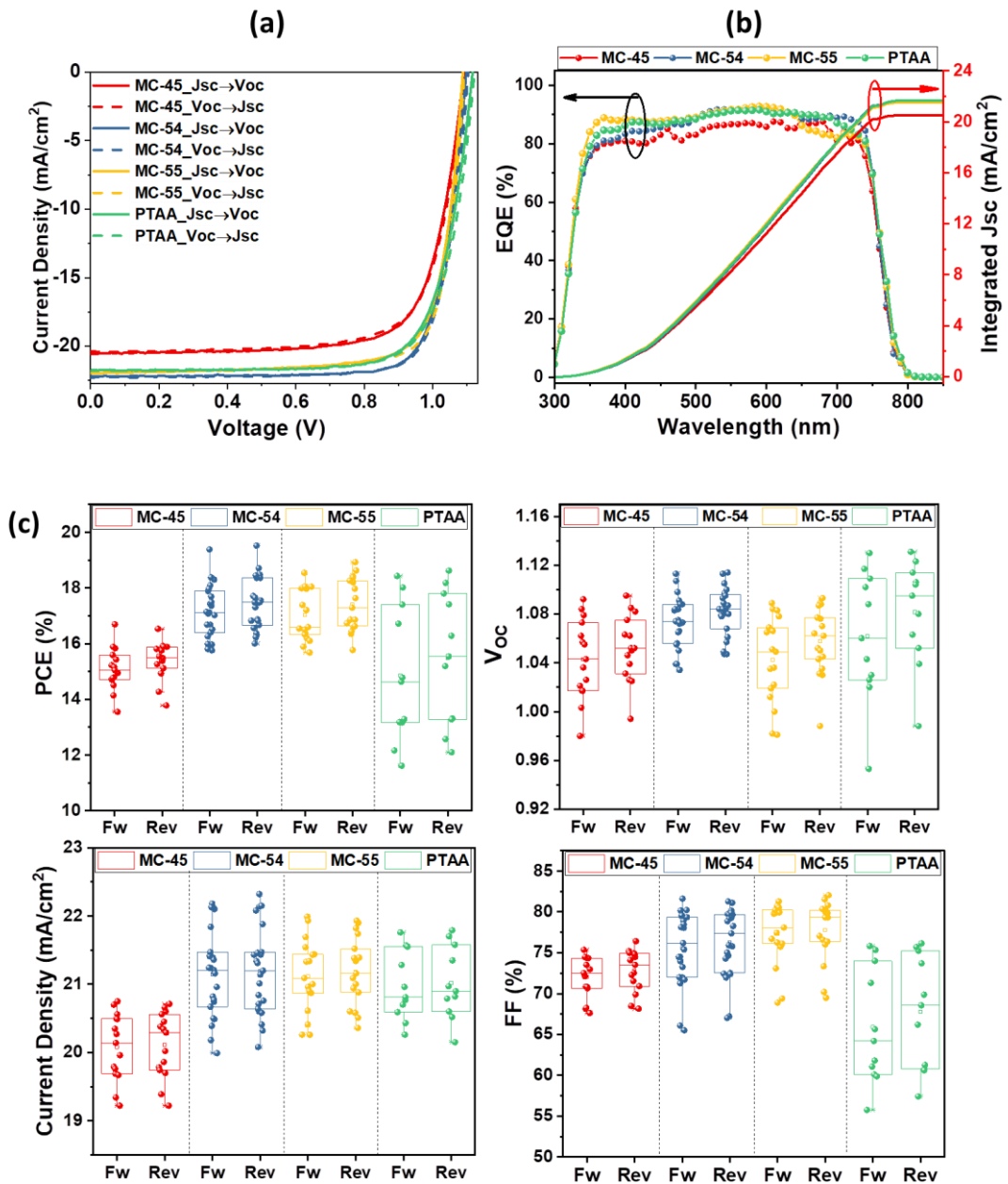


Figure 4.15: (a) $J-V$ curves of best solar cells in forward (J_{SC} to V_{OC} , solid line) and reverse scan (V_{OC} to J_{SC} , dashed line). (b) External quantum efficiency (EQE) spectra which show integrated current density of best solar cells. (c) Statistic values of photovoltaic parameters with PTAA, MC-45, MC-54 and MC-55 HTL for both forward (fwd) and reverse (rev) scan direction

Figure 4.15a shows the current density *versus* voltage ($J-V$) curves of the best devices of PTAA, MC-45, MC-54 and MC-55 under one sun illumination (AM 1.5G, $100\text{mW}/\text{cm}^2$). $J-V$ characteristic scan was performed in forward (J_{SC} to V_{OC} , solid

lines) and reverse (V_{OC} to J_{SC} , dashed lines) at a scan rate of 40 mW/s. As can be understood from J - V curves, all cells present negligible hysteresis. Figure 4.15b shows the external quantum efficiency (EQE) of champion devices with integrated J_{SC} . The maximum EQE peaks of the best-performing devices are around 90% EQE, indicating a significant photon to electron conversion and less recombination [100].

There is a minor difference between J_{SC} values obtained from J - V curves and integrated J_{SC} obtained from EQE. All photovoltaic parameters and hysteresis index (HI) of the best devices are summarized in Table 4.6. A statistic distribution of photovoltaic performances of J_{SC} , V_{OC} , fill factor (FF) and PCE is shown in Figure 4.15c.

According to the results, SAM-based bidentate anchor groups (MC-54 and MC-55) have higher PCE than MC-45 and PTAA. The best PCEs of MC-54 and MC-55 are 19.52% and 18.99% surpassing the best value of MC-45 (16.69%) and PTAA (18.62%). Especially, MC-54 and MC-55 have better J_{SC} according to MC-45 which has monodentate anchor group. It can be said that MC-54 and MC-55 have a better hole injection from perovskite to ITO electrode according to MC-45. In addition, SAMs' statistical values of photovoltaic parameters (Figure 4.15c) exhibit higher reproducibility than PTAA.

Table 4.6: Photovoltaic parameters of best performing devices

Samples	Scan	J_{sc} (mA/cm²)	J_{sc_EQE} (mA/cm²)	V_{oc} (V)	FF (%)	PCE (%)	HI (%)	V_{bi} (V)
PTAA	Forward	21.76	21.69	1.117	75.82	18.43	0.010	1.10
	Reverse	21.79		1.123	76.14	18.62		
MC-45	Forward	20.56	20.55	1.092	74.35	16.69	-0.010	1.082
	Reverse	20.38		1.095	74.08	16.53		
MC-54	Forward	22.18	21.59	1.098	79.57	19.38	0.007	1.092
	Reverse	22.32		1.105	79.15	19.52		
MC-55	Forward	21.99	21.53	1.089	77.45	18.54	0.023	1.089
	Reverse	21.90		1.093	79.32	18.99		

Built-in Potential (V_{bi}) has a significant effect on solar cell parameters. It is determined by extrapolating the linear part of J - V curves at $J = 0$ under dark conditions. V_{bi} values of PTAA polymer and SAM molecules were found from dark J - V curves (Figure 4.16) and listed in Table 4.6. A maximum achievable V_{OC} is limited by V_{bi} [131]. As depicted in Table 4.6, MC-45 has a lower V_{OC} according to MC-54 and MC-55. With a large V_{OC} , the driving force of charge separation is expected to be larger [132]. Therefore, the current density of devices is supposed to be higher with a large V_{bi} . Depending on these results, MC-54 and MC-55 modifications show higher current density than MC-45 modification. A larger built-in potential will not only increase the driving force of charge separation but also extended the depletion region for efficiently suppressing recombination [133]. Which is supports steady-state PL and TrPL measurements.

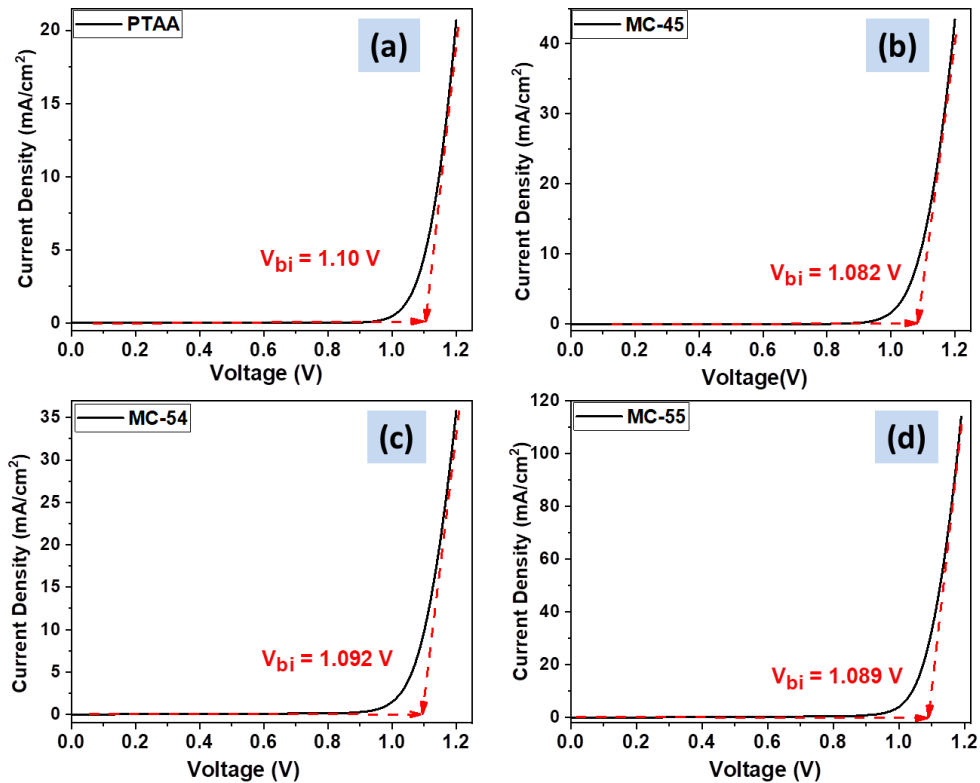


Figure 4.16: Built-in potential is estimated from dark J - V curves of PTAA (a), MC-45 (b), MC-54 (c) and MC-55 (d)

Analysis of J - V characteristics as a function of light intensity is a common approach to define the recombination mechanism [134]. Figure 4.17 shows J - V curves of PSCs with PTAA, MC-45, MC-54 and MC-55 hole transport materials respect to light intensity. For this measurement, different optical filter were used to obtain different light intensity. Under low level light intensity, Shockley-Read-Hall (monomolecular) process is dominating charge carrier recombination by trap sites such as substitutions or interstitials and vacancies [65, 135]. However, with increasing charge carrier density, radiative (bimolecular) recombination between unbound electrons and holes take over [136].

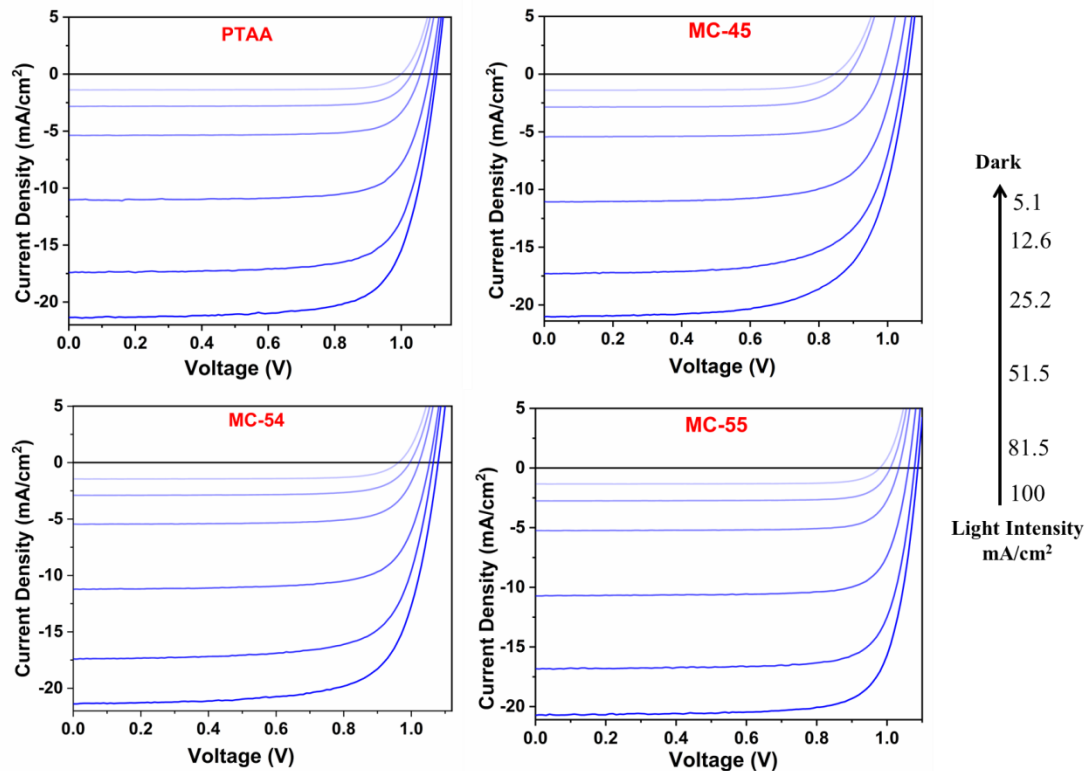


Figure 4.17: J - V curves of PTAA, MC-45, MC-54 and MC-55 based devices at different light intensity

From J - V curves of figure 4.17, V_{OC} and J_{SC} values from each light intensity are extracted and plotted as J_{SC} and V_{OC} versus different light intensity (Figure 4.18). The variation of J_{SC} and light intensity is fitted by power law function (equation 2.4, Chapter 2) where α represent the radiative recombination degree. If $\alpha = 1$, there is no photocurrent losses at the J_{SC} conditions. According to results (Fig. 4.18a), $\alpha = 0.98$,

0.96, 0.97 and 0.98 for PTAA, MC-45, MC-54 and MC-55, respectively. α value for all the samples is close to 1 and it indicates that biomolecular recombination is negligible under short-circuit conditions [137].

In addition, it is possible to calculate ideality factor (n_{id}) from V_{OC} dependence the light intensity. The n_{id} of a diode is a measure of how much solar cell closely ideal diode behaviour. The n_{id} is converted from slope of the logarithmic V_{OC} vs light intensity (Fig. 4.18b) by equation 2.6 (Chapter 2). Typically, the n_{id} is between 1 and 2 ($1 < n_{id} < 2$). If the n_{id} close to 1 biomolecular recombination dominates, if n_{id} higher than 1 and approach to 2, monomolecular recombination dominates mechanism [138, 139].

The n_{id} values are obtained as 1.43, 1.60, 1.48 and 1.56 for PTAA, MC-45, MC-54 and MC-55, respectively. It is indicating that all devices has acceptable ideality factor.

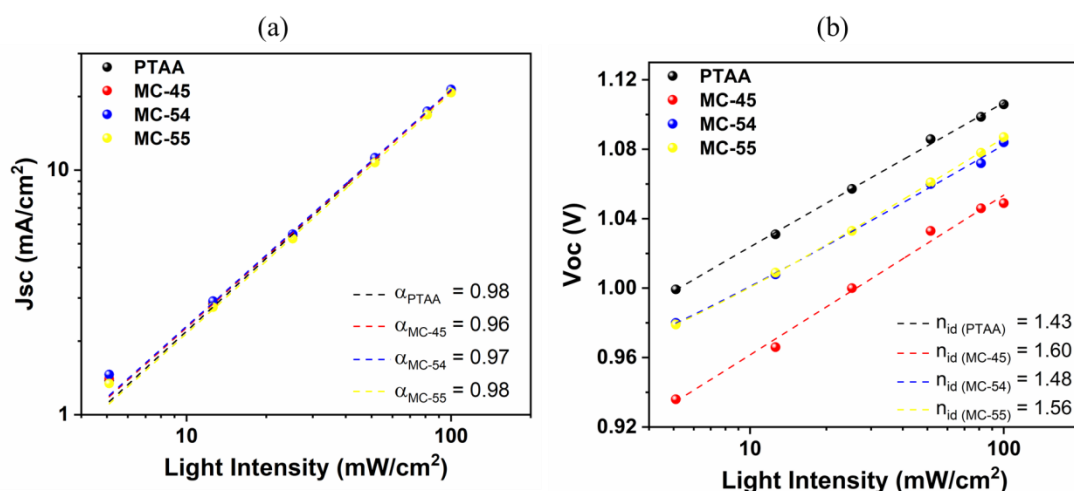


Figure 4.18: (a) J_{SC} and (b) V_{OC} dependence of light intensity for different HTM

We have investigated the stability of the completed PSCs based on SAMs and PTAA in the ultrahigh vacuum compatible sample holder at 45 °C. The PCE of PTAA based PSC rapidly decays and eventually collapses after 10 h, whereas the MC-45 based PSC retains 80% of its initial efficiency after that time. This result shows that MC-45 has better durability than PTAA even if it has lower device performance due to its

molecule structure. As can be seen in Figure 4.2, MC-45 has a higher decomposition temperature (300 °C, 5% weight loss) compared to PTAA (~120 °C, 5% weight loss) [140]. As demonstrated in a previous study, PTAA exhibits faster decay due to breaking the carbon bonds in the aromatic rings into smaller fragments under UV light [98]. The rest of the SAM molecules (MC-54 and MC-55) based perovskite devices showed slightly slower decays, the 80% of initial efficiency is recorded 15 h and 30 h for MC-54 and MC-55, respectively (Figure 4.19a). In addition, stability of the SAM molecules on ITO surface was determined by cyclic voltammetry method (Figure 4.19b-d). The ITO coated surface was used as a working electrode, a platinum wire as a counter electrode, and Ag wire as a reference electrode in acetonitrile supporting electrolyte, and 0.1 M TBAPF6. After MC-45, MC-54 and MC-55 molecules coated on ITO surface CV was performed on substrates for 30 cycles. As can be seen from Figure 4.19b-d, the inflection points of each cycle is at the same point. These results showed that MC-45, MC-54 and MC-55 coating is very stable in terms of electrochemical compounds attached to the ITO surface [141].

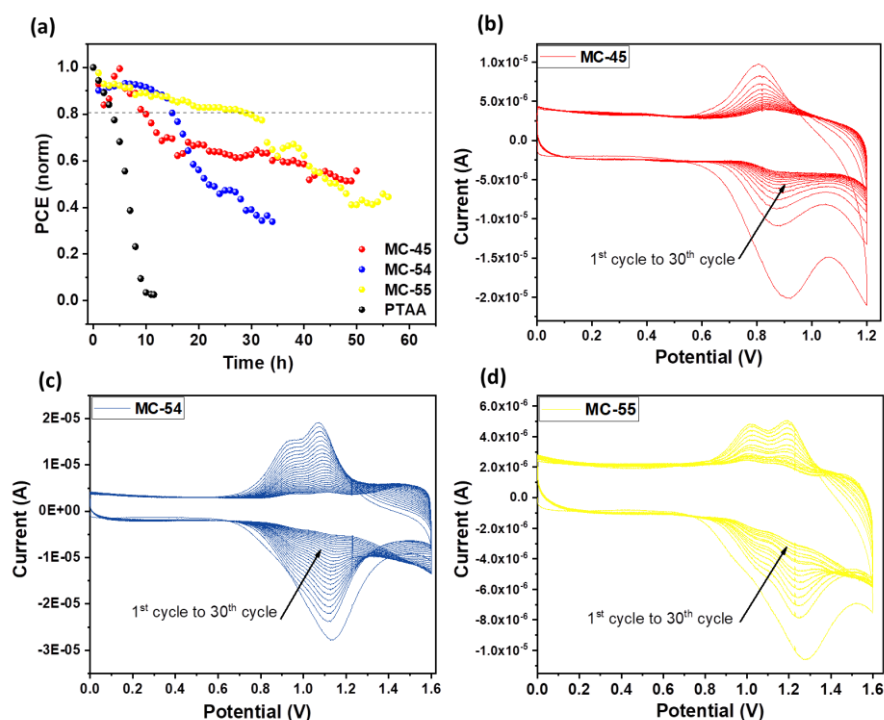


Figure 4.19: Stability of the completed PSCs based on SAMs and PTAA (a), and stability of SAM molecules on ITO for MC-45 (b), MC-54 (c) and MC-55 (d) measured by CV for 30th cycles

After the measuring of photovoltaic performance of devices, we focused on analyzing transient photocurrent (TPC), transient photovoltage (TPV), and differential capacitance (DC) techniques to investigate carrier recombination, carrier transport, and carrier lifetime of complete devices under operation conditions. Our group has described these techniques in depth elsewhere [142]. Therefore, each will be briefly mentioned.

Figure 4.20 shows the charges stored in the PSCs under different V_{OC} values. Each curve fitted to the linear plus exponential dependence law [143]. The geometrical capacitance of free charges accumulating in the selective contacts causes the linear component [144]. After contacts are saturated with charges, they start accumulated in the perovskite bulk and it shows an exponential trend [145]. This is called chemical capacitance. The solid lines at the bottom of Figure 4.20 indicate carriers in the perovskite bulk. Geometric capacitance (C_{geo}) is extracted (dashed lines) from the total charge (symbols). As can be observed from Figure 4.20, the voltage at which chemical capacitance becomes suitable for each device follows the trend MC-54 > MC-55 > MC-45.

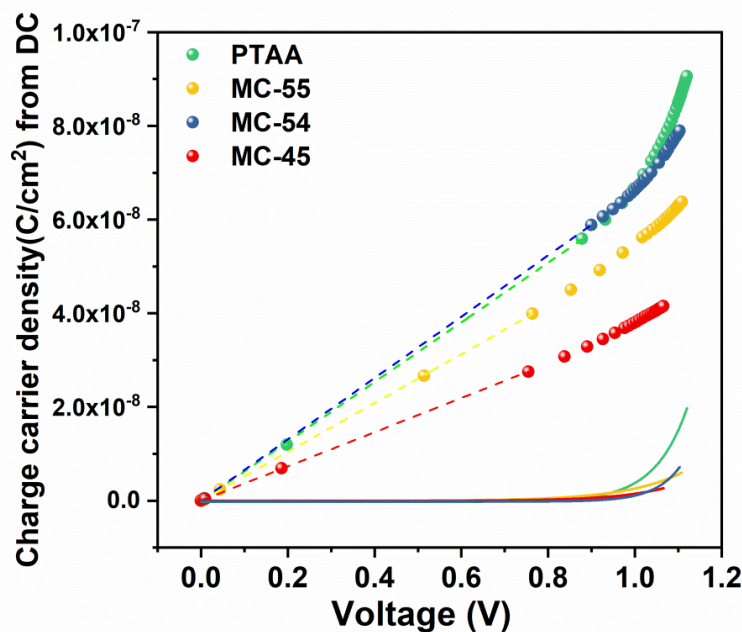


Figure 4.20: Differential capacitance at different light bias with and without C_{geo} for PSCs with different HTMs. Dashed lines correspond to linear fitting of C_{geo} . Solid lines (at the bottom) correspond to carrier density after subtraction of geometrical capacitance

In order to study interface recombination, TPV measurements are carried out on PSCs under open-circuit conditions. The charge (n) affects the kinetic of carrier recombination. As a result, plotting the data extracted from the TPV measurements versus charge is suited for an appropriate comparison between different devices [146, 147], as shown in Figure 4.21a. Figure 4.21b shows the values after geometrical capacitance subtraction. The solid vertical line compares differences in carrier lifetime at equal charge values. According to the results, devices with MC-45 show faster recombination than devices with MC-54 and MC-55. Devices with MC-54 and PTAA almost show the same recombination trend. Therefore, the recombination order can be shown as $MC-45 > MC-55 > MC-54$. In this instance, it is possible to obtain recombination order (δ) as the power-law slope from Figure 4.21b.

$$\tau_{\Delta n} = \tau_{\Delta n0} (n/n_0)^{-\lambda} \quad (4.2)$$

Where λ is the slope of power-law and it is correlate with the recombination order (δ) as $\delta = \lambda + 1$, n_0 is the charge density in the equilibrium and $\tau_{\Delta n0}$ is the equilibrium small perturbation life time. From Figure 4.21b, recombination orders was obtained as 1.06 for (MC-45), 1.08 for (MC-55) and 1.13 for (MC-54). As can be seen, the recombination kinetics of all devices follows the same slope trend. The deducted recombination orders confirm that all devices are ruled by first-order ($\delta = 1$) recombination dynamic [148].

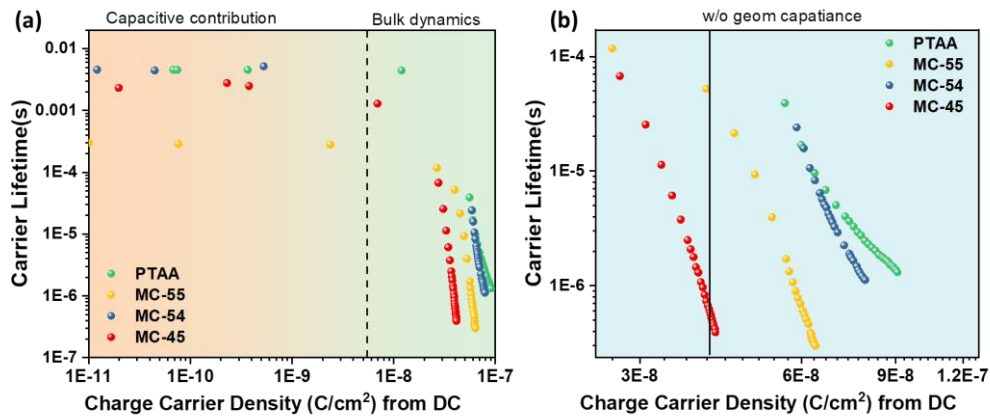


Figure 4.21: (a) Charge (n) carrier measured from DC vs carrier lifetime obtained via TPV for different HTMs and (b) after subtraction of geometrical capacitance

4.3 Conclusion

In summary, we reported three novel SAM molecules, MC-45, MC-54 and MC-55 as HTL and integrated into p-i-n structure perovskite solar cells. SAM treatment is demonstrated as an effective way to adjust the work function of ITO to reduce the energetic barrier between perovskite and ITO electrode. The presence of SAM molecules on the ITO surface is confirmed by XPS, CV, AFM, KPFM and contact angle measurements. The modification of SAMs led to formation of high quality perovskite films with larger grain size and lower density of traps as indicated in XRD analysis and FESEM images. PL and TrPL results show that SAM molecules reduced non-radiative recombination at the interface between perovskite absorber and contacts. Photovoltaic performance of SAM molecules with bidentate anchoring groups (MC-54 and MC-55) have higher PCE than MC-45 which has monodentate anchoring group and current standard polymeric PTAA. An explanation for the better performance of MC-54 and MC-55 is due to their better charge transfer capability that might come from their molecule structure. The best cell performance based MC-54 has 19.52% PCE with a 22.32 mA/cm^2 of J_{SC} , 1.10 V of V_{OC} and 79.15% of FF.

Moreover, SAM modified devices, compared to PTAA-based devices, exhibited high reproducibility according to statistic values and showed higher stability in a light-soaking stability test at open circuit conditions. Finally, we have measured charge carrier density and carrier recombination lifetimes using DC and TPV techniques. It is clearly demonstrated that SAM molecules can increase the charge carrier lifetime and minimize the carrier recombination which totally controls the solar cells efficiency.

Chapter 5

General Conclusion

This thesis aims to utilize novel self-assembled monolayers (SAMs) as a hole transport layer for p-i-n structure perovskite solar cells. The main goal is the replacement of conventional hole transport layers (PEDOT:PSS and PTAA) with SAMs. Indium tin oxide (ITO) is the most used transparent conductive electrode in p-i-n structure PSCs. SAM molecules conformably cover the ITO surface by dip-coating. Afterward, SAM modified substrates are used for the fabrication of PSCs.

In this thesis, different carbazole-based SAM molecules are applied to both MAPI and CsMAFA perovskite devices to analyse the improvement of PSC performance and stability of devices.

In this section, the general conclusion of the thesis are explained briefly for each chapter.

- ❖ In the third chapter, two novel SAM molecules, named TPA and MC-43, were used as hole transport materials instead of PEDOT:PSS in p-i-n structure MAPI perovskite solar cells. With these molecules, we demonstrated for the first time that SAMs can be used efficiently as hole transport materials. The perovskite solar cells fabricated with these SAM molecules showed remarkable PCE. The best cell based on TPA scored 15.9% PCE with a FF of 77%, V_{OC} of 1.06 V and J_{SC} of 19.4 mA cm^{-2} . The best performing MC-43 cell scored 17.3% with a FF of 80%, V_{OC} of 1.07 V and J_{SC} of 20.3 mA cm^{-2} . As a result of our work, these molecules could be a viable alternative to the traditional polymers for improving the stability and durability of p-i-n structure perovskite solar cells

❖ In the fourth chapter, 3 novel SAM molecules with carboxylic acid as anchoring groups were used as HTLs for inverted perovskite solar cells. At the same time, PTAA was used as a baseline HTL for performance comparison. Two of these molecules have bidentate anchoring group (MC-54 and MC-55) while the one has monodentate anchoring (MC-45). Besides the PTAA comparison, we also have compared those two types of molecules. Photovoltaic performance of the SAM-based two-anchor group has higher PCE than MC-45 and current standard polymeric PTAA. The best PCE of MC-54 and MC-55 is 19.52% and 18.99% surpassing the best value of MC-45 (16.69%) and PTAA (18.62). An explanation for the better performance exhibited by MC-54 and MC-55 is due to their better charge transfer capability that might come from their molecule structure. Last of all these results show that high efficiency is achieved by using those molecules which can form SAM onto ITO surface through their anchoring groups without any inorganic or organic hole transporting material like PEDOT:PSS or PTAA.

References

- [1] Olabi A, Abdelkareem MA. Renewable energy and climate change. *Renewable and Sustainable Energy Reviews*. 2022;158:112111.
- [2] Yang X, Pang J, Teng F, Gong R, Springer C. The environmental co-benefit and economic impact of China's low-carbon pathways: Evidence from linking bottom-up and top-down models. *Renewable and Sustainable Energy Reviews*. 2021;136:110438.
- [3] Curtin J, McInerney C, Gallachóir BÓ, Hickey C, Deane P, Deeney P. Quantifying stranding risk for fossil fuel assets and implications for renewable energy investment: a review of the literature. *Renewable and Sustainable Energy Reviews*. 2019;116:109402.
- [4] Olabi A, Obaideen K, Elsaid K, Wilberforce T, Sayed ET, Maghrabie HM, et al. Assessment of the pre-combustion carbon capture contribution into sustainable development goals SDGs using novel indicators. *Renewable and Sustainable Energy Reviews*. 2022;153:111710.
- [5] Quereshi S, Jadhao PR, Pandey A, Ahmad E, Pant K. Overview of sustainable fuel and energy technologies. *Sustainable Fuel Technologies Handbook*: Elsevier; 2021. p. 3-25.
- [6] Burke MJ, Stephens JC. Political power and renewable energy futures: A critical review. *Energy Research & Social Science*. 2018;35:78-93.
- [7] Chapin DM, Fuller CS, Pearson GL. A new silicon p-n junction photocell for converting solar radiation into electrical power. *Journal of applied physics*. 1954;25(5):676-7.
- [8] Kojima A, Teshima K, Shirai Y, Miyasaka T. Organometal halide perovskites as visible-light sensitizers for photovoltaic cells. *Journal of the american chemical society*. 2009;131(17):6050-1.

- [9] NREL. Best Research-Cells Efficiency Chart 2022, May [Available from: <https://www.nrel.gov/pv/cell-efficiency.html>].
- [10] Rose G. Description of some New Minerals from the Urals. *Ann Phys.* 1839;124:551-73.
- [11] Chu Z, Chu X, Zhao Y, Ye Q, Jiang J, Zhang X, et al. Emerging Low-Dimensional Crystal Structure of Metal Halide Perovskite Optoelectronic Materials and Devices. *Small Structures.* 2021;2(6):2000133.
- [12] Lee JW, Kim DH, Kim HS, Seo SW, Cho SM, Park NG. Formamidinium and cesium hybridization for photo-and moisture-stable perovskite solar cell. *Advanced Energy Materials.* 2015;5(20):1501310.
- [13] Hu W, Cong H, Huang W, Huang Y, Chen L, Pan A, et al. Germanium/perovskite heterostructure for high-performance and broadband photodetector from visible to infrared telecommunication band. *Light: Science & Applications.* 2019;8(1):1-10.
- [14] Moore D, Kamino B, Patel J, Miranda L, Johnston M, Parrott E, et al. Bandgap-Tunable Cesium Lead Halide Perovskites with High Thermal Stability for Efficient Solar Cells. *Adv. Energy Mater.* 2016;6:1502458.
- [15] Heo J, Im S, Noh J, Madal T, Lim C, Chang J, et al. *Nat. Photonics*, 2013, 7, 486;(c) JH Noh, SH Im, JH Heo, TN Mandal and SI Seok. *Nano Lett.* 2013;13:1764.
- [16] Green MA, Ho-Baillie A, Snaith HJ. The emergence of perovskite solar cells. *Nature photonics.* 2014;8(7):506-14.
- [17] Lu P, Lu M, Wang H, Sui N, Shi Z, Yu WW, et al. Metal halide perovskite nanocrystals and their applications in optoelectronic devices. *InfoMat.* 2019;1(4):430-59.
- [18] Li C, Lu X, Ding W, Feng L. Y. Gao et Z. Guo. *Acta Crystal B.* 2008;64:702.
- [19] Ortiz-Cervantes C, Carmona-Monroy P, Solis-Ibarra D. Two-dimensional halide perovskites in solar cells: 2D or not 2D? *ChemSusChem.* 2019;12(8):1560-75.

- [20] Dong Q, Fang Y, Shao Y, Mulligan P, Qiu J, Cao Lei and Huang JS 2015. *Science*.347:967.
- [21] Nie W, Tsai H, Asadpour R, Blancon J-C, Neukirch AJ, Gupta G, et al. High-efficiency solution-processed perovskite solar cells with millimeter-scale grains. *Science*. 2015;347(6221):522-5.
- [22] Kim H-S, Lee C-R, Im J-H, Lee K-B, Moehl T, Marchioro A, et al. Lead iodide perovskite sensitized all-solid-state submicron thin film mesoscopic solar cell with efficiency exceeding 9%. *Scientific reports*. 2012;2(1):1-7.
- [23] Cho YJ, Jeong MJ, Park JH, Hu W, Lim J, Chang HS. Charge Transporting Materials Grown by Atomic Layer Deposition in Perovskite Solar Cells. *Energies*. 2021;14(4):1156.
- [24] Rakstys K, Igci C, Nazeeruddin MK. Efficiency vs. stability: dopant-free hole transporting materials towards stabilized perovskite solar cells. *Chemical Science*. 2019;10(28):6748-69.
- [25] Sun S, Buonassisi T, Correa-Baena JP. State-of-the-art electron-selective contacts in perovskite solar cells. *Advanced Materials Interfaces*. 2018;5(22):1800408.
- [26] Tress W, Marinova N, Inganäs O, Nazeeruddin MK, Zakeeruddin SM, Graetzel M, editors. The role of the hole-transport layer in perovskite solar cells-Reducing recombination and increasing absorption. 2014 IEEE 40th Photovoltaic Specialist Conference (PVSC); 2014: IEEE.
- [27] Bi D, Yang L, Boschloo G, Hagfeldt A, Johansson EM. Effect of different hole transport materials on recombination in CH₃NH₃PbI₃ perovskite-sensitized mesoscopic solar cells. *The journal of physical chemistry letters*. 2013;4(9):1532-6.
- [28] Snaith HJ, Abate A, Ball JM, Eperon GE, Leijtens T, Noel NK, et al. Anomalous hysteresis in perovskite solar cells. *The journal of physical chemistry letters*. 2014;5(9):1511-5.
- [29] Liu P, Wang W, Liu S, Yang H, Shao Z. Fundamental understanding of photocurrent hysteresis in perovskite solar cells. *Advanced Energy Materials*. 2019;9(13):1803017.

- [30] Rong Y, Hu Y, Ravishankar S, Liu H, Hou X, Sheng Y, et al. Tunable hysteresis effect for perovskite solar cells. *Energy & Environmental Science*. 2017;10(11):2383-91.
- [31] Zhang Z, Men B, Liu Y, Gao H, Mao Y. Effects of precursor solution composition on the performance and IV hysteresis of perovskite solar cells based on $\text{CH}_3\text{NH}_3\text{PbI}_{3-x}\text{Cl}_x$. *Nanoscale Research Letters*. 2017;12(1):1-8.
- [32] Kang DH, Park NG. On the current–voltage hysteresis in perovskite solar cells: dependence on perovskite composition and methods to remove hysteresis. *Advanced Materials*. 2019;31(34):1805214.
- [33] Azpiroz J, Mosconi E, Bisquert J, Angelis F. *Energy Environ. Sc*; 2015.
- [34] Lee J-W, Kim S-G, Bae S-H, Lee D-K, Lin O, Yang Y, et al. The interplay between trap density and hysteresis in planar heterojunction perovskite solar cells. *Nano letters*. 2017;17(7):4270-6.
- [35] Tress W, Marinova N, Moehl T, Zakeeruddin SM, Nazeeruddin MK, Grätzel M. Understanding the rate-dependent J–V hysteresis, slow time component, and aging in $\text{CH}_3\text{NH}_3\text{PbI}_3$ perovskite solar cells: the role of a compensated electric field. *Energy & Environmental Science*. 2015;8(3):995-1004.
- [36] Wu F, Pathak R, Qiao Q. Origin and alleviation of JV hysteresis in perovskite solar cells: A short review. *Catalysis Today*. 2021;374:86-101.
- [37] Li Z, Xiao C, Yang Y, Harvey S, Kim D, Christians J, et al. AM M, and K. Zhu. *Energy Environ Sci*. 2017;10:C7EE00358G.
- [38] Liu J, Yin X, Liu X, Que M, Que W. Multi-influences of ionic migration on illumination-dependent electrical performances of inverted perovskite solar cells. *The Journal of Physical Chemistry C*. 2017;121(29):16051-7.
- [39] De Bastiani M, Dell'Erba G, Gandini M, D'Innocenzo V, Neutzner S, Kandada ARS, et al. Ion migration and the role of preconditioning cycles in the stabilization of the J–V characteristics of inverted hybrid perovskite solar cells. *Advanced Energy Materials*. 2016;6(2):1501453.

- [40] Xu T, Chen L, Guo Z, Ma T. Strategic improvement of the long-term stability of perovskite materials and perovskite solar cells. *Physical Chemistry Chemical Physics*. 2016;18(39):27026-50.
- [41] Cao X, Li Y, Li C, Fang F, Yao Y, Cui X, et al. Modulating hysteresis of perovskite solar cells by a poling voltage. *The Journal of Physical Chemistry C*. 2016;120(40):22784-92.
- [42] Tress W, Correa Baena JP, Saliba M, Abate A, Graetzel M. Inverted current–voltage hysteresis in mixed perovskite solar cells: polarization, energy barriers, and defect recombination. *Advanced Energy Materials*. 2016;6(19):1600396.
- [43] Zhang Y, Liu M, Eperon GE, Leijtens TC, McMeekin D, Saliba M, et al. Charge selective contacts, mobile ions and anomalous hysteresis in organic–inorganic perovskite solar cells. *Materials Horizons*. 2015;2(3):315-22.
- [44] Casalini S, Bortolotti CA, Leonardi F, Biscarini F. Self-assembled monolayers in organic electronics. *Chemical Society Reviews*. 2017;46(1):40-71.
- [45] Nicosia C, Huskens J. Reactive self-assembled monolayers: from surface functionalization to gradient formation. *Materials horizons*. 2014;1(1):32-45.
- [46] Ulman A. Formation and structure of self-assembled monolayers. *Chemical reviews*. 1996;96(4):1533-54.
- [47] Bigelow W, Pickett D, Zisman W. Oleophobic monolayers: I. Films adsorbed from solution in non-polar liquids. *Journal of Colloid Science*. 1946;1(6):513-38.
- [48] Khassanov A, Steinrück H-G, Schmaltz T, Magerl A, Halik M. Structural investigations of self-assembled monolayers for organic electronics: Results from X-ray reflectivity. *Accounts of chemical research*. 2015;48(7):1901-8.
- [49] Kim SY, Cho SJ, Byeon SE, He X, Yoon HJ. Self-Assembled Monolayers as Interface Engineering Nanomaterials in Perovskite Solar Cells. *Advanced Energy Materials*. 2020;10(44):2002606.

- [50] Burkhardt M, Jedaa A, Novak M, Ebel A, Voitchovsky K, Stellacci F, et al. Concept of a Molecular Charge Storage Dielectric Layer for Organic Thin-Film Memory Transistors. *Advanced Materials*. 2010;22(23):2525-8.
- [51] Metzger RM. Unimolecular electronics. *Chemical reviews*. 2015;115(11):5056-115.
- [52] Schwartz DK. Mechanisms and kinetics of self-assembled monolayer formation. *Annual review of physical chemistry*. 2001;52(1):107-37.
- [53] Singh M, Kaur N, Comini E. The role of self-assembled monolayers in electronic devices. *Journal of Materials Chemistry C*. 2020;8(12):3938-55.
- [54] Ma H, Yip HL, Huang F, Jen AKY. Interface engineering for organic electronics. *Advanced Functional Materials*. 2010;20(9):1371-88.
- [55] Choi K, Choi H, Min J, Kim T, Kim D, Son SY, et al. A Short Review on Interface Engineering of Perovskite Solar Cells: A Self-Assembled Monolayer and Its Roles. *Solar RRL*. 2020;4(2):1900251.
- [56] Bauer T, Schmaltz T, Lenz T, Halik M, Meyer B, Clark T. Phosphonate-and carboxylate-based self-assembled monolayers for organic devices: a theoretical study of surface binding on aluminum oxide with experimental support. *ACS Applied Materials & Interfaces*. 2013;5(13):6073-80.
- [57] Paniagua SA, Giordano AJ, Smith ONL, Barlow S, Li H, Armstrong NR, et al. Phosphonic acids for interfacial engineering of transparent conductive oxides. *Chemical reviews*. 2016;116(12):7117-58.
- [58] Wang P, Klein C, Moser J-E, Humphry-Baker R, Cevey-Ha N-L, Charvet R, et al. Amphiphilic ruthenium sensitizer with 4, 4'-diphosphonic acid-2, 2'-bipyridine as anchoring ligand for nanocrystalline dye sensitized solar cells. *The Journal of Physical Chemistry B*. 2004;108(45):17553-9.
- [59] Wojciechowski S, Stranks AA. G. Sadoughi, A. Sadhanala, N. Kopidakis, G. Rumbles, C. Z Li, RH Friend, AK-Y Jen, and HJ Snaith, *ACS Nano*. 2014;8:12701.
- [60] Zuo L, Gu Z, Ye T, Fu W, Wu G, Li H, et al. Enhanced photovoltaic performance of CH₃NH₃PbI₃ perovskite solar cells through interfacial

- engineering using self-assembling monolayer. *Journal of the American Chemical Society*. 2015;137(7):2674-9.
- [61] Bai Y, Dong Q, Shao Y, Deng Y, Wang Q, Shen L, et al. Enhancing stability and efficiency of perovskite solar cells with crosslinkable silane-functionalized and doped fullerene. *Nature communications*. 2016;7(1):1-9.
- [62] Yalcin E, Can M, Rodriguez-Seco C, Aktas E, Pudi R, Cambarau W, et al. Semiconductor self-assembled monolayers as selective contacts for efficient PiN perovskite solar cells. *Energy & Environmental Science*. 2019;12(1):230-7.
- [63] Saliba M, Correa-Baena J-P, Wolff CM, Stolterfoht M, Phung N, Albrecht S, et al. How to Make over 20% Efficient Perovskite Solar Cells in Regular (n-i-p) and Inverted (p-i-n) Architectures. *Chemistry of Materials*. 2018;30(13):4193-201.
- [64] Koster LJA, Mihailetschi VD, Ramaker R, Blom PW. Light intensity dependence of open-circuit voltage of polymer: fullerene solar cells. *Applied physics letters*. 2005;86(12):123509.
- [65] Shockley W, Read Jr W. Statistics of the recombinations of holes and electrons. *Physical review*. 1952;87(5):835.
- [66] Tress W, Yavari M, Domanski K, Yadav P, Niesen B, Correa P. Interpretation and evolution of open-circuit voltage, recombination, ideality factor and subgap irreversible degradation of perovskite solar cells. *Energy Environ Sci*. 2017;11:151-65.
- [67] Kuik M, Koster L, Wetzelaer G, Blom P. Trap-assisted recombination in disordered organic semiconductors. *Physical review letters*. 2011;107(25):256805.
- [68] Yang WS, Park B-W, Jung EH, Jeon NJ, Kim YC, Lee DU, et al. Iodide management in formamidinium-lead-halide-based perovskite layers for efficient solar cells. *Science*. 2017;356(6345):1376-9.
- [69] Wu Z, Raga SR, Juarez-Perez EJ, Yao X, Jiang Y, Ono LK, et al. Improved Efficiency and Stability of Perovskite Solar Cells Induced by C₆₀O

- Functionalized Hydrophobic Ammonium-Based Additives. *Advanced Materials*. 2018;30(3):1703670.
- [70] Pont S, Bryant D, Lin C-T, Aristidou N, Wheeler S, Ma X, et al. Tuning CH₃NH₃Pb(I_{1-x}Br_x)₃ perovskite oxygen stability in thin films and solar cells. *Journal of Materials Chemistry A*. 2017;5(20):9553-60.
- [71] Salim T, Sun S, Abe Y, Krishna A, Grimsdale AC, Lam YM. Perovskite-based solar cells: impact of morphology and device architecture on device performance. *Journal of Materials Chemistry A*. 2015;3(17):8943-69.
- [72] Burschka J, Pellet N, Moon S-J, Humphry-Baker R, Gao P, Nazeeruddin MK, et al. Sequential deposition as a route to high-performance perovskite-sensitized solar cells. *Nature*. 2013;499(7458):316-9.
- [73] Xiao Z, Bi C, Shao Y, Dong Q, Wang Q, Yuan Y, et al. Efficient, high yield perovskite photovoltaic devices grown by interdiffusion of solution-processed precursor stacking layers. *Energy & Environmental Science*. 2014;7(8):2619-23.
- [74] Jeon NJ, Noh JH, Kim YC, Yang WS, Ryu S, Seok SI. Solvent engineering for high-performance inorganic-organic hybrid perovskite solar cells. *Nature materials*. 2014;13(9):897-903.
- [75] Eperon GE, Burlakov VM, Docampo P, Goriely A, Snaith HJ. Morphological control for high performance, solution-processed planar heterojunction perovskite solar cells. *Advanced functional materials*. 2014;24(1):151-7.
- [76] Xiao Z, Dong Q, Bi C, Shao Y, Yuan Y, Huang J. Solvent annealing of perovskite-induced crystal growth for photovoltaic-device efficiency enhancement. *Advanced Materials*. 2014;26(37):6503-9.
- [77] Schulz P, Edri E, Kirmayer S, Hodes G, Cahen D, Kahn A. Interface energetics in organo-metal halide perovskite-based photovoltaic cells. *Energy & Environmental Science*. 2014;7(4):1377-81.
- [78] Ameen S, Rub MA, Kosa SA, Alamry KA, Akhtar MS, Shin HS, et al. Perovskite solar cells: influence of hole transporting materials on power conversion efficiency. *ChemSusChem*. 2016;9(1):10-27.

- [79] Hu Q, Wu J, Jiang C, Liu T, Que X, Zhu R, et al. Engineering of electron-selective contact for perovskite solar cells with efficiency exceeding 15%. *ACS nano*. 2014;8(10):10161-7.
- [80] Kim H, Lim K-G, Lee T-W. Planar heterojunction organometal halide perovskite solar cells: roles of interfacial layers. *Energy & Environmental Science*. 2016;9(1):12-30.
- [81] Heo JH, Han HJ, Kim D, Ahn TK, Im SH. Hysteresis-less inverted CH₃NH₃PbI₃ planar perovskite hybrid solar cells with 18.1% power conversion efficiency. *Energy & Environmental Science*. 2015;8(5):1602-8.
- [82] Bai Y, Chen H, Xiao S, Xue Q, Zhang T, Zhu Z, et al. Effects of a molecular monolayer modification of NiO nanocrystal layer surfaces on perovskite crystallization and interface contact toward faster hole extraction and higher photovoltaic performance. *Advanced Functional Materials*. 2016;26(17):2950-8.
- [83] Kırbıyık Ç, Kara K, Kara DA, Yiğit MZ, Istanbulu B, Can M, et al. Enhancing the c-TiO₂ based perovskite solar cell performance via modification by a serial of boronic acid derivative self-assembled monolayers. *Applied Surface Science*. 2017;423:521-7.
- [84] Tozlu C, Mutlu A, Can M, Havare AK, Demic S, Icli S. Effect of TiO₂ modification with amino-based self-assembled monolayer on inverted organic solar cell. *Applied Surface Science*. 2017;422:1129-38.
- [85] Chang C-Y, Chang Y-C, Huang W-K, Liao W-C, Wang H, Yeh C, et al. Achieving high efficiency and improved stability in large-area ITO-free perovskite solar cells with thiol-functionalized self-assembled monolayers. *Journal of Materials Chemistry A*. 2016;4(20):7903-13.
- [86] Yang G, Wang C, Lei H, Zheng X, Qin P, Xiong L, et al. Interface engineering in planar perovskite solar cells: energy level alignment, perovskite morphology control and high performance achievement. *Journal of Materials Chemistry A*. 2017;5(4):1658-66.

- [87] Prieto P, Nistor V, Nouneh K, Oyama M, Abd-Lefdil M, Díaz R. XPS study of silver, nickel and bimetallic silver–nickel nanoparticles prepared by seed-mediated growth. *Applied Surface Science*. 2012;258(22):8807-13.
- [88] Liu T, Chen K, Hu Q, Zhu R, Gong Q. Inverted perovskite solar cells: progresses and perspectives. *Advanced Energy Materials*. 2016;6(17):1600457.
- [89] Akın Kara D, Kara K, Oylumluoglu G, Yigit MZ, Can M, Kim JJ, et al. Enhanced device efficiency and long-term stability via boronic acid-based self-assembled monolayer modification of indium tin oxide in a planar perovskite solar cell. *ACS applied materials & interfaces*. 2018;10(35):30000-7.
- [90] Park N-G. High efficiency mesoscopic organometal halide perovskite solar cells. 2016.
- [91] Docampo P, Ball JM, Darwich M, Eperon GE, Snaith HJ. Efficient organometal trihalide perovskite planar-heterojunction solar cells on flexible polymer substrates. *Nature communications*. 2013;4(1):1-6.
- [92] Malinkiewicz O, Yella A, Lee YH, Espallargas GM, Graetzel M, Nazeeruddin MK, et al. Perovskite solar cells employing organic charge-transport layers. *Nature Photonics*. 2014;8(2):128-32.
- [93] Saliba M, Stolterfoht M, Wolff CM, Neher D, Abate A. Measuring aging stability of perovskite solar cells. *Joule*. 2018;2(6):1019-24.
- [94] Magomedov A, Kasparavičius E, Rakstys K, Paek S, Gasilova N, Genevičius K, et al. Pyridination of hole transporting material in perovskite solar cells questions the long-term stability. *Journal of Materials Chemistry C*. 2018;6(33):8874-8.
- [95] You J, Guo F, Qiu S, He W, Wang C, Liu X, et al. The fabrication of homogeneous perovskite films on non-wetting interfaces enabled by physical modification. *Journal of Energy Chemistry*. 2019;38:192-8.
- [96] Stolterfoht M, Wolff CM, Amir Y, Paulke A, Perdigón-Toro L, Caprioglio P, et al. Approaching the fill factor Shockley–Queisser limit in stable, dopant-

- free triple cation perovskite solar cells. *Energy & Environmental Science*. 2017;10(6):1530-9.
- [97] Magomedov A, Al-Ashouri A, Kasparavičius E, Strazdaite S, Niaura G, Jošt M, et al. Self-assembled hole transporting monolayer for highly efficient perovskite solar cells. *Advanced energy materials*. 2018;8(32):1801892.
- [98] Aktas E, Phung N, Köbler H, González DA, Méndez M, Kafedjiska I, et al. Understanding the perovskite/self-assembled selective contact interface for ultra-stable and highly efficient p–i–n perovskite solar cells. *Energy & Environmental Science*. 2021;14(7):3976-85.
- [99] Al-Ashouri A, Magomedov A, Roß M, Jošt M, Talaikis M, Chistiakova G, et al. Conformal monolayer contacts with lossless interfaces for perovskite single junction and monolithic tandem solar cells. *Energy & Environmental Science*. 2019;12(11):3356-69.
- [100] Ullah A, Park KH, Nguyen HD, Siddique Y, Shah S, Tran H, et al. Novel Phenothiazine-Based Self-Assembled Monolayer as a Hole Selective Contact for Highly Efficient and Stable p-i-n Perovskite Solar Cells. *Advanced Energy Materials*. 2022;12(2):2103175.
- [101] Brennan BJ, Portolés MJL, Liddell PA, Moore TA, Moore AL, Gust D. Comparison of silatrane, phosphonic acid, and carboxylic acid functional groups for attachment of porphyrin sensitizers to TiO₂ in photoelectrochemical cells. *Physical Chemistry Chemical Physics*. 2013;15(39):16605-14.
- [102] Havare AK, Can M, Demic S, Okur S, Kus M, Aydın H, et al. Modification of ITO surface using aromatic small molecules with carboxylic acid groups for OLED applications. *Synthetic Metals*. 2011;161(21-22):2397-404.
- [103] Arkan E, Unal M, Yalcin E, Arkan MZY, Yurtdas S, Can M, et al. Influence of end groups variation of self assembled monolayers on performance of planar perovskite solar cells by interface regulation. *Materials Science in Semiconductor Processing*. 2021;123:105514.

- [104] Yalcin E, Kara DA, Karakaya C, Yigit MZ, Havare AK, Can M, et al. Functionalized organic semiconductor molecules to enhance charge carrier injection in electroluminescent cell. *Optical Materials*. 2017;69:283-90.
- [105] Hou X, Xiao X, Zhou Q-H, Cheng X-F, He J-H, Xu Q-F, et al. Surface engineering to achieve organic ternary memory with a high device yield and improved performance. *Chemical science*. 2017;8(3):2344-51.
- [106] Hotchkiss PJ, Jones SC, Paniagua SA, Sharma A, Kippelen B, Armstrong NR, et al. The modification of indium tin oxide with phosphonic acids: mechanism of binding, tuning of surface properties, and potential for use in organic electronic applications. *Accounts of chemical research*. 2012;45(3):337-46.
- [107] Paramonov PB, Paniagua SA, Hotchkiss PJ, Jones SC, Armstrong NR, Marder SR, et al. Theoretical characterization of the indium tin oxide surface and of its binding sites for adsorption of phosphonic acid monolayers. *Chemistry of Materials*. 2008;20(16):5131-3.
- [108] Huang J, Tan S, Lund PD, Zhou H. Impact of H₂O on organic–inorganic hybrid perovskite solar cells. *Energy & Environmental Science*. 2017;10(11):2284-311.
- [109] Idigoras J, Aparicio FJ, Contreras-Bernal L, Ramos-Terron S, Alcaire M, Sánchez-Valencia JRn, et al. Enhancing moisture and water resistance in perovskite solar cells by encapsulation with ultrathin plasma polymers. *ACS Applied materials & interfaces*. 2018;10(14):11587-94.
- [110] Clegg C, Hill IG. Systematic study on the impact of water on the performance and stability of perovskite solar cells. *Rsc Advances*. 2016;6(57):52448-58.
- [111] Mi X, Rungo BA, Dong X, Liu H, Li X, Wang S. Enhanced efficiency and stability of organic light-emitting diodes via binary self-assembled monolayers of aromatic and aliphatic compounds on indium tin oxide. *Organic Electronics*. 2020;84:105752.
- [112] Bi C, Wang Q, Shao Y, Yuan Y, Xiao Z, Huang J. Non-wetting surface-driven high-aspect-ratio crystalline grain growth for efficient hybrid perovskite solar cells. *Nature communications*. 2015;6(1):1-7.

- [113] Ren X, Yang Z, Yang D, Zhang X, Cui D, Liu Y, et al. Modulating crystal grain size and optoelectronic properties of perovskite films for solar cells by reaction temperature. *Nanoscale*. 2016;8(6):3816-22.
- [114] Yang D, Yang Z, Qin W, Zhang Y, Liu SF, Li C. Alternating precursor layer deposition for highly stable perovskite films towards efficient solar cells using vacuum deposition. *Journal of Materials Chemistry A*. 2015;3(18):9401-5.
- [115] Xiao M, Huang F, Huang W, Dkhissi Y, Zhu Y, Etheridge J, et al. A fast deposition-crystallization procedure for highly efficient lead iodide perovskite thin-film solar cells. *Angewandte Chemie International Edition*. 2014;53(37):9898-903.
- [116] Wu Y, Islam A, Yang X, Qin C, Liu J, Zhang K, et al. Retarding the crystallization of PbI₂ for highly reproducible planar-structured perovskite solar cells via sequential deposition. *Energy & Environmental Science*. 2014;7(9):2934-8.
- [117] Nukunodompanich M, Budiutama G, Suzuki K, Hasegawa K, Ihara M. Dominant effect of the grain size of the MAPbI₃ perovskite controlled by the surface roughness of TiO₂ on the performance of perovskite solar cells. *CrystEngComm*. 2020;22(16):2718-27.
- [118] Huang J, Shao Y, Dong Q. Organometal trihalide perovskite single crystals: a next wave of materials for 25% efficiency photovoltaics and applications beyond? *The Journal of Physical Chemistry Letters*. 2015;6(16):3218-27.
- [119] Long R, Liu J, Prezhdov OV. Unravelling the effects of grain boundary and chemical doping on electron-hole recombination in CH₃NH₃PbI₃ perovskite by time-domain atomistic simulation. *Journal of the American Chemical Society*. 2016;138(11):3884-90.
- [120] Dong Q, Yuan Y, Shao Y, Fang Y, Wang Q, Huang J. Abnormal crystal growth in CH₃NH₃PbI_{3-x}Cl_x using a multi-cycle solution coating process. *Energy & environmental science*. 2015;8(8):2464-70.

- [121] Zhou H, Chen Q, Li G, Luo S, Song T-b, Duan H-S, et al. Interface engineering of highly efficient perovskite solar cells. *Science*. 2014;345(6196):542-6.
- [122] Liu D, Wu L, Li C, Ren S, Zhang J, Li W, et al. Controlling CH₃NH₃PbI_{3-x}Cl_x Film Morphology with Two-Step Annealing Method for Efficient Hybrid Perovskite Solar Cells. *ACS applied materials & interfaces*. 2015;7(30):16330-7.
- [123] Roose B, Dey K, Chiang Y-H, Friend RH, Stranks SD. Critical assessment of the use of excess lead iodide in lead halide perovskite solar cells. *The Journal of Physical Chemistry Letters*. 2020;11(16):6505-12.
- [124] Shi B, Yao X, Hou F, Guo S, Li Y, Wei C, et al. Unraveling the passivation process of PbI₂ to enhance the efficiency of planar perovskite solar cells. *The Journal of Physical Chemistry C*. 2018;122(37):21269-76.
- [125] Du T, Burgess CH, Kim J, Zhang J, Durrant JR, McLachlan MA. Formation, location and beneficial role of PbI₂ in lead halide perovskite solar cells. *Sustainable Energy & Fuels*. 2017;1(1):119-26.
- [126] Yerramilli AS, Chen Y, Sanni D, Asare J, Theodore ND, Alford T. Impact of excess lead on the stability and photo-induced degradation of lead halide perovskite solar cells. *Organic Electronics*. 2018;59:107-12.
- [127] Gujar TP, Unger T, Schönleber A, Fried M, Panzer F, Van Smaalen S, et al. The role of PbI₂ in CH₃NH₃PbI₃ perovskite stability, solar cell parameters and device degradation. *Physical chemistry chemical physics*. 2018;20(1):605-14.
- [128] Shi Y, Zhang H, Tong X, Hou X, Li F, Du Y, et al. Interfacial Engineering via Self-Assembled Thiol Silane for High Efficiency and Stability Perovskite Solar Cells. *Solar RRL*. 2021;5(7):2100128.
- [129] Kim J, Godin R, Dimitrov SD, Du T, Bryant D, McLachlan MA, et al. Excitation density dependent photoluminescence quenching and charge transfer efficiencies in hybrid perovskite/organic semiconductor bilayers. *Advanced Energy Materials*. 2018;8(35):1802474.

- [130] Wen X, Feng Y, Huang S, Huang F, Cheng Y-B, Green M, et al. Defect trapping states and charge carrier recombination in organic–inorganic halide perovskites. *Journal of Materials Chemistry C*. 2016;4(4):793-800.
- [131] Manda PK, Ramaswamy S, Dutta S. Extraction of the built-in potential for organic solar cells from current–voltage characteristics. *IEEE Transactions on Electron Devices*. 2017;65(1):184-90.
- [132] Hara KO, Usami N. Theory of open-circuit voltage and the driving force of charge separation in pn-junction solar cells. *Journal of Applied Physics*. 2013;114(15):153101.
- [133] Subhani WS, Wang K, Du M, Wang X, Liu S. Interface-modification-induced gradient energy band for highly efficient CsPbIBr₂ perovskite solar cells. *Advanced Energy Materials*. 2019;9(21):1803785.
- [134] Sánchez JG, Cabrera-Espinoza A, Martínez-Ferrero E, Delgado JL, Palomares E. Chalcogen-substituted PCBM derivatives as ternary components in PM6: Y6 solar cells. *Materials Advances*. 2022.
- [135] Yin W-J, Shi T, Yan Y. Unusual defect physics in CH₃NH₃PbI₃ perovskite solar cell absorber. *Applied Physics Letters*. 2014;104(6):063903.
- [136] Davies CL, Filip MR, Patel JB, Crothers TW, Verdi C, Wright AD, et al. Bimolecular recombination in methylammonium lead triiodide perovskite is an inverse absorption process. *Nature communications*. 2018;9(1):1-9.
- [137] Credgington D, Kim Y, Labram J, Anthopoulos TD, Durrant JR. Analysis of recombination losses in a pentacene/C₆₀ organic bilayer solar cell. *The Journal of Physical Chemistry Letters*. 2011;2(21):2759-63.
- [138] Ryu S, Ha NY, Ahn Y, Park J-Y, Lee S. Light intensity dependence of organic solar cell operation and dominance switching between Shockley–Read–Hall and bimolecular recombination losses. *Scientific reports*. 2021;11(1):1-10.
- [139] Sun Z, Sitbon G, Pons T, Bakulin AA, Chen Z. Reduced carrier recombination in PbS–CuInS₂ quantum dot solar cells. *Scientific reports*. 2015;5(1):1-11.

- [140] Bahry T, Cui Z, Deniset-Besseau A, Gervais M, Mbomekalle I, Sollogoub C, et al. Optimal strategy based on radiation chemistry for facile and direct synthesis of poly (3-thiophene acetic acid) polymers in water and dichloromethane. *New Journal of Chemistry*. 2020;44(27):11652-66.
- [141] Havare AK, Can M, Tozlu C, Kus M, Okur S, Demic Ş, et al. Charge transfer through amino groups-small molecules interface improving the performance of electroluminescent devices. *Optical Materials*. 2016;55:94-101.
- [142] Palomares E, Montcada NF, Méndez M, Jiménez-López J, Yang W, Boschloo G. Photovoltage/photocurrent transient techniques. *Characterization Techniques for Perovskite Solar Cell Materials*: Elsevier; 2020. p. 161-80.
- [143] Gelmetti I, Montcada NF, Pérez-Rodríguez A, Barrena E, Ocal C, García-Benito I, et al. Energy alignment and recombination in perovskite solar cells: weighted influence on the open circuit voltage. *Energy & Environmental Science*. 2019;12(4):1309-16.
- [144] Ryan JW, Palomares E. Photo-Induced Charge Carrier Recombination Kinetics in Small Molecule Organic Solar Cells and the Influence of Film Nanomorphology. *Advanced Energy Materials*. 2017;7(10):1601509.
- [145] Du T, Kim J, Ngiam J, Xu S, Barnes PR, Durrant JR, et al. Elucidating the Origins of Subgap Tail States and Open-Circuit Voltage in Methylammonium Lead Triiodide Perovskite Solar Cells. *Advanced Functional Materials*. 2018;28(32):1801808.
- [146] Yaghoobi NN, Di Carlo A, Méndez M, Palomares E, Paci B, Generosi A. Analysis of the efficiency losses in hybrid perovskite/PTAA solar cells with different molecular weights: Morphology versus kinetics. *ACS Applied Energy Materials*. 2020;3(7):6853-9.
- [147] Rodríguez-Seco C, Mendez M, Roldán-Carmona C, Pudi R, Nazeeruddin MK, Palomares EJ. Minimization of carrier losses for efficient perovskite solar cells through structural modification of triphenylamine derivatives. *Angewandte Chemie International Edition*. 2020;59(13):5303-7.
- [148] Rodríguez-Seco C, Mendez M, Roldan-Carmona C, Cabau L, Asiri AM, Nazeeruddin MK, et al. Benzothiadiazole Aryl-amine based materials as

efficient hole carriers in perovskite solar cells. *ACS Applied Materials & Interfaces*. 2020;12(29):32712-8.

Appendices

Appendice A

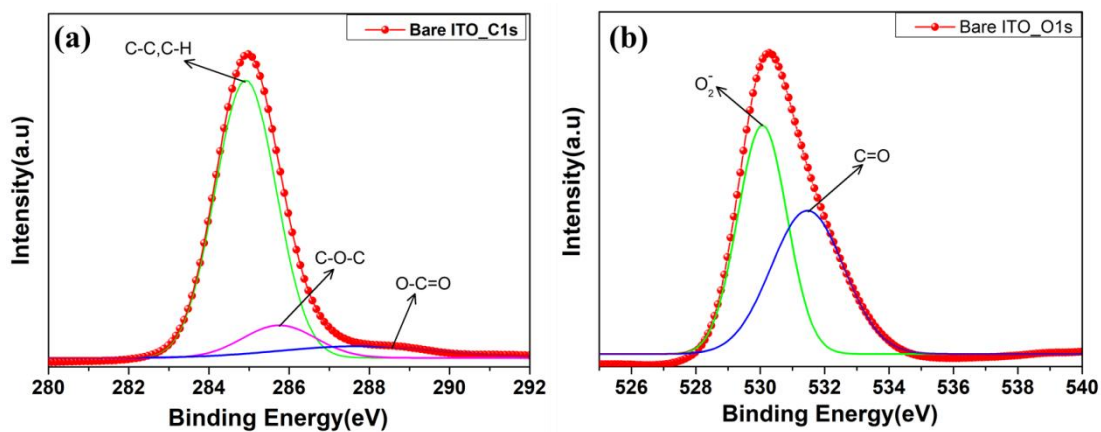


Figure A.1: XPS high-resolution surface spectra of C1s (a) and O1s (b) for bare ITO.

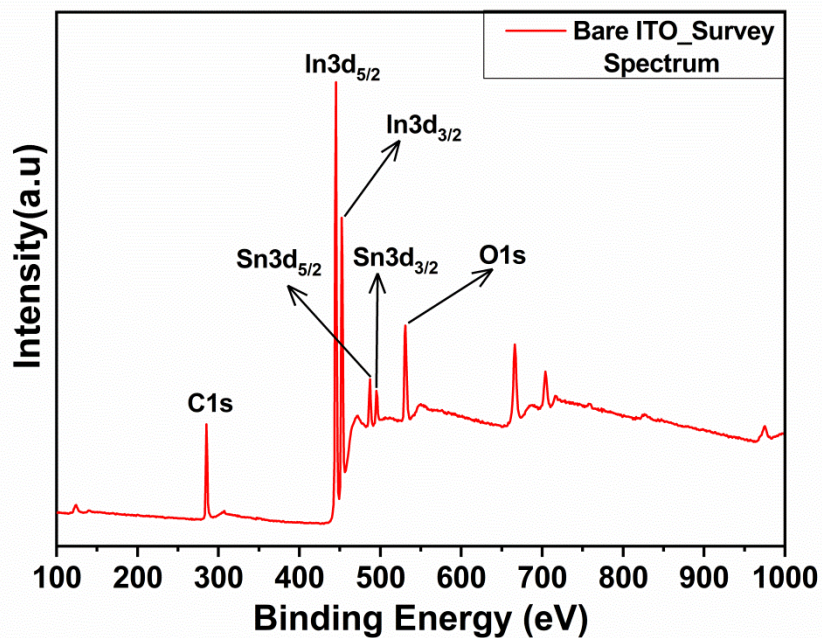


Figure A.2: XPS survey spectrum of bare ITO

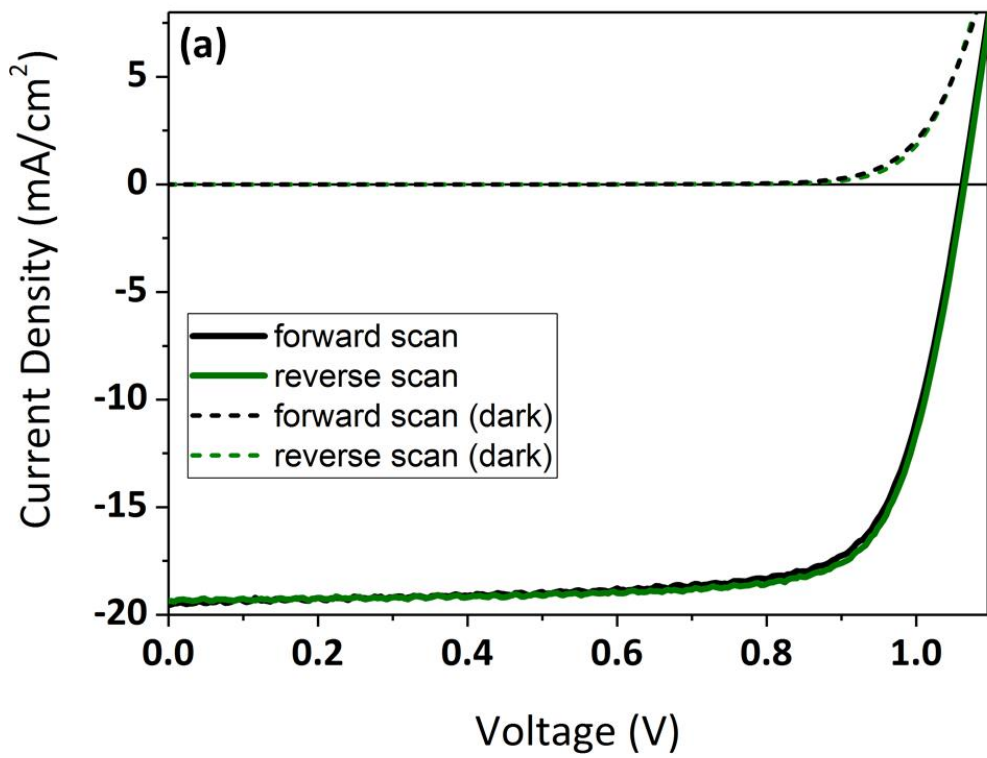
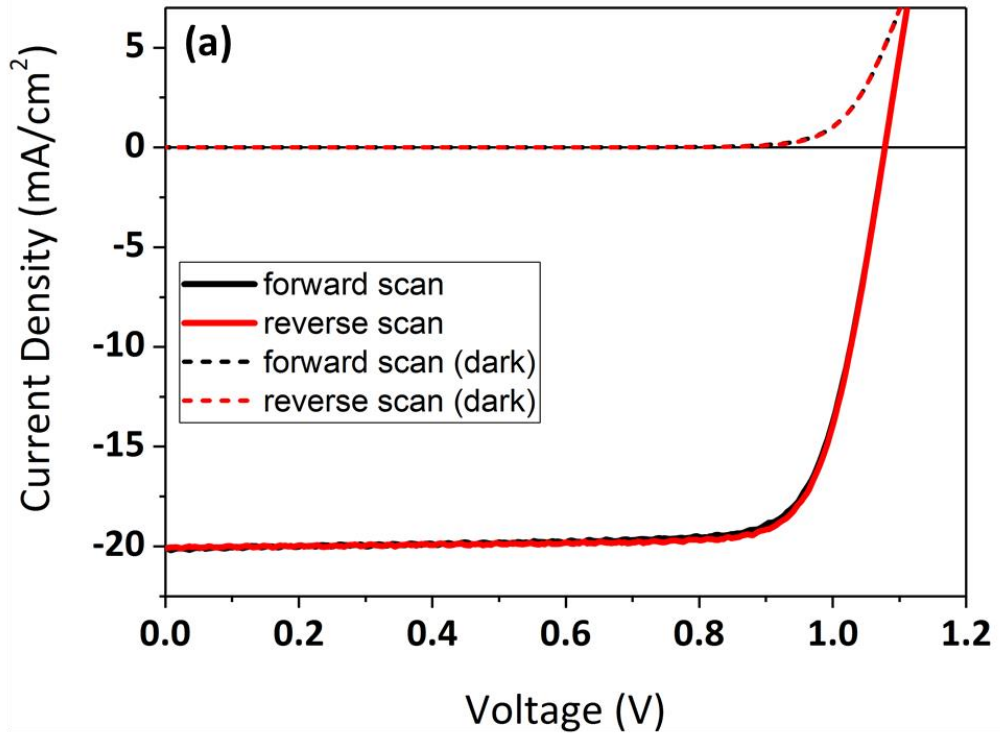


Figure A.3: J - V characteristic of best PSC based on MC-43 (a) and TPA (b) SAM molecules at 1 sun and dark conditions

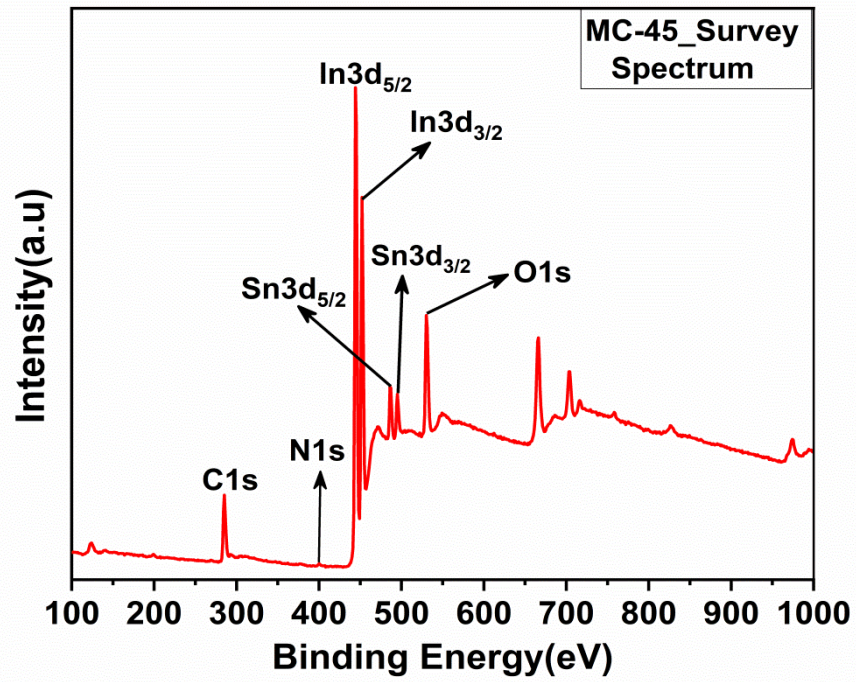


Figure A.4: XPS surface spectrum of ITO/MC-45

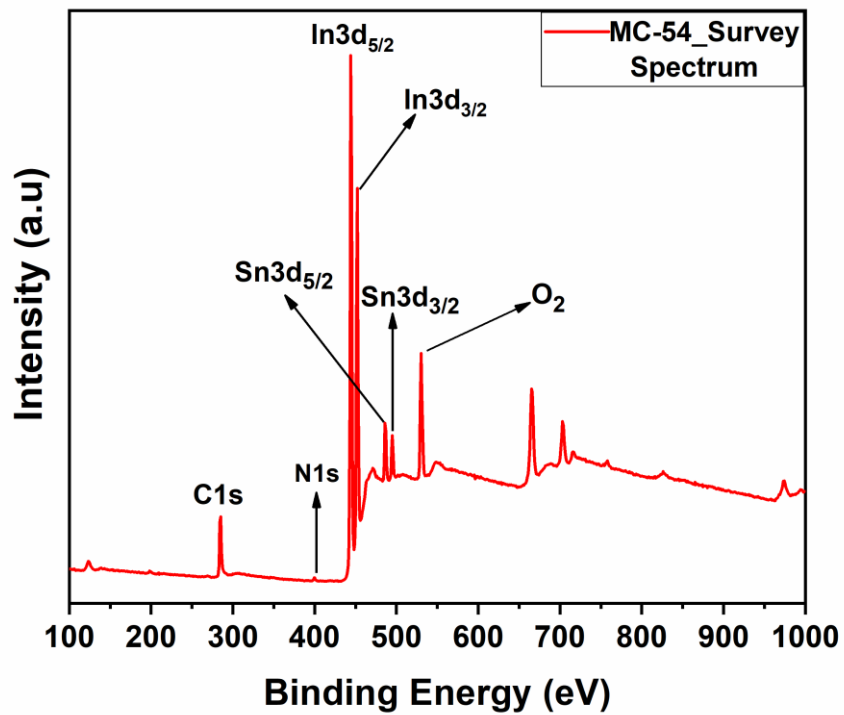


Figure A.5: XPS surface spectrum of ITO/MC-54

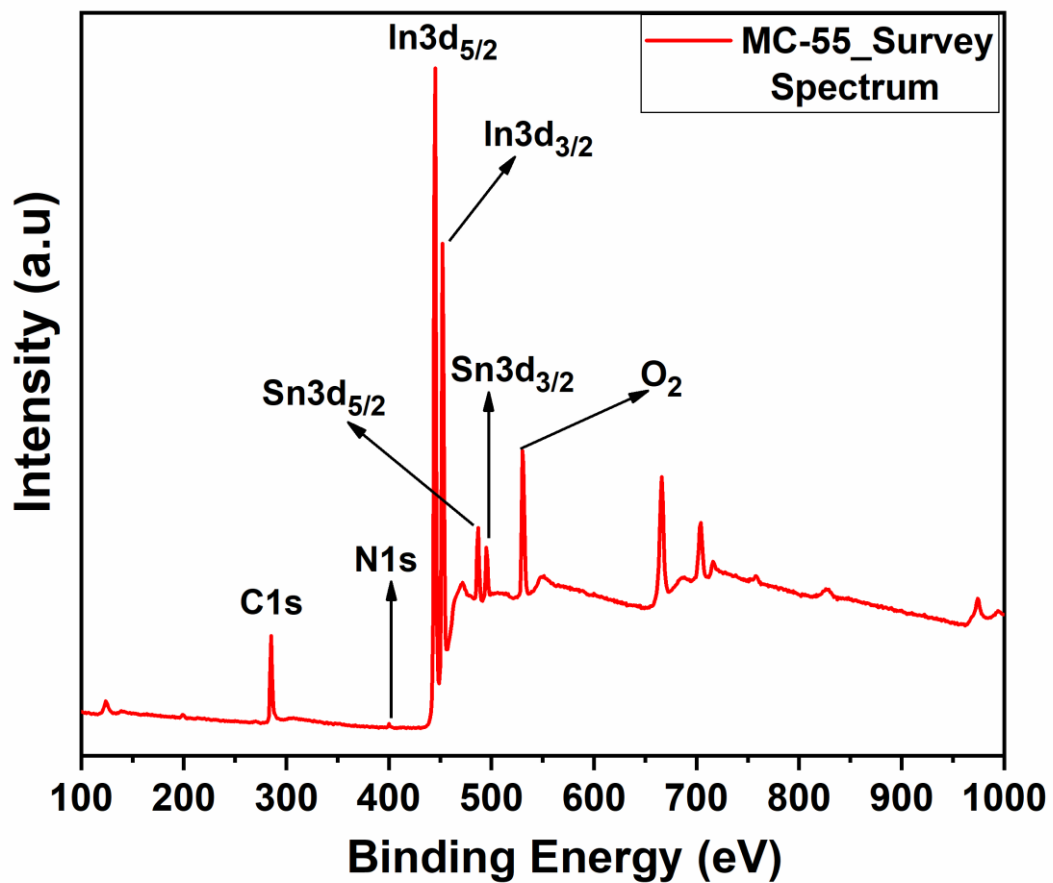


Figure A.6: XPS surface spectrum of ITO/MC-55

Appendice B

Publications from the Thesis

Journal Articles

E. Yalcin, M. Can, C. Rodriguez-Seco, E. Aktas, R. Pudi, W. Cambarau, S. Demic, and E. Palomares; *Semiconductor self-assembled monolayers as selective contacts for efficient p-i-n perovskite solar cells*; Energy & Environmental Science; 2019, 12, 230-237, (DOI: 10.1039/c8ee01831f)

Projects

'Fabrication of Hysteresis-Free Perovskite Solar cells by SAM Modified Electrode'
Supported by 'The Scientific and Technological Research Council of Turkey, 2214-A International Research Fellowship Programme for PhD Students'

Curriculum Vitae

Name Surname : Eyyup Yalçın
E-mail : eyupyalcin21@gmail.com

Education:

2007–2012 Ege University, Dept. of Physics.
2013–2015 İzmir Kâtip Çelebi University, Dept. of Materials Science and Engineering.
2016-2022 İzmir Katip Çelebi University, Dept. of Materials Science and Engineering.

Work Experience:

2014 – 2022 Research Assistant
Dept. of Materials Science and Engineering
Izmir Katip Çelebi University

May. 2017 – Aug. 2017
(3 months) Visiting Researcher
Institute of Chemical Research of Catalonia (ICIQ),
Spain

Feb. 2020 – Apr.2021
(15 months) Visiting Researcher
Institute of Chemical Research of Catalonia (ICIQ),
Spain

Publications:

1. **E. Yalcin**, D. A. Kara, C. Karakaya, M. Z. Yigit, A. K. Havare, M. Can, C. Tozlu, S. Demic, M. Kus and A. Aboulouard; *Functionalized organic semiconductor molecules to enhance charge carrier injection in Electroluminescent Cell*; Optical Materials, 69 (2017) 283-290, (DOI: 10.2016/j.optmat.2017.04.038).

2. A. Bayram, **E. Yalcin**, S. Demic, O. Gunduz and M.E. Solmaz; *Development and application of a low cost smartphone-based turbidimeter using scattered light*; Applied Optics, 57 (2018) 5935-5940 (DOI: 10.1364/AO.57.005935).
3. **E. Yalcin**, M. Can, C. Rodriguez-Seco E. Aktas, R. Pudi, W. Cambarau, S. Demic and E. Palomares; *Semiconductor Self-Assembled Monolayers as Selective Contact for Efficient PiN Perovskite Solar Cells*; Energy&Environmental Science, 2019,12,230. (DOI:10.1039/c8ee01831f).
4. E. Arkan, M.Z. Yigit arkan, M. Unal, **E. Yalcin**, H. Aydın, C. Celebi, M. Can, C. Tozlu and S. Demic; *Performance enhancement of inverted perovskite solar cells through interface engineering by TPD based bidentate self-assembled monolayers*; Optical Materials, 2020, 105, 109910 (DOI: 10.1016/j.optmat.2020.109910).
5. E. Arkan, **E. Yalcin**, M. Unal, M.Z. Yigit Arkan, M. Can, C. Tozlu and S. Demic; *Effect of functional groups of self-assembled monolayer molecules on the performance of inverted perovskite solar cell*; Materials Chemistry and Physics 2020, 254, 123435 (DOI: 10.1016/j.matchemphys.2020.123435).
6. E. Arkan, M. Unal, **E. Yalcin**, M.Z. Yigit Arkan, S. Yurtdas, M. Can, C. Tozlu and S. Demic; *Influence of end groups variation of self-assembled monolayers on performance of planar perovskite solar cells by interface regulation*; Materials Science in Semiconductor Processing; 2021, 105514 (DOI: 10.1016/j.mssp.2020.105514).
7. **E Yalcin**, B. Gultekin, H. Bilgili, M. Can; *Kendiliğinden organize olan tek tabaka molekülleri kullanılarak organize olan ışık yayan diyotların veriminin iyileştirilmesi*; GÜFBED/GUSTIJ; 202, 11 (4), 1235-1241 (DOI: 10.17714/gumusfenbil.853760)

Proceeding in Conference/Symposium Books:

1. **E. Yalcin**, S. Demic, A. Erdoğan, O. Mermer, M. Kus, A. N. Ozcivan M. Can; *“Increase Efficiency of Organic Light-Emitting Diode by Using Different Acceptor Self-Assemble Monolayers”*, 1st International Conference on Green Chemistry and Sustainable Technologies (GCSTI-2015), September 30-October 03, 2015 Cesme, Izmir-Turkey.

2. **E. Yalcin**, S. Demic, A. N. Ozcivan, M. Kus, K. Kara, M. Can; *“Increase Efficiency of Organic-Light Emitting Diode by Using Different Donor Self-Assemble Monolayers”*, 1st International Conference on Green Chemistry and Sustainable Technologies (GCSTI-2015), September 30-October 03, 2015 Cesme, Izmir-Turkey.
3. A. N. Özçivan, **E. Yalçın**, A. Erdoğan and M. Kuş; *“An OLED application with Carbazole and Triphenyl based SAM used for HTL”*, 1st International Conference on Green Chemistry and Sustainable Technologies September 30 – October 3, 2015 Izmir-Turkey.
4. A. N. Özçivan, Ö. Mermer, **E. Yalcin**, K. Kara, M. Kuş, C. Tozlu and M. Can; *Improvement of device performance of organic light emitting diodes via ITO surface modification using different SAM molecules*, 1st International Conference on Organic Electronic Material Technologies (OEMT’2015) /25-28 March 2015. Elazig, Turkey.
5. M. Karaman, N. Mutlu, **E. Yalcin**, M. Karakaya, A. N. Ozcivan, M. Can and Z. Tasci; *“High-Efficiency Dye-Sensitized Solar Cell with Novel Ionic Liquids Co-Adsorbent”* 28th National Chemistry Congress 15-21 August 2016, Mersin-Turkey.
6. **E. Yalcin**, D.A. Kara, C. Karakaya, M. Can, N. Kaya and S. Demic; *“Using Self-Assembled Monolayer to Improve device Performance of Organic Light Emitting Diodes”*, 4st International Conference on Energy and Environment Research 17-20 July 2017, Porto-Portugal.
7. A. Aykac. M. Erol, F. Gunes, **E. Yalcin**, M. Can and Halil I. Ciftci; *“Production of Zinc Oxide Nanostructures on a Flexible Copper Plate and Their Potential Application”*, The 4th International Symposium on Pharmaceutical and Biomedical Sciences, March 17, 2018/Kumamoto-Japan